AN INVESTIGATION INTO THE MODELING OF GROUND DEFORMATIONS INDUCED BY UNDERGROUND MINING

by

Zacharias G. Agioutantis

Dissertation submitted to the Faculty of the

Virginia Polytechnic Institute and State University

in partial fulfillment of the requirements for the degree of

Doctor of Philosophy

in

Mining and Minerals Engineering

APPROVED:

Dr. M. Karmis, Chairman, Head

Dr. J. M. Duncan

Dr. G. J. Faulkner

Dr. C. Haycocks

Dr. J. R. Lucas

September, 1987

Blacksburg, Virginia

AN INVESTIGATION INTO THE MODELING OF GROUND DEFORMATIONS INDUCED BY UNDERGROUND MINING

by

Zacharias G. Agioutantis

Committee Chairman: Dr. Michael Karmis

Mining and Minerals Engineering

(ABSTRACT)

The mechanisms of strata deformation due to underground mining were analyzed in an effort to better understand immediate roof behavior and surface displacements. Strata deformation characteristics above longwall and room-and-pillar mines in the eastern U.S. coalfields were evaluated and a numerical procedure was developed for calculating surface displacements.

The model, based on the well-known finite element method, utilized empirical indices associated with subsidence engineering in order to incorporate the site-specific characteristics into the formulation. Different material behavior models and failure criteria were employed in an attempt to determine the areas highly deformed by underground excavation. Additionally, the method was sensitive to the ratios of the elastic moduli used to describe different rocks and/or rock conditions, and not to the magnitude of the elastic properties. Thus, the use of arbitrary reduction factors to convert laboratory to in situ property values was completely avoided and scaling of the calculated surface displacements was based on, the empirically predicted, regional or local parameters. The use of fixed displacement nodes around an opening to induce failure overcame the roof-floor overlap problem encountered in other formulations.

The successful implementation of the proposed methodology for modeling surface deformations complements and enhances existing prediction techniques, which are primarily based on empirical approaches, by allowing parametric analysis for different excavation geometries, roof convergence curves and overburden properties.

Acknowledgements

I would like to thank my dissertation advisor, Dr. Michael Karmis, for his patience, support and valuable advice during the course of my research.

Thanks are also extended to Dr. J. Michael Duncan for his many helpful suggestions, and to Dr. Gavin Faulkner, Dr. Chris Haycocks and Dr. J. Richard Lucas for their review of this manuscript.

I extend much appreciation to Mrs. Johanna Jones for her help in editing this manuscript. I also wish to extend my thanks to the people who helped and encouraged me during this research effort: Dr. Andrej Jarosz, Mr. Jim Overfelt and Mrs. Martha Orth.

Finally, I wish to sincerely thank my parents for their unfailing support and encouragement during the course of my university studies.

Table of Contents

List of Figures

List of Tables

Chapter 1

Introduction

The mechanisms of strata deformation due to underground mining play an important role in the design of underground mining systems, evaluation of roof behavior during and after mining, and the development of surface control measures. The best documented studies on this topic are associated with longwall mining in a number of coalfields around the world, and are primarily confined to immediate roof behavior. Most of their conclusions, however, are directly related to the mining and geological conditions experienced in specific areas and, therefore, may not be applicable to the conditions encountered in the eastern U.S. coalfields. Various researchers have also attempted to directly measure strata deformation close to the seam level during coal extraction, rather than to examine the entire process of ground deformation from the seam level to the surface, in an effort to better understand roof behavior and determine support requirements.

The study of surface displacements can provide valuable insight into the strata deformation mechanisms of the entire overburden rock mass. Measurement and prediction of surface deformations, using a variety of empirical and numerical models, have become very popular in recent years. Models usually employ empirical parameters to represent

average strata behavior, or rely on iterative techniques to determine potential weak areas based on different mathematical criteria. For example, most empirical surface deformation prediction techniques (i.e. the influence function methods) do not consider the effects of overburden strata deformation and weakening, but incorporate various empirical parameters to represent overburden properties and strata behavior. Numerical models, on the other hand, can closely simulate a mining sequence, but rely heavily on the accurate determination of the in situ elastic properties of the coal measure strata.

The objectives of this study were twofold: To identify and evaluate strata deformation characteristics above longwall and room-and-pillar mines in the eastern U.S. coalfields, and to develop a numerical procedure for calculating surface deformations by relating the surface phenomena to overburden deformation characteristics.

During the preliminary analysis, particular emphasis was placed on the effects of the geological and geomechanical characteristics upon the two most important manifestations of immediate roof deformation: the caving height, which is associated with the expansion ability of the broken material (bulking), and the extent of the caving zone, which describes the highly deformed areas above the excavation. The former determines the weight of the strata that the supports are called upon to accept, whereas the latter defines the area where inelastic behavior of the fractured material is expected. Roof behavior was subsequently evaluated using existing methodology, and the various empirical approaches were compared. The limitations of each method to realistically model the caving mechanisms, and consequently the deformation characteristics of the overburden were identified and examined in depth. Some of these studies appeared to be theoretical and conceptual, ignoring many important parameters of the geological environment, whereas others relied heavily on geological information but lacked a rigorous

foundation upon which a generalized model could be based. Surface phenomena were also evaluated with respect to underground disturbance propagation.

A number of existing numerical models were evaluated for their ability to satisfactorily model overburden deformations while conforming to the boundary conditions and limitations imposed by the physical problem. Existing numerical models described in the literature, were, in most cases, tailored to a specific case study with respect to both the elastic properties used and the failure criteria applied. These, however, lacked the ability to accurately estimate the horizontal strain experienced on the surface. A numerical procedure was therefore developed, based on the well-known finite element method. The model incorporated concepts related to the mechanics of strata deformation characteristics, derived from the empirical analysis, as well as empirical indices associated with subsidence engineering. Different material behavior models and failure criteria were employed in an attempt to determine the areas highly deformed by underground excavation.

Deformation zones based on empirical parameters were defined in the overburden, in an attempt to simulate the theoretical and observed strata deformation characteristics. Accurate subsidence and horizontal strain calculations verified the modeling procedure with respect to the strata deformation zones used in the model. Finally, the model was used to predict vertical and horizontal movements, based on the developed procedure and on regionally predicted values for the required empirical parameters.

The successful implementation of the proposed methodology for modeling surface deformations complements existing prediction methods, namely the profile function method, the zone area method and influence function method. Furthermore, the influence function method and the finite element model are the only methods capable of

calculating horizontal movements, which in turn are necessary in order to calculate horizontal strains. Parametric analysis was also possible for different excavation geometries and different overburden properties.

Chapter 2

Overburden Deformation Mechanisms

2.1 Strata Mechanics

The number of coal mines employing the longwall mining method has increased in the past several years, both in the U.S and worldwide. Experience has demonstrated that longwall mining is safer and much more productive than room-and-pillar mining. With respect to ground control, longwall mining disturbs the overburden strata from the immediate roof to the surface, but due to the uniform extraction sequence employed, strata behavior is predictable and several methods have been used to describe and quantify such disturbances. In general, the difference between the minimum and maximum stress (deviatoric stress) governs elastic movement within the elastic limit. Further stressing induces cleavage, and then bodily movement, of all points within individual blocks. Movement along the first induced cleavage plane relieves the component of stress acting parallel to that plane. The additional stress relieved is displaced partly into adjacent rock, to initiate further cleavage planes and/or movement. Thus, a propagation of fractures and cracks takes place throughout the strata, due to continuous stress redistribution, progressing from the point of initiation at seam level to the surface.

The spacing at which cleavage planes are induced in a particular kind of strata is related to the rate at which the strata is stressed. Closer spacing seems to be characterized by a slower rate of advance while wider spacing is characterized by a higher rate of advance (NCB, 1972).

2.1.1 Roof Zones

The disturbance zones in the overburden strata, occurring in response to longwall mining, are shown in Figure 2.1. The **caved zone**, which constitutes the immediate roof before it caves, ranges in thickness from two to eight times the excavation height. The **fractured zone**, which lies above the caved zone, consists typically of large blocks defined by vertical fractures and horizontal cracks occurring due to bed separation. The thickness of the fractured zone ranges from 28 to 42 times the mining height (Peng, 1986). Between the fractured zone and the surface is the **continuous deformation** or **intermediate** zone, in which the strata usually deform without causing any major cracks, and which can, therefore, be considered to be a continuous medium. The beds sag in a predominantly elastic fashion, and may become detached horizontally along bedding planes. A **surface zone**, consisting of loose overburden layers and/or topsoil, behaves plastically and follows the solid bedrock down into a trough-shaped depression.

Focusing more closely upon the area above the opening, the **immediate** roof corresponds to the caved zone, while the **main** roof includes the lower portion of the fractured zone and extends to the surface (Figure 2.2).

Peng (1984) classified the immediate roof as **unstable, medium stable**, and **stable**, depending upon the strength of the roof and the amount of time that it can be left unsupported before failing (Figure 2.3). The rock type, thickness and the geomechanical

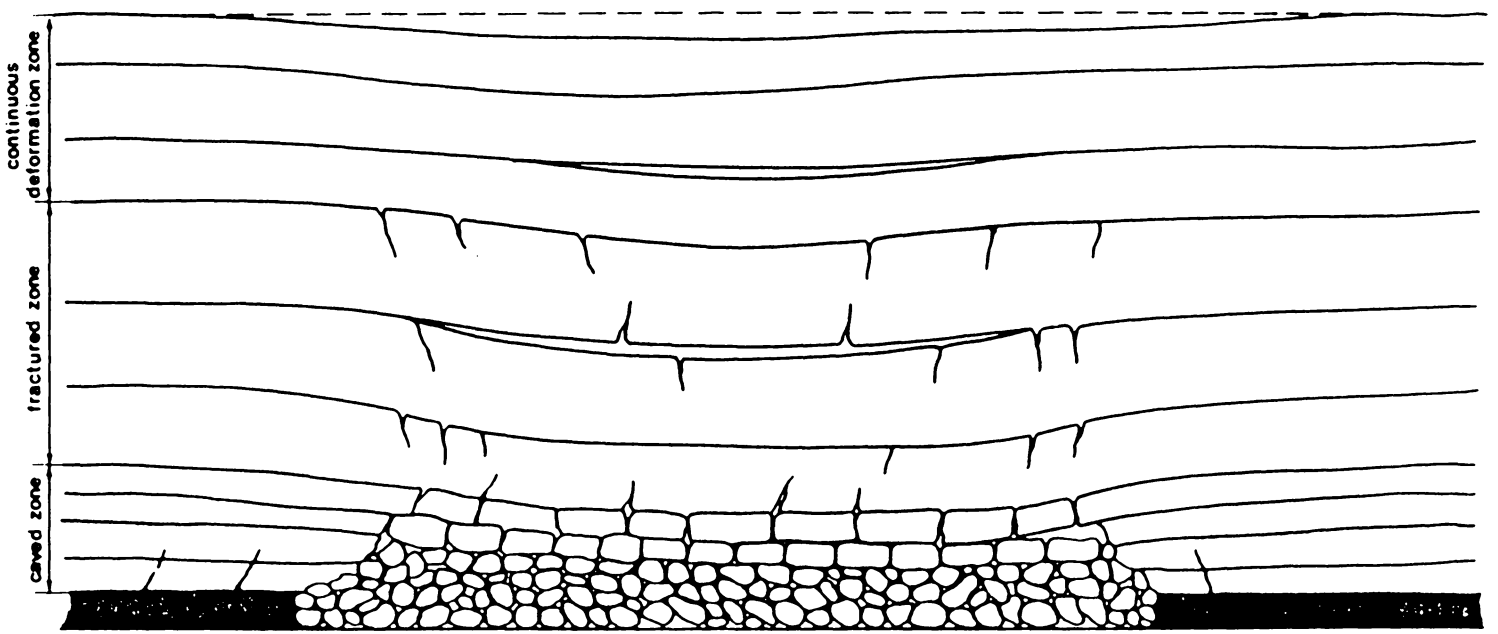

Figure 2.1 Overburden Zones due to Longwall Mining [after Peng and Chiang, 1984]

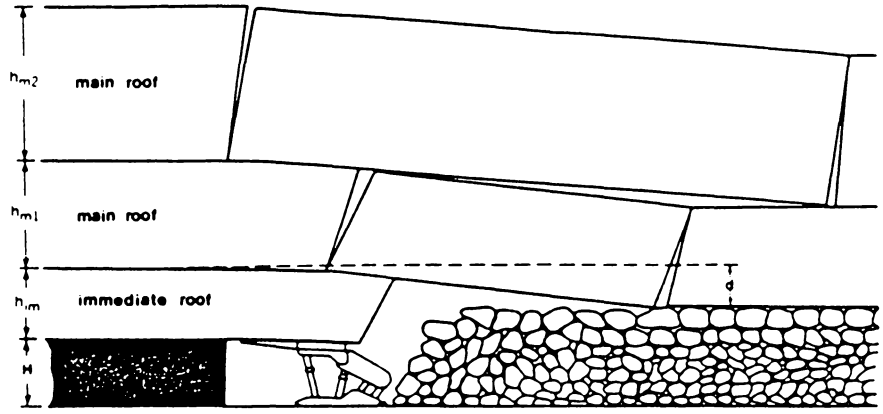

a

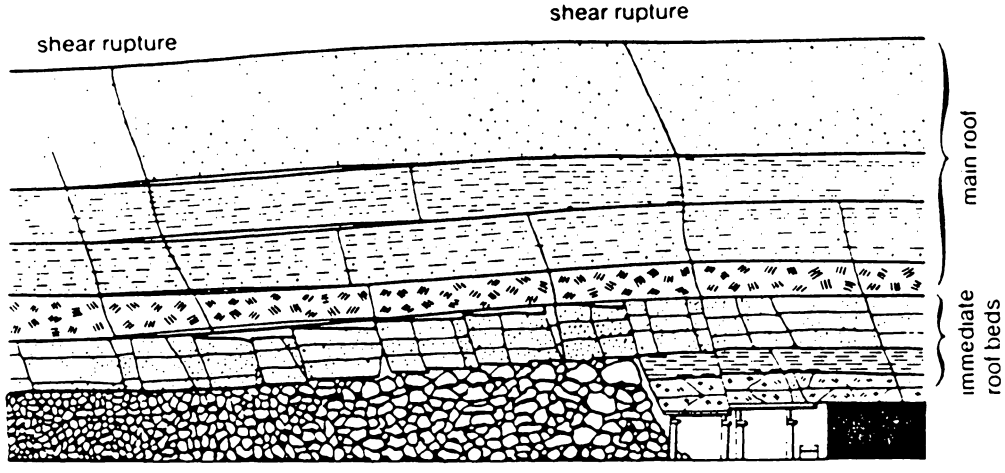

b

Figure 2.2 (a) Immediate and Main Roof [after Peng and Chiang, 1984]; (b) Shearing Effects in the Immediate and Main Roof [after Kratzsch, 1983]

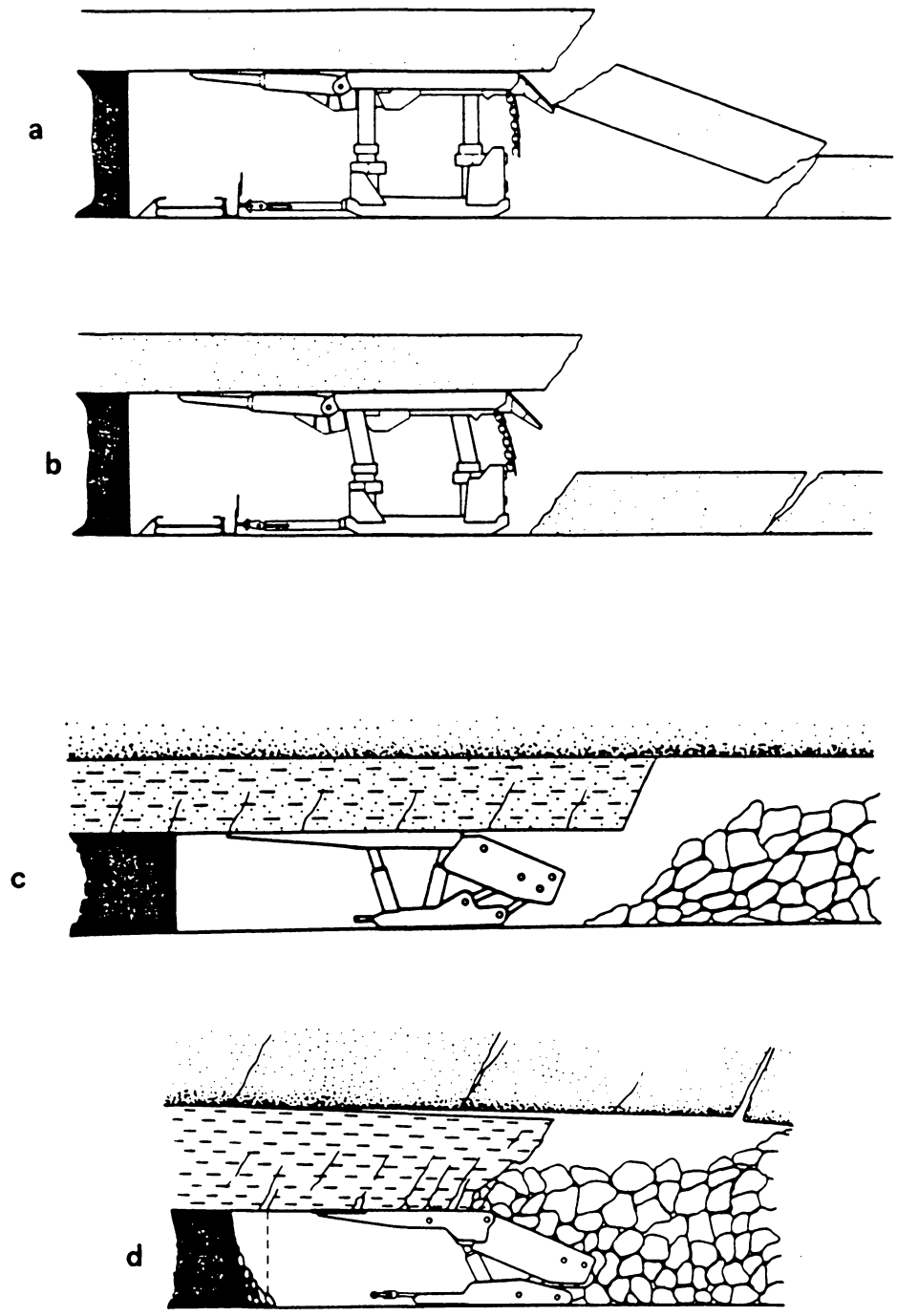

Figure 2.3 Classification of Immediate Roof: (a, b) Stable; (c) Medium Stable; (d) Unstable [after Peng and Chiang, 1984]

properties of the immediate roof are important in order to establish its behavior and overall effect with regard to strata deformation. The caving height or the thickness of the immediate roof required to fill up the gob by volumetric expansion (bulking) can generally be determined by the following equation (Peng, 1986):

$$H - d = h_m(K - 1) \qquad [2.1]$$

where

H = the mining height;

d = the maximum deflection (sagging) of the lowest uncaved strata ($d \leq d_o$);

d_o = the maximum allowed sagging without breaking;

h_m = the thickness of the immediate roof or caving height;

K = the bulking factor ranging from 1.1 to 1.5.

The main roof generally breaks periodically along the direction of the face advance, and imposes periodic roof **weightings** to the face area. Its movements will affect the stability of the immediate roof and are governed by the following factors (Peng, 1986):

- Strata separation will occur along the bedding planes which comprise the next weakest zone after existing fractures.
- Strata separation and downward sagging occur first at the lowest layer in the fracture zone, and then propagate upward.
- Depending on the properties of the main roof, movement may be delayed with respect to the immediate roof or may occur simultaneously with the lower strata.

It is important to note that distinguishing the lower portion of the fracture zone and the upper portion of the immediate roof is difficult, especially if the latter is rather thick.

Periodic **weight pressure** in the face area is usually evidence of main roof fracturing, followed by sagging.

Figure 2.4 shows an idealized sequence of roof failure, as longwall mining progresses, where two distinct phases of overburden movement, i.e. first and periodic weighting (or caving) can be identified. The first weighting interval (L_o) is the distance from the set-up entry to the point where the roof first breaks. The second phase begins right after the first weighting and extends until completion of mining in the panel. During this period, the roof pressure at the face area increases and decreases cyclically due to the cyclical breakage of the immediate and/or main roof. The periodic roof weighting interval, L_p, is the distance between two roof weightings. Roof weighting is caused either by shearing or bending breaks, depending on whether the bending strength at the upper surface of the bed or the shear strength in the compression zone is exceeded first. Figure 2.5 shows the principal types of breaking of the main roof identified, as bending fracture, perpendicular shear, and thrust-fracture along slip planes (Kratzsch, 1983).

It is important to note that, in the vicinity of the **transition point**, i.e. in the area of transition from convex to concave curvature above the ribside, bed separation is likely to occur starting from the lower intermediate zone, especially if weak beds are overlain by hard beds. The location of the transition point changes as mining progresses and, thus, since deformations are assumed elastic, the gaps may reclose behind the face and over the gob area.

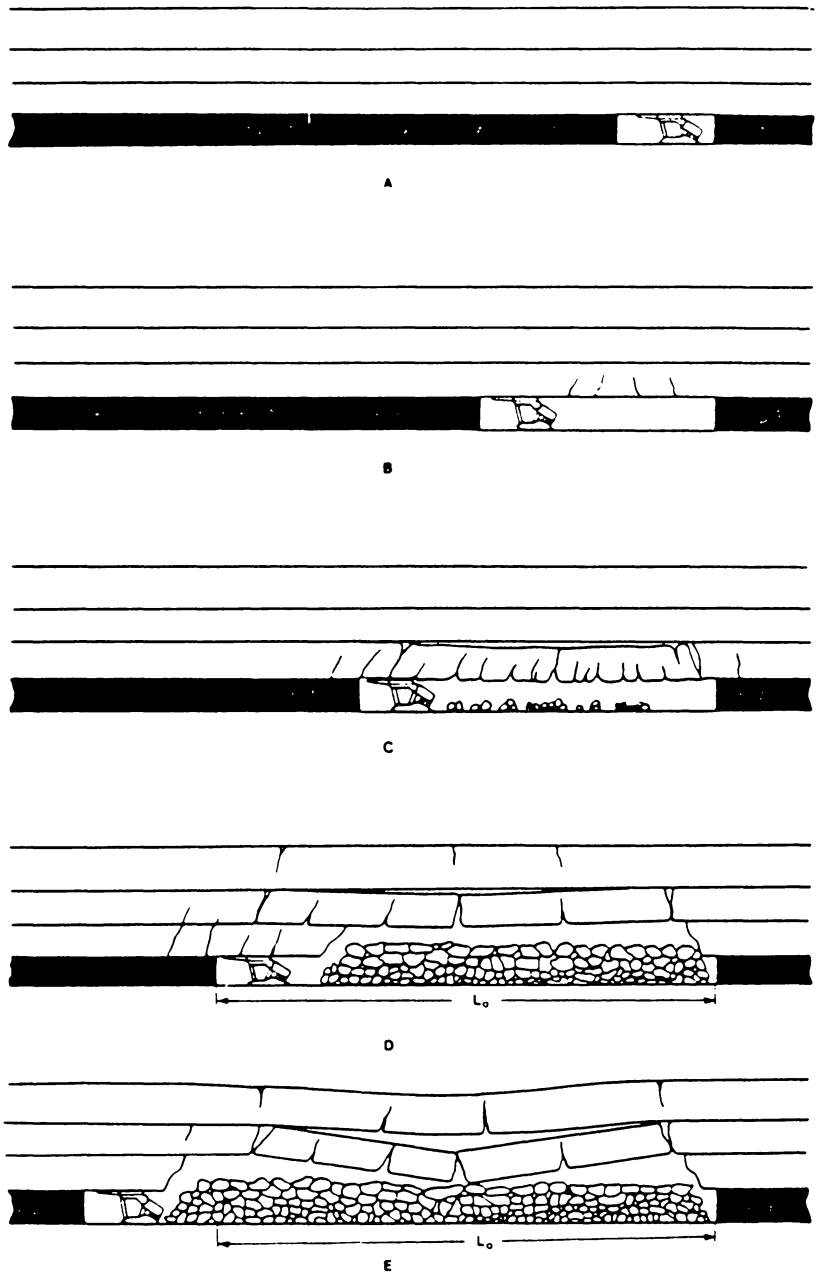

Figure 2.4a Sequences of Roof Movements Leading to First Weighting and Caving [after Peng and Chiang, 1984]

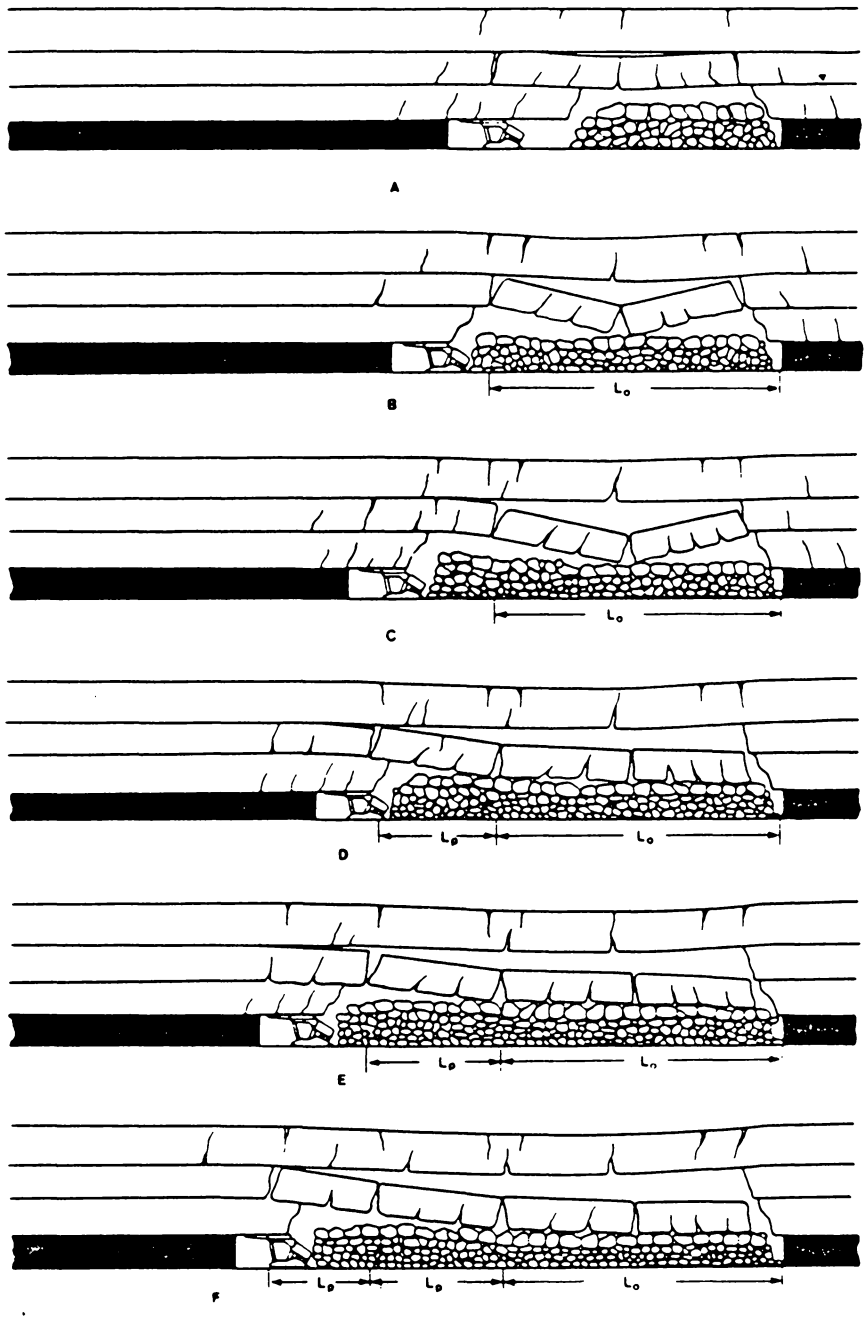

Figure 2.4b Sequences of Roof Movements Leading to First Weighting and Caving (continued)

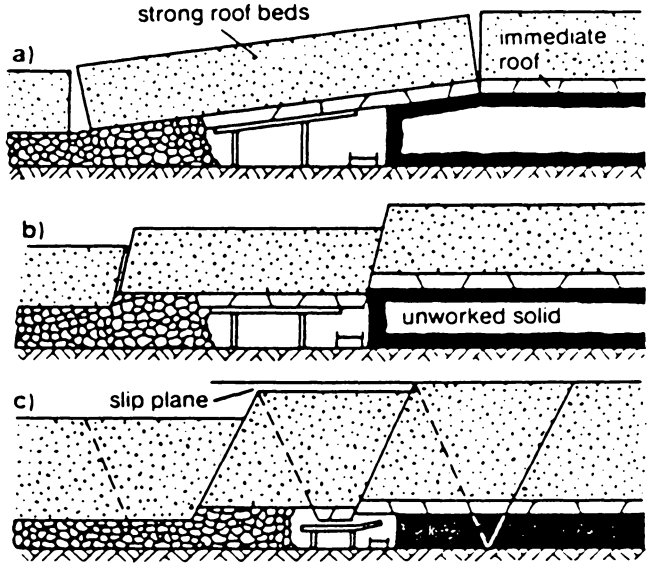

Figure 2.5 Principal Types of Main Roof Break under Caving Conditions: (a) Bending Fracture; (b) Perpendicular Shear; (c) Thrust Fracture along Slip Planes [after Kratzsch, 1983]

2.1.2 Material Bulking

The bulking factor of the failed material is an important dynamic parameter which affects the stress re-distribution after roof failure and gob recompaction. It is defined as the ratio of the volume of the broken rock to the volume of the original intact material. The caved materials immediately behind the longwall face usually have a higher bulking factor, which tends to decrease as the material is compacted by additional material failing over it, or as the applied pressure increases. Table 2.1 presents typical values of initial and residual bulking factors for coal measure strata (Peng, 1984).

2.1.3 Stress Distribution

Parallel to the examination of roof stability criteria, the stress distribution around an opening should be examined in case it can promote the formation of **stable** structures in the immediate roof. The strength of rocks and, more precisely, the relationship between the virgin strength to the rock strength after excavation, is a principal factor governing the stability of mine openings.

Considering vertical displacements, the rock mass undergoes expansion over the gob area and compression over the unworked seam. The different vertical zones are shown in Figure 2.6.

Virgin stress distribution around any panel is disturbed when the panel entries are developed, as well as when the mining face advances. A destressed zone occurs in the roof of the entries and over the panel while the load is transferred to the neighboring solid coal, thus creating zones where the vertical pressure exceeds the average overburden pressure. These zones are called **abutments**, and a typical distribution of front and side

Table 2.1 Typical Values of Initial and Residual Bulking Factors for Coal Measure Strata (Peng, 1984).

Rock Type	Initial Bulking Factor	Residual Bulking Factor
Sand	1.06-1.15	1.10-1.03
Clay	< 1.20	1.03-1.07
Broken Coal	< 1.30	1.05
Clay Shale	1.40	1.10
Sandy Shale	1.60-1.80	1.25-1.35
Sandstone	1.50-1.80	1.30-1.35

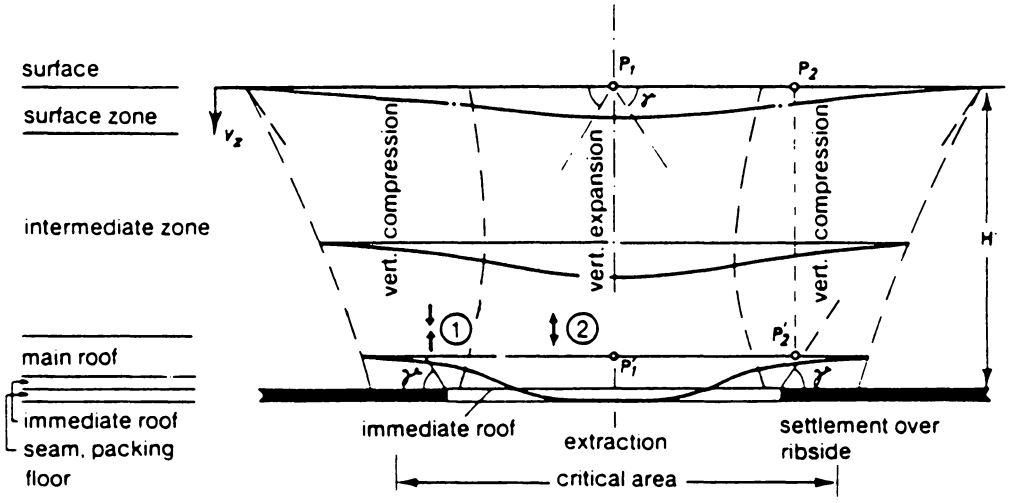

Figure 2.6 Vertical Deformation of an Undermined Rock Mass: (1) Additional Pressure Resulting from Abutment and Bending Pressure (2) Load Reduction and Bed Separation over the Extraction Area [after Kratzsch, 1983]

abutment pressures around an extracted longwall panel is shown in Figure 2.7. Figure 2.8 shows the pressures exerted on the gob and the face along different cross-sections of the mine plan depicted in Figure 2.7. The zone of decreasing vertical and horizontal stress concentration in the roof and floor extends from the abutment area in the shape of an ellipsoid.

The magnitude and location of these abutments depend upon both the physical properties of the roof rock and the geologic conditions in the area. At this stage, the magnitude of the compressive stress developed in the rock strata can exceed the strength of the rock and create zones of clastic, plastic and elastic material. This observation is utilized in the design of panels so that coal may be loosened up by the preceding stress abutment, which at the same time alters the physical characteristics of the surrounding rock. It should be noted that periodic weighting of the main roof can temporarily alleviate and/or re-distribute abutment pressures.

The front abutment reaches its maximum 3 to 20 feet ahead of the face line, but its width varies depending upon its position relative to the face, being wider at both ends of the face and decreasing towards the center. It is reported (NCB, 1972) that, at the point of maximum front abutment pressure, the roof starts to slope towards the waste.

2.1.4 Surface effects

The surface or weathering zone over coal measure strata behaves in a predominantly inelastic and plastic manner in the formation of subsidence troughs (Kratzsch, 1983). All points in the subsidence basin are subject to a three-dimensional motion, which can be described in full by the following deformation indices:

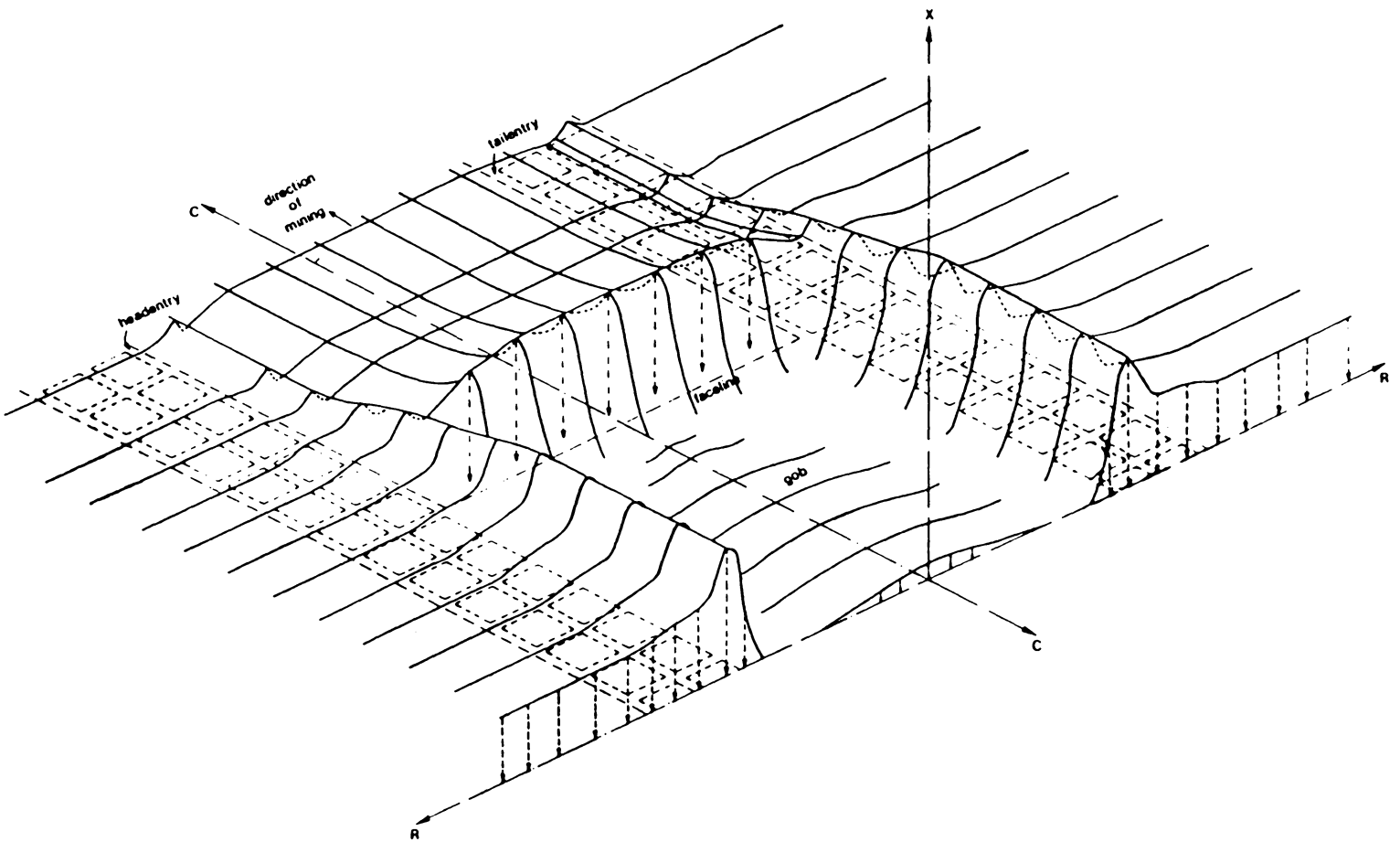

Figure 2.7 **Abutment Pressures around Longwall Extractions in Three Dimensions [after Peng and Chiang, 1984]**

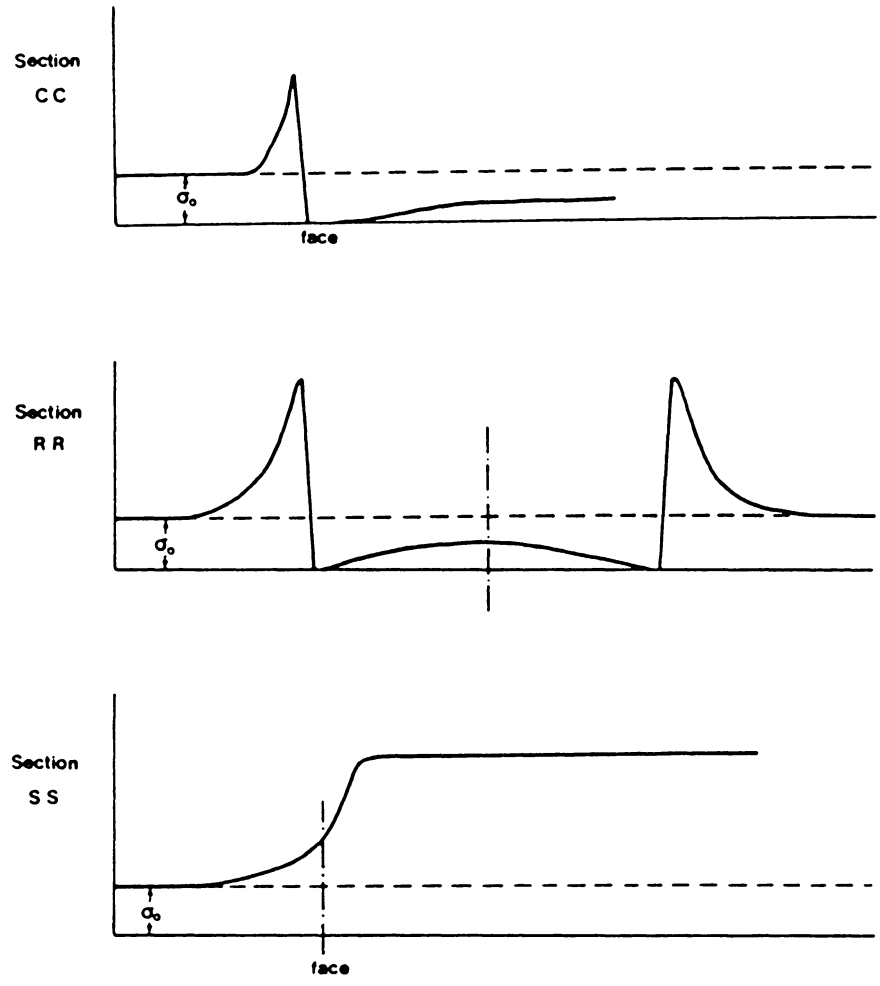

Figure 2.8 Abutment Pressures around Longwall Extractions in Various Cross-Sections [after Peng and Chiang, 1984]

- **Subsidence** (s), which is the vertical component of the surface movement vector.
- **Displacement** (u), which is the horizontal component of the surface movement vector on any vertical cross-section.
- **Horizontal strain** (ε), which is the normalized difference of horizontal displacements between any two points. Compression results in negative strains, while extension is described by positive strains.
- **Slope** ($i = \frac{du}{dx}$), which is the first derivative of horizontal displacements.
- **Curvature** ($k = \frac{d^2u}{dx^2}$), which is the second derivative of horizontal displacements.

Additionally, the following terms are used to define the characteristics of subsidence profiles, as shown in Figure 2.9.

- **Angle of draw** (γ) is the angle between the vertical and the line connecting the panel edge and the edge of the movement basin at the surface. This angle is sometimes referred to as the **limit angle**, and it serves to define the limit of the surface influence, but not necessarily the limit within the rock mass (Kratzsch, 1983). It is evident from the subsidence trough development that, with increasing height above the mining horizon, the bending of the rock strata shifts outwards of the excavated area. Thus, the subsidence trough of each bed from the main roof to the surface is wider and flatter than the one below.
- **Angle of break** (δ) is the angle between the vertical and the line connecting the panel edge and the point of maximum tensile strength at the surface. It should be noted that the point of maximum tensile strain on the ground surface is the most likely point for the occurrence of tensile cracks.

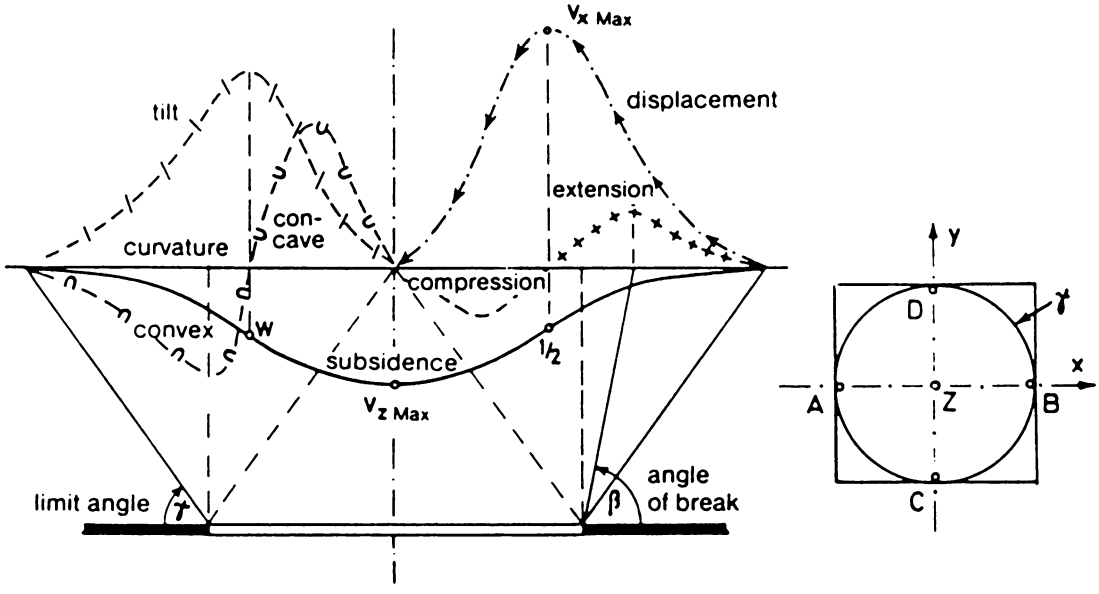

Figure 2.9 **The Vertical and Horizontal Components of Ground Movement over a Critical Area of Extraction [after Kratzsch, 1983]**

- **Inflection point (IP)** is the point that divides the concave and convex portions of the subsidence profile. Also, at this point, the surface slope is maximum and the curvature is zero, and subsidence is equal to half of the maximum subsidence.
- Two theoretical parameters, used primarily with subsidence evaluation techniques which involve influence functions, are also defined. Influence functions mathematically account for surface deformations given the geometry of the excavation, the overburden properties and an appropriate influence function. The **angle of influence** (β) describes the extent of the influence of underground openings on the surface according to a given influence function, and is expressed in a similar manner to that of the angle of draw. The **radius of influence** (r) is defined as $\frac{h}{\tan \beta}$, where (h) is the depth of the excavation.

2.2 Caving Phenomena

Several theories have been proposed to explain the phenomena of roof caving in underground mining, and these can be summarized as follows:

- crumbling of the roof under an arch;
- bending of the roof layers, as though they were beams, followed by crumbling;
- plastic or pseudo-plastic flow of material into the waste area, due to inward movement of the surrounding mass; and
- propagation of ground movement through the rock strata above an underground excavation, resulting in the development of a subsidence trough at the surface.

The observation that cavities and tunnels in soil or rock often remain stable without artificial support, provided that they have assumed the shapes of domes or arches, lead to the early dome or arch theories.

In a very notable study, Denkhaus (1964) examined the elastic dome theory in isotropic and homogeneous media. He distinguished between two separate dome formations, one occurring in sufficiently cohesive rock and the other in less cohesive rock, and calculated the axis ratio of the resulting elliptic arch for both cases. Furthermore, he suggested that the stress re-distribution due to mining must be determined, and the failure hypothesis re-applied until fracture propagation is arrested. When static equilibrium is reached, forces exerted from the rock mass inside the boundary of the dome may result in a stable **voussoir** dome.

Bridging occurs when caving is inhibited as mining progresses, due to the presence of strong massive rock layer(s) that have not failed. When, however, the maximum unsupported width is reached for the particular strata configuration, the supporting layer may break suddenly, resulting in dynamic loading of the supports, damage to mine entries, and even airblast phenomena (Sheorey, 1984).

The evaluation of roof caving parameters has been generally approached by applying the methods described in the following sections.

2.2.1 Pressure Arch Theories

The pressure arch theory has been investigated in depth by British investigators since the early 1900's. It was found that the distribution of the forces in the vicinity of a narrow opening can be represented as shown in Figure 2.10 (Adler and Sun, 1976). In the case

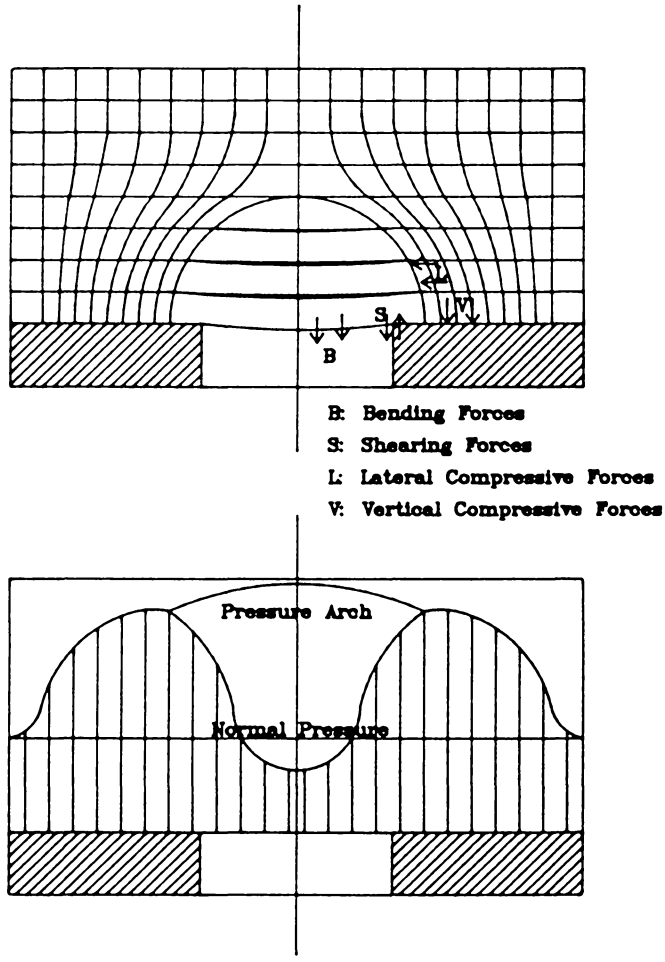

Figure 2.10 Stress Re-Distribution around an Opening and Associated Forces [after Adler and Sun, 1976]

of longwall mining, upon excavation of the opening the weight is transferred to the solid sides, and a transverse pressure arch is developed above the excavation, within which lies a zone of destressed strata. The maximum width of the pressure arch can be calculated from the following empirical formula:

$$W = 0.15\ D + 60 \qquad [2.2]$$

where

W = the width of the maximum pressure arch [feet];

D = the excavation depth [feet].

Extensive field observations have verified (Adler and Sun, 1976) that the maximum possible width between the pressure arch abutments generally increases with depth, although it is also influenced to some extent by the prevailing strata conditions. Figure 2.11 shows pressure arches associated with good and poor mining conditions. If the excavation width exceeds the maximum width of the pressure arch, intense fracturing can occur and a great amount of weight will be transmitted directly to the pillars. The height of the pressure arch is a function of the material properties, rate of extraction, span of the working area, vertical to horizontal stress ratio, etc. For small horizontal stresses and low rock strength, the pressure arch tends to be higher.

2.2.2 Dome Theories

Dome formations, and the principles governing their state of equilibrium, have been examined extensively (Denkhaus, 1964; Dinsdale, 1955; etc). Figure 2.12 shows the pressure rings developed around a supported opening. A simple static analysis of the

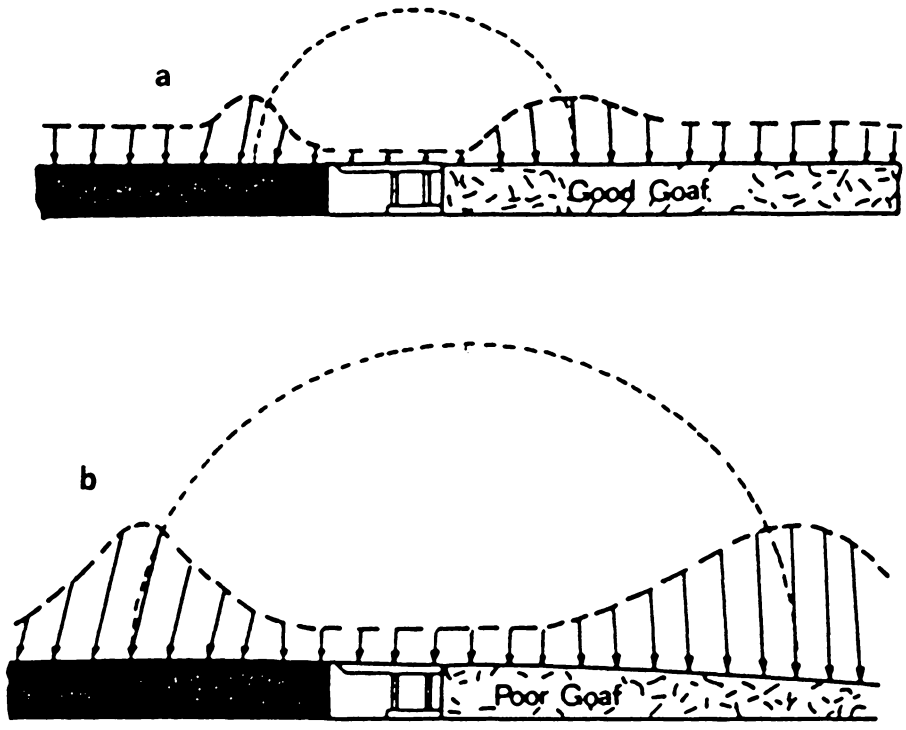

Figure 2.11 Effect of the Width of the Pressure Arch to Face Conditions: (a) Narrow Pressure Arch, Good Face Conditions; (b) Wide Pressure Arch, Poor Face Conditions

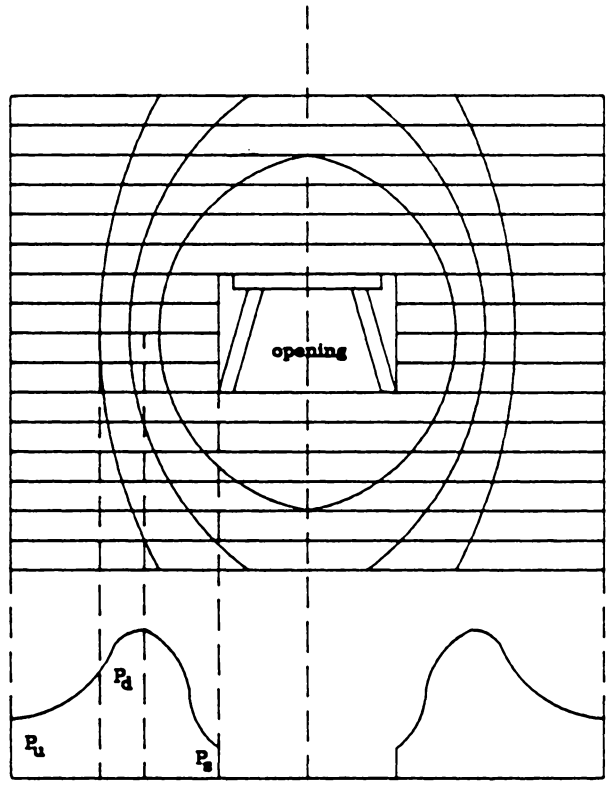

P_u = pressure in undisturbed rock
P_s = pressure on support within opening
P_d = pressure to sides of drift

Figure 2.12 Pressure Dome and Stress Trajectories around a Drift [after Adler and Sun, 1976]

forces acting on the dome indicates that the height of the dome is directly related to the vertical pressure, according to the following relationship:

$$h = \frac{P}{8H}(2Lb + b^2) \qquad [2.3]$$

where

P = the pressure per unit length exerted on the dome by the overlying rock [lbs/ft];

H = the horizontal force [lbs];

h = the height of the dome [feet];

b = the span of the opening [feet];

L = the width of the abutments [feet];

under the assumptions that the value of L is given; the location of the vertical force (R) is at the center of the abutment; and the values of P and H are known.

A method for calculating the stress distribution for a rigid or elastic dome, based on the equilibrium forces on the dome boundary (Figure 2.13), has been developed by Denkhaus (1964). For **insufficiently cohesive** rock, a portion of the core of the dome will gradually separate from the dome boundary while the span of the dome is being increased. The relationship between the span and height of the dome is given by:

$$L = \sqrt{\frac{8\sigma_c d}{w}(1 - \frac{h}{d})\log(1 - \frac{h}{d})} \qquad [2.4]$$

where

L = the span of the dome;

h = the height of the dome;

d = the excavation depth;

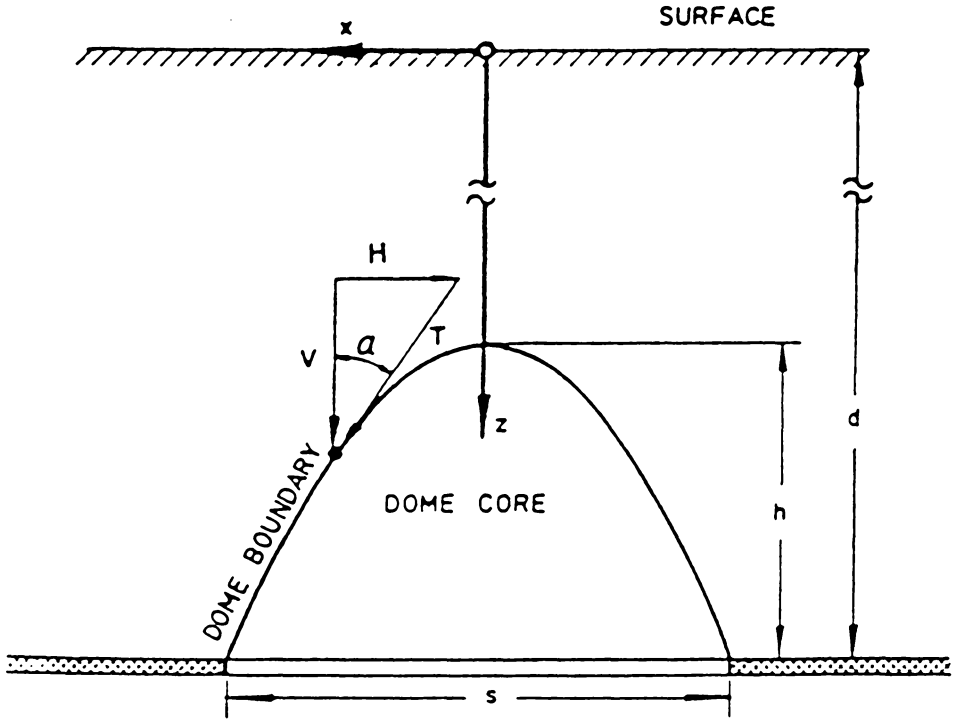

Figure 2.13 **Forces at Dome Boundaries [after Denkhaus, 1964]**

w = the specific weight of the rock;

σ_c = the uniaxial compressive strength of the rock.

If the rock is **sufficiently cohesive**, the core of the dome will not separate from the dome boundary, which must then carry the weight of the dome. The relationship between the span and the height of the dome is given by:

$$L = \sqrt{\frac{8\sigma_c d}{w}(1 - \frac{h}{d})} \qquad [2.5]$$

It should be noted that when the above formulation, which was initially developed and applied to deep mines, is applied for shallow mining depths, the calculated dome height is larger than the mine depth. This implies that the rock included within the dome boundary is weakened, and the disturbance initiated by the underground opening will be transmitted to the surface, thus creating surface subsidence effects. For greater depths, however, the underground disturbance would be **absorbed** by the overburden without any surface effects. This suggests that the dome theory would be useful in delineating the affected areas, but would not give specific information about strata behavior within those areas.

A modified dome concept in elastic rock has been proposed (Adler and Sun, 1976) by assuming that the rock inside the dome is fractured and the dome has an elliptical shape with a height of twice its span (Figure 2.14). The height of the dome can then be obtained by the following formula:

$$h = \left[\frac{1 + \frac{\sigma_t}{w} d}{2K} - 0.5\right]\frac{L}{2} \quad \text{or} \quad h = \frac{L}{K - 1 + \frac{\sigma_c}{w} d} \qquad [2.6]$$

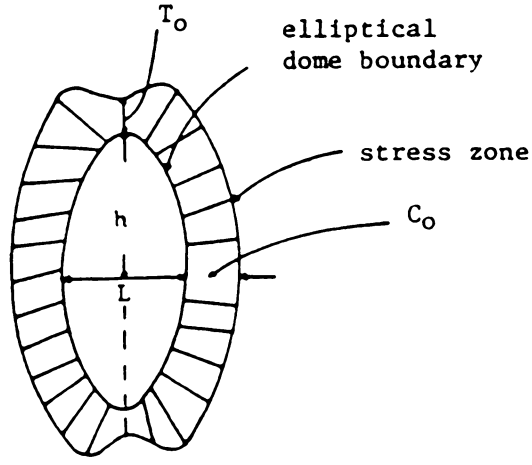

Figure 2.14 Stress Distribution around an Elliptical Dome [after Adler and Sun, 1976]

where

K = the ratio of the lateral to vertical rock pressure;

σ_t = the tensile strength;

σ_c = the compressive strength.

2.2.3 The Voussoir Arch Theory

The concept of the voussoir arch was introduced in mining in 1941 (Adler and Sun, 1976) to account for the ability exhibited by highly fragmented roof strata to stand unsupported, although the rock did not have the tensile strength required by any other traditional approach (e.g. the beam theory).

The stability of such a voussoir arch (Figure 2.15) requires that the following conditions are fulfilled (Adler and Sun, 1976):

- **Rotation**: To avoid possible tension or rotation, the eccentricity of thrust must be limited to one sixth of the breadth of the joint, that is, the thrust must fall within the middle third of the joint.
- **Sliding**: The joint is safe if the angle made by the resultant of the normal and transverse forces with the normal to the joint is less than the angle of friction.
- **Crushing**: Stresses experienced by the joints should exceed the maximum compressive strength of the material.

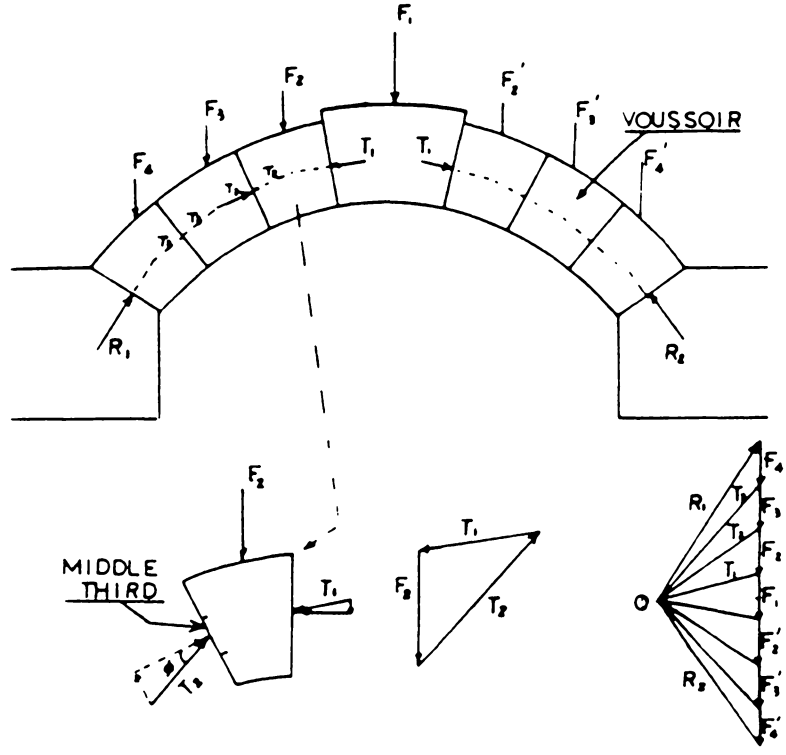

Figure 2.15 **Forces Acting on a Voussoir Arch [after Adler and Sun, 1976]**

2.3 Analytical Roof Stability Evaluation

2.3.1 Beam and Plate Theories

The overburden can be modeled as a series of stratified beam layers, with the immediate roof being the first beam above the underground excavation. Before failure, the beams are treated as fixed, while, after a beam has failed, small cantilevers are created on either side. Thus, the span of the next layer can be calculated, and is less than the original opening width. The deflection of each beam depends upon its thickness and its elastic deformation modulus. Hence, it is possible that a lower beam deflects more than the overlying one, so that a gap --termed the Weber cavity (Denkhaus, 1964)-- develops between the two beams. The extent of interlayer loading can be calculated, given the properties of the beams (VPI&SU, 1981), and the caving height can then be approximated by allowing roof layers to fail in a step-wise fashion, and the bulked material to fill the void.

To calculate the weight imposed on the supports at a given longwall face, the beam theory assumes that the immediate roof detaches from the overlying main roof, and forms a cantilever beam over the face supports. The deflection and subsequent failure of this beam depends on the specific weight, elastic properties and thickness of the rock material, the unsupported span allowed, and the type of supports. The model of a simple cantilever beam resting on a flexible support simulates real conditions better than the assumption of a rigid support (Peng, 1978). Shepherd (1973)[1] described the different calculated modes of fracture of the immediate roof beam under varying conditions, such

---

[1] Peng (1978)

as at different depths of excavation and under high shear or high normal stresses (Figure 2.16).

In a recent study (Majumder, 1986), the bending moment distribution on a cantilever beam behind a longwall face was applied in order to estimate support requirements at the face. Again, the concepts of stratified layers and interlayer loading were employed in order to calculate beam-loading conditions.

When the length of the roof is less than twice its width, calculations of stresses and deflection should be performed using the equations developed by the plate theory.

2.4 Empirical Roof Quality Evaluation

It is widely acknowledged today that engineering classification of rock masses is necessary in order to characterize rock for engineering purposes.

When this approach is applied to mine roof caving studies, the caving ability of the roof is assessed by an appropriate geomechanical rock classification method. As in all attempts to classify rocks for engineering design, the conclusions and statistical inferences refer to particular local conditions, which may vary considerably from site to site. Combining results from different mining environments, utilizing the appropriate scaling factors, may consequently lead to a more general roof characterization scheme. In this study, however, only the classification techniques suitable for measuring and/or predicting roof caving in longwall or secondary extracted room-and-pillar panels are evaluated.

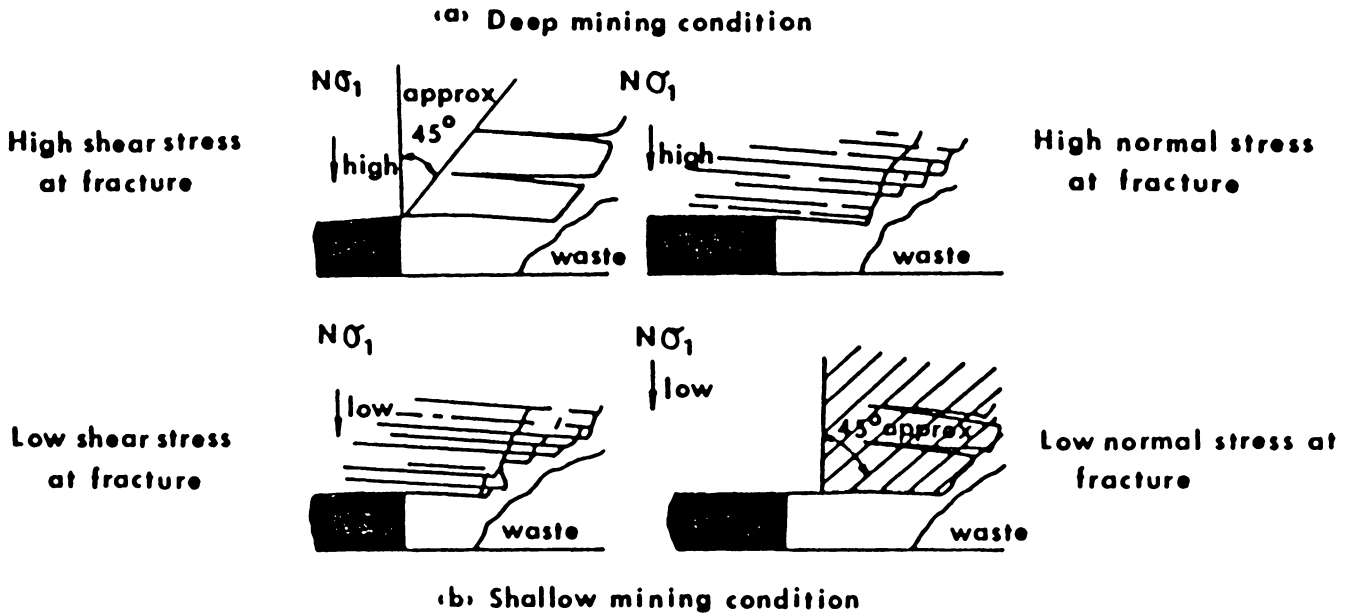

Figure 2.16 Modes of Fracture of Roof Beams under Various Extreme Conditions [after Peng, 1978]

Qualitative criteria for classification of roof types with different caveability have been developed by researchers based on the geologic structure. Proyavkin *et al.*[2] developed an index of roof subsidence due to caving (h) as a function of seam thickness (m) and the width of the opening (s), as:

$$h = k\ m\ s \qquad [2.7]$$

where

k ranges from 0.015 to 0.04, depending on roof stability characteristics; and all units are in [m].

Kidybinski (1982) also references classification schemes developed for eastern European coalfields. One is based on the point load index strength and the corresponding layer thickness, while another calculates a roof index based on the average frequency of natural bedding plane occurrence in the roof rocks. The index may be improved when scaled for time, humidity and rock quality factors.

A classification technique based on bed separation resistance (or resistance of roof rocks in tension in the vertical direction) has also been quoted in the literature (Kidybinski, 1982). The immediate roof is subdivided into:

- the falling roof extending from 0 to 0.5m over the immediate roof;
- the fractured roof, extending from 0.5 to 1.5m over the immediate roof; and
- the compact roof extending from 1.5 to 3.0m over the immediate roof of the longwall face.

---

[2] Kidybinski (1982)

In practice, hydraulic borehole penetrometers can be used to measure the immediate roof characteristics to a depth of up to 3 times the seam thickness.

Another classification scheme, developed in Poland (Unrug and Szwilski, 1982), can be represented by an empirical rock quality index (RQI), L, given by:

$$L = 0.016\ C_s d \qquad [2.8]$$

where

C_s = the compressive strength of the roof rock in situ [kg/cm^2], given as:

$C_s = C\ K_1\ K_2\ K_3$;

C = the compressive strength measured in the laboratory [kg/cm^2];

K_1 = the coefficient of strength utilization, $0 < K_1 < 1$;

K_2 = the coefficient of strength loss with time, $0 < K_2 < 1$;

K_3 = the influence of moisture in mine air, $0 < K_3 < 1$;

d = the thickness of the immediate roof [cm].

A classification scheme is then based on the value of L, as shown in Table 2.2. The face advance required to induce the first caving of the gob, R, [m] can be expressed in terms of L as follows:

$$R = 4.47\ L^{0.4} \qquad [2.9]$$

A classification system developed in Russia (Peng, 1984) is based on rock strength and exposure time, in contrast with the Polish system, which is based on bed thickness. The system classifies the roof in a similar manner, from unstable to very stable.

Table 2.2 Roof Classification (Unrug and Szwilski, 1982)

Classification Group	Roof Quality Index, L	Allowable Area of Exposed Roof [m^2]	Description of Roof Strata
I	$0 < L \leq 18$	approx. 1	Very weak. Immediate fall of roof when exposed. Coal tops recommended for safety. Stratified with coal bands, claystone, wet.
II	$18 < L \leq 35$	1 to 2	Incompetent, friable. Difficult to control. Banded claystone, fissured.
III	$35 < L \leq 60$	2 to 5	Firm, competent, caves readily. Claystone, mudstone fractured, wet.
IV	$60 < L \leq 130$	5 to 8	Good caving characteristics. Strong claystone, mudstone, coarse sandstone, weak, wet.
Va	$130 < L \leq 250$	above 8	Strong, durable. Requires system to initiate caving. Strong mudstone, sandstone.
Vb	$L > 250$	--	Very strong. Not suitable for caving. Thick sandstone, limestone.

The first weighting interval can also be estimated using a simple tension formula (Peng, 1984):

$$L = \sqrt{\frac{2hT}{g}} \qquad [2.10]$$

where

h = the height of caving of immediate roof;

T = the tensile strength of immediate roof;

g = the density of immediate roof.

In another study, Sheorey (1984) defined the caving span as the extent of the face advance of a longwall face from the start line until the immediate roof collapses. The exposed roof is modeled as a rectangular plate simply supported and uniformly loaded, failing in tension. The equivalent face advance is then defined as:

$$a_{eq} = \sqrt{\left(\frac{\beta}{\beta'}\right)}\ a \qquad [2.11]$$

where

β = factor depending on the rectangularity (c/a) of the caving area;

β' = the limiting value for b when c/a > 3;

c, a = the width and length of the panel, respectively.

Regression results from 12 case studies show that a_{eq} is correlated with the average RQD of the immediate roof, measured by scan line techniques on the face and entries, through the following linear relationship:

$$a_{eq} = 0.59\ RQD + 5.2 \qquad [2.12]$$

where a_{eq} is expressed in meters [m].

Again, the application of the equation is limited to cases that simulate the mining conditions of the source case studies. In the same study, the equivalent span a_{eq} was also calculated as a function of the Q-index, which was proposed by Barton *et al.* (1974) for rock classification purposes. The latter index considers several other joint parameters besides RQD, e.g. joint set, joint roughness and joint alteration numbers.

The application of the Rock Mass Rating system, RMR, for caving evaluation can also be considered. Bieniawski (1976) proposed the use of RMR to estimate maximum unsupported span or stand-up time of an underground excavation. This concept has been extended to coal mining for supporting mine entries (Bieniawski, 1984).

2.5 Numerical Modelling Approach

Experience has shown that empirical and phenomenological methods may be used in order to provide a good estimate of ground movements, given an extensive data base of regionally grouped observations. They do not provide, however, the means for an accurate parametric analysis covering a range of geomechanical conditions.

Mathematical models that cover a variety of failure mechanisms present an alternative method for analyzing geomechanical problems. The application of these models involves discretization of the domain into individual cells or elements, and application of a set of constitutive equations and/or a failure mechanism to the individual elements. Two- or three-dimensional ground deformation models have been used extensively for estimating maximum subsidence above longwall and room-and-pillar workings, and for determining subsidence profile shapes. In most cases, however, model parameters (such

as elastic moduli, reduction factors, etc.), are calculated after fitting a regional model to measured data. Few numerical procedures mention application of caving and reconsolidation routines in their numerical codes. Specifically, routines incorporated in a finite element program developed by ACIRL (Holt and Mikula, 1984) were reported to be able to detect failed material, plus material isolated by failed material or joints. Bulking expansion due to fragmentation was initiated, and the material was subsequently reconsolidated to accept load from surrounding materials. A displacement discontinuity program developed by the same research group required an estimated caving height as input data. A program developed at Penn State (Mozumbar, 1974) allowed for node separation and recontact along strata layers. The objective of the program was subsidence modeling over longwall panels. Also, a program developed by the Sandia National Laboratories (Sutherland, 1986) is reported to incorporate a "RUBBLE" model to allow for material failure and reconsolidation.

In the following sections, some of the different techniques and models available for modeling geotechnical problems and ground movements, as applied to undermined areas, are critically reviewed.

2.5.1 Displacement-Discontinuity Techniques

In this approach, the models perform a simplified mathematical analysis of a **plan** view of a mining layout, as contrasted with analyses of cross-sections performed by the other types of models. Although this formulation is efficient in modeling the stability of mine layouts, it is not suitable for subsidence prediction. It has often, however, been incorporated into two-stage models that combine two different techniques, as will be explained in later sections.

Reported application:

- A displacement discontinuity code (THREED), which was developed by the Australian Coal Industry Research Laboratories, conducts a simplified mathematical analysis of a plan view of a mine lay-out, and is able to model the effects of confinement of coal on yielding (Holt and Mikula, 1984). A simplified caving criterion was then introduced into the above program with the following assumptions: Caving takes place at the nominated (assumed) caving height within the caving zone, but the gob material does not transmit any stresses from roof to floor until the calculated closure reaches a certain magnitude.

2.5.2 Rigid Block Models

Rigid block models were first introduced by Cundall (1974), and have since been developed and further applied to a variety of problems. Rock mass is modeled as an assembly of rigid blocks, which can move independently according to the driving mechanism (e.g. gravity, external forces etc.). Blocks can crack, and the resulting pieces can also assume independent motion. All deformations occur at the block contact points on the respective surfaces, resulting in forces being generated at these points. A change in displacement (i.e. downward movement) produces a change in force, which is then added to the existing force associated with the contact. The new force field governs the block behavior (displacement, rotation, cracking and separation, etc.), and the procedure is repeated until equilibrium is reached. This can prove very costly for modeling overburden strata behavior all the way to the surface (depending on the time increment factor), but can be advantageously applied to the **near field**, where fracturing actually occurs. This can

in turn be coupled with a **far field** method to model elastic or plastic deformations, as demonstrated below.

Reported applications:

- Lorig (1984) postulated the application of a hybrid distinct element / boundary element method. He suggested that the distinct element method is well suited to the analysis of jointed media surrounding excavations. This is particularly applicable in cases where separation and slip on discontinuity surfaces result in displacements which may be orders of magnitude greater than elastic displacements. In such cases, the performance of the rock mass is dominated by its discontinuous nature and, therefore, its elastic properties may be ignored. The deficiency associated with this method, when applied to analysis of underground excavations in blocky media, is that it creates the necessity of discretizing the complete problem domain. However, field measurements of displacements, as well as elastic analyses of stresses and displacement distributions around underground excavations, indicate that far field rock responds to excavation as an elastic continuum.

- Sutherland (1986) reported the use of a model called "BLOCKS" to analyze roof stability and subsidence. The method uses a simple parallel spring and dashpot model to calculate the resulting normal forces during block interaction. When the blocks are allowed to deform, the action is analogous to constant strain elements in the finite element method applications. A routine to account for roof failure and recompaction has also been incorporated into this model.

2.5.3 Combined Models

Formulations that combine more than one technique are potentially better for realistic modeling of strata behavior than any single technique, provided that the physical and mathematical continuity of the medium is established between the two methods. This is especially true when more than one physical phenomenon need to be taken into account simultaneously (e.g. ground movement and ground water flow, near and far field response, etc.).

Reported applications:

- Trent (1979) developed a two-dimensional code which couples near and far field response. The modeling tools used were derived from existing computer codes, namely a Linear Elastic Small Strain code simulating the far field and a Rigid Block Model for the near field effects. Preliminary results showed that the coupled code responded well for small time steps, where piling of the broken material over an underground opening was not initiated.

- Lorig (1984) also developed a combined code, as mentioned under the rigid block model techniques.

- Kripakov *et al.* (1986) applied the finite element method in conjunction with a displacement-discontinuity approach, in order to study chain pillar loading conditions. The procedure included the effects of seam interaction and the influence of a gob model. Displacement output values obtained from the displacement-discontinuity model were used as a separate and distinct boundary-loading condition for a two-dimensional finite element model.

- Farahmand and Li (1986) developed a computer program that combined the direct boundary element method and the displacement discontinuity technique, employing a linear type element. A structural discontinuity was modeled either by a row of displacement-discontinuity elements placed along the discontinuity or a by number of boundary elements placed along both sides of the discontinuity.

2.5.4 Finite Difference Methods

Finite difference schemes can also be applied, although they are not commonly used. In this formulation, the higher derivatives of the constitutive equations are approximated, and the system is solved for discrete values. The major disadvantage of these methods is that they do not provide solutions to points other than those initially selected for discretization of the problem.

2.5.5 Finite Element Models

Finite element methods are based on interpolation functions that connect the discretized points of a given mesh and provide approximation functions for the domain between those points. This group of methods has found the most application in recent years, although modeling is not always realistic nor indicative of rock behavior, and so assumptions must be made. Researchers have employed different approaches with respect to constitutive relationships and/or convergence criteria when using finite element methods to model rock behavior. Material models occasionally used include **elastic-viscous** and **elastic-plastic**, while **linear elastic** and **non-linear elastic** formulations are applied more often. An elastic-viscous model is not appropriate for subsidence prediction, since it assumes earth as an elastic plate resting on a viscous mantle. This scale is far too large to model subsidence or ground movements over a longwall panel (Holt and

Mikula, 1984). Elastic-plastic models model rock as elastic until failure, whereupon its behavior becomes plastic. When modeling the behavior of strata around and above underground openings (i.e. mine entries, panels etc.), the following options may be incorporated in the model, depending upon the application:

- assignment of gravitational forces to intact rock elements, and modeling of the opening using **air elements**, i.e. elements with no elastic properties or gravitational loading;

- use of single-step or multiple-step loading cycles. In the first case the full load is imposed on the mesh, and the elements experience extreme forces in one step, which may result in failure modes different than those experienced when the elements are loaded at a slower rate; and

- reduction of the elastic properties of the failed elements by a fixed or proportional amount, depending upon the stress state of the element. The model must be rerun to allow for the modification of element properties. Strength values incorporated in failure criteria may also need to be scaled when using reduced elasticity values for the intact rock elements (Hsiung and Peng, 1985).

The following areas have also been identified by many researchers as crucial to finite element analysis, with respect to successful modeling of different physical problems:

- ***Determination of Properties***: Appropriate geological and geomechanical data for the various layers need to be correctly determined. These, in general, include the thickness of major strata layers and location of mining horizons. More specifically, it is important to determine, for all rock types, the properties that may be necessary for

the implementation of the failure and/or convergence criteria (e.g. Young's modulus, Poisson's ratio, Compressive and Tensile strength, etc.).

- ***Handling of Discontinuities***: Major joint sets and/or discontinuities, as well as their respective tensile and shear properties, need to be identified. Equally important is the numerical representation of these physical discontinuities in the model and their incorporation into mesh design.

  The large scale movements involved during the caving of rock strata occur mostly along pre-existing discontinuities and slippage planes. Inclusion of joint elements, therefore, has always been considered essential, if realistic conditions are to be simulated. A comparative study of joint properties (Table 2.3) has revealed great disparities between values used by different authors, while results were considered successful in each case.

  Investigations into the role of joint elements (Holt and Mikula, 1984), when applied to subsidence prediction models using numerical methods, concluded that:

  1. Joints generally contribute very little to rock mass slipping and shearing except local to an excavation or goaf (gob).

  2. Joint opening is generally confined to the immediate vicinity of the excavation or goaf areas.

- ***Design of Finite Element Meshes***: Usually the codes allow for both triangular and quadrilateral elements to be defined, although there is always consideration given to an upper limit on the number of elements and/or nodes a program can handle, both

Table 2.3 Values of Joint Stiffness by Various Authors (after Holt and Mikula, 1984)

K_s [MPa/m]	σ_n [MPa].	K_n [MPa/m]	Reference
			Goodman *et al.* (1968) by direct shear
54-350	0.7		sandstone (clean, dry open)
330-1200	3.5		
1,600-2,400	10.5		
100-300	7.6		artificial, mica-filled joints
800			wet, thick seams
6,000			closed joints
			Pratt reported similar values
10,000-100,000	10-100		Wawersik (1974) jointed triaxial sandstone
100,000	300		Brown and Swanson (1972)
43,000 ± 5,000	3.5	8,500	Rosso (1979) direct shear
49,000	7.0	80,000	
76,000	10.5	100,000	
22,000 ± 10,000	1.0-2.7	38,000	jointed triaxial
33,000 ± 15,000	3.5-8.5	95,000	
95,000 ± 30,000	7.0-18.	95,000	
0-16,000	0-1.2		
0-12,000	0-2.8		
48,000 ± 15,000	0-6.3		
			Valliappan and Evans (1980)
1,000		2,600	slightly weathered sandstone
800		1,500	slightly weathered claystone
1,200		8,000	Cramer *et al.* (1979)
200		300	Dolezalova (1979)
1,200		400	

with respect to available memory and cost of analysis. The mesh tends to be dense around critical areas (i.e. around the opening), and finer in areas least affected.

Numerical errors are associated with numerical modeling in general. Mayer *et al.* (1984) investigated the sources of error for a two-dimensional finite difference computer program designed to model strata deformation. They emphasized the point that, as the mess becomes finer, the effect of the round-off error increases. Similarly, the percentage of error is greater for small strains than for large strains, so that the number of significant figures to which the displacements must be calculated depends upon the magnitude of stress or strain.

- ***Large and Small Scale Displacements***: In general, large scale displacements are represented by elastic-plastic models that allow the individual elements to **stretch** and extend over the volume (or area) that would be occupied by a fractured element. Most finite element techniques operate under the assumption of small scale displacements, which may not always be representative of the actual conditions.

- ***Cost of Finite Element Analyses***: Cost is proportional to the number of equations that need to be solved simultaneously, the number of integration points used in the numerical integration techniques when deriving the element equations, the degree of the interpolation functions between the nodes, and sometimes, most importantly, the number of iterations necessary to achieve convergence. Increased demand for accuracy results in a significant increase in these numbers and, hence, in the cost of the analysis.

Plastic Models: These models were initially introduced for soil modeling. The Drucker-Prager model (Drucker and Prager, 1952) has been applied to modeling soil

behavior as well as rock failure. Based on the extended Mohr-Coulomb failure criteria, the Drucker-Prager criterion uses the invariants of the stress tensor, which, in combination, account for the effects of all of the principal stresses and provide a yield criterion:

$$f = \sqrt{J_{2d}} - a J_1 - K \qquad [2.13]$$

where

J_1 = the first invariant of the stress tensor S_{ii};

$J_{2d} = \frac{1}{2}(S'_{ii}S'_{jj} - S'_{ij}S'_{ij})$, the second invariant of the deviatoric stress tensor;

$S'_{ij} = S_{ij} - \frac{1}{3}d_{ij}S_{kk}$, the deviatoric stress tensor;

S_{ij} = the stress tensor, where i,j = 1,2,3;

a, K = constants.

Reported applications:

- Siriwardane (1984) has utilized the Drucker-Prager yield criterion in a recent study. The material constants that are needed can be related to the angle of internal friction and cohesion of the material. However, since no caving criterion nor a gob response curve are taken into account, it may be concluded that all of the material is modeled as elastic until yielding into plastic failure.

Elastic models: These have found extensive application, and have been in use for many years and in different variations, e.g. linear, non-linear, transversely isotropic, etc. Linear and non-linear elastic models are discussed in Chapter 3, along with the corresponding failure criteria.

Reported applications:

- A discussion on a model developed by Germanis and Valliappan (1975) was reported by Holt and Mikula (1984). It is based on a no-tension analysis employing the Von-Mises yield criterion for linear rock behavior, and on the initial stress method proposed by Zienkiewicz *et al.* (1969) for non-linear rock behavior. The method yielded 75% of the maximum subsidence values predicted by the National Coal Board curves (NCB, 1966), but the profile was markedly different from that usually observed in practice.

- A program developed at Pennsylvania State University (1974) simulates ground movement caused by an advancing face. In this program, each overburden strata layer is assumed isotropic and linearly elastic. Gob behavior is modeled by allowing broken rock to partially support overlying strata, depending upon the degree of compaction. This behavior was first modeled by Salamon (1966), and considers material behavior criteria in the gob in terms of an empirical load displacement relationship, as given below:

$$P_m = \frac{P_c\ \omega_o}{K_o(m - \omega_o)} \qquad [2.14]$$

where

P_m = the resistance of the gob;

P_c = material constant;

K_o = initial bulking factor;

ω_o = downward displacement of the contact surface;

m = extraction thickness.

- Girrens *et al.* (1982) used a modified ADINA code (Bathe, 1975) to model the effects of subsidence on ground hydrology. One method utilizes the general equations that describe fluid migration in highly deformable media, while another method models the subsidence phenomena separately, using a structural finite element code and then solving the fluid flow equations. The deformed mesh for a case study presented in their investigation verifies the observation (as discussed in Chapter 4) that the subsidence profile, even when pre-compaction has been subtracted, is not asymptotic to the original surface.

- A program developed by the Australian Coal Industry Research Laboratories (ACIRL)[3] examines the stability of mine layouts at seam level, using constant strain elements. Joints, faults, bedding planes and other discontinuities are represented by Goodman **joint elements**. An important feature of the program is its use of **laminated elements**, which can result in a more realistic representation of discontinuous joints and bedding planes by allowing elements to fail along pre-existing weakness planes located within these elements. Their use permits model simulation of fracturing above the sides of the excavation, inelastic strata movement, and simulation for small angles of draw and asymmetrical subsidence profiles (Holt and Mikula, 1984). Furthermore, the program has the ability to simulate the development of the goaf (gob) in more than one cycle, and it also incorporates a full failure stress-strain envelope, where the post-failure section is arbitrarily defined. An isoparametric version of the program was also developed. It should be noted that, in an isoparametric element, both the displacement between the nodes and its geometry are described by the same interpolation function.

---

[3] Hebblewhite 1982, Mikula 1981, as referenced by Holt and Mikula (1984).

- In a study conducted by the U.S. Bureau of Mines (Beckett, 1984), the subsidence properties of the overburden as a function of the **effective** overburden stiffness, for the geology and geometry of a particular case study with supercritical panel width, were examined. The overburden material model was assumed to be linear-elastic, while gob properties were assumed to observe a non-linear stress-strain curve. Elastic parameters (stiffness) of the immediate roof were reduced to a small percentage of the laboratory values until the obtained subsidence prediction curves were satisfactory.

- Serata and Gardner (1986) described the application of a rheologic model (REM) to model roof stresses and strains in salt mines. Their model is capable of simulating basic earth material time-dependent behaviors, including ductility, brittleness, failure, deterioration, post-failure strength, volumetric expansion (dilatancy), viscoelasticity and viscoplasticity. A "Stress Control Methodology" has been developed to help validate the models and evaluate the results of the numerical analysis.

- Sutherland (1986) reported the application of a modified finite element program to model subsidence and roof failure characteristics. The program incorporates a routine for modeling roof material failure and recompaction under a redefined bulked state. The model also allows for slip surfaces (joints), and incorporates the **ubiquitous** joint element, where the joint assigned to a specific location can assume different discrete orientations depending on the corresponding stresses. Model calibration was achieved mainly through physical simulations of mining structures (i.e. centrifuge simulation).

Chapter 3

Development of the Finite Element Analysis

3.1 Introduction

One of the approaches to calculating strata movement over underground openings is the well-established numerical technique of finite element modeling. This method, first introduced for modeling isotropic, homogeneous and elastic materials, has repeatedly been applied for modeling soil and/or rock materials, but none of these applications can be considered as a general model. This becomes apparent when one considers the complexity and non-uniformity of solid earth media, as well as the minimal information available for the sub-strata, apart from information obtained through borehole logging and/or seismic logs.

The finite element method has been previously applied for simulating geotechnical problems such as behavior of foundations, dams, etc. under load, whether compacted or uncompacted, under the assumption that the materials have properties which are either uniform or which can be mathematically described. This method has also been applied to modeling underground mining conditions with respect to stress development around pillars (Hsiung and Peng, 1985; Kripakov *et al.*, 1986; etc.), and to modeling

elastoplastic conditions such as those encountered in salt mines (Serata, 1986). In a few instances, however, (Mozumbar, 1974; Siriwardane, 1984; etc.), the method has been used in conjunction with a continuous underground opening such as that which is encountered when examining longwall mining systems. Additionally, numerous applications are reported for modeling surface deformation under different mining conditions.

Results from modeling of the overburden, employing the finite element formulation, will be used as indicators of overburden behavior and movement with respect to strata deformation mechanisms. In the process of developing a suitable model, however, different strata representation and models were examined in depth, revealing a variety of alternatives, as well as the specific advantages and disadvantages of using each. The following sections describe the general numerical formulation, as well as the particular steps associated with the development of the specific code used in this study. It should be mentioned that the base code (i.e. constitutive equation formulation and system solution), was duplicated from a program developed by Duncan *et al.* (1984). The program was developed in FORTRAN-77, and run on an IBM mainframe computer.

3.2 Mesh Generation

The domain to be modeled was arbitrarily divided into quadrilateral elements, which constituted the basic mesh. Element size tended to decrease in areas where a more accurate solution was desirable.

A typical mesh layout for analyzing surface subsidence due to underground openings was rectangular in shape, included a few underburden layers whose overall vertical extension was characteristically less than that of the overburden, took advantage of the

symmetry properties of the problem, and allowed one row of elements to account for the mined area at the seam level. For the purposes of this analysis, this type of mesh is termed a **full mesh.** In conventional mesh designs only the half-panel is modeled, the symmetry axis being in the middle of the panel and on the left side of the generated mesh. Mesh nodes within the full mesh were numbered consecutively from left to right and from bottom to top. Since the horizontal dimension of the mesh window was larger than the vertical dimension, the final system of simultaneous equations resulted in a higher bandwidth value than would result if the nodes had been numbered from bottom to top and left to right. The former, however, had the advantage of keeping the same numbering at the lower nodes when variation occurred in the number of horizontal subdivisions of the overburden layers considered.

A variation of the full mesh employed in this analysis allowed for a **caving area** above the extracted panel. In this case, elements and nodes were not generated for a specified width and height above the opening.

A third type of mesh, termed the **restricted mesh**, was generated in the initial stages of this analysis. In this case, only the area bounded by the line representing the angle of draw on the right side, and by the top of the caving zone at the bottom, was included in the mesh. Nodes located on the angle of draw were fixed, while nodes on the symmetry axis were **rollered** as in the case of the full mesh.

A **mesh generator** was developed to facilitate data entry to the main program for full meshes. Horizontal and vertical spacing of cells, position and dimensions of the opening and/or caving zone, presence of chock elements and positioning of joint elements, if any, were the required data input to the generator. The output from the generator, which included coordinates of nodal points, element connectivity data and material type, as

well as stresses attributed to each element due to gravity and tectonics, was used as direct input to the main program, and assured error-free input with respect to mesh description. A similar mesh generator was enhanced with graphics commands to allow mesh plotting on an HP 7585B plotter, driven by an HP-86B desktop computer. Restricted meshes were generated manually, due to the complexity of the element and node configuration on the sloping boundaries. More details about the mesh generator program are given in Appendix B.

3.3 Numerical Formulation

The application of finite element techniques usually requires the following steps: a) complete discretization of the domain; b) derivation of the constitutive element relationships; c) assembly of the **global** matrix; d) application of the driving mechanism (i.e. nodal forces and/or fixed displacements; e) solution of the linear system in order to calculate nodal displacements; f) evaluation of the stress state of each element; and g) checking for convergence when using a multiple iteration scheme. Application of these techniques basically relies on the use of inter-element continuity equations, in order to model a continuum. Element failure, therefore, can only be modeled by assigning **reduced** elastic properties to the specific element. In this study, a model able to handle a two-dimensional representation of a mine cross-section was formulated under the assumption of plane-strain conditions. The latter implies that: a) the thickness (or unit third dimension) is large compared to the x-y dimension (in a cartesian coordinate system); and b) loading forces are acting only on the x-y plane. Thus, it can be assumed that: a) the displacement in the z-direction (w) is negligible; and b) the in-plane displacements (u,v) are independent of z (Figure 3.1).

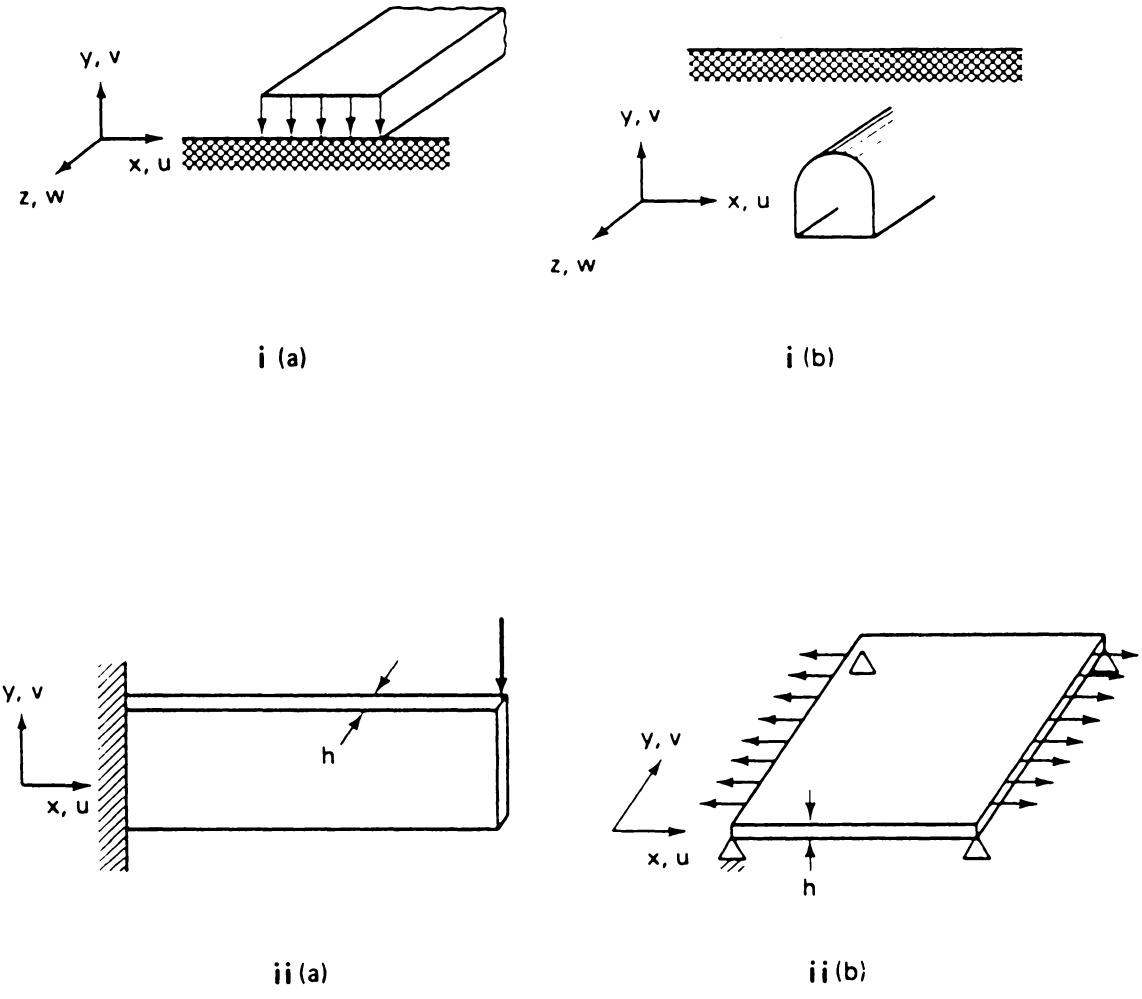

Figure 3.1 (i) Plane Strain Approximation for: (a) Strip Load; (b) Long Underground Tunnel. (ii) Plane Stress Approximation for: (a) Beam; (b) Plate [after Desai, 1979]

Employing linear approximation functions for the internodal displacement functions of four-node quadrilateral elements, and accounting for eight (8) degrees of freedom per element, the element stiffness matrix (K) is calculated as:

$$K = h \int\int_A [B]^T[C][B]\ dxdy \qquad [3.1]$$

where

- h = the thickness of the element;
- C = the elasticity matrix for plane-strain analysis related to stress and strain by $\{\sigma\} = [C]\{\varepsilon\}$;
- B = the strain-displacement matrix;
- A = the area of the element;
- σ = the two-dimensional stress state of the element (i.e. σ_x, σ_y, τ_{xy});
- ε = the strain state of the element (i.e. ε_x, ε_y, γ_{xy}).

To simplify calculations, the element stiffness matrix, (K), is transformed into a local coordinate system employing the Jacobian matrix (J):

$$K = \int_{-1}^{1} \int_{-1}^{1} [B]^T[C][B]|J|\ dsdt \qquad [3.2]$$

where s and t are the local coordinate variables.

The double integral is then numerically approximated using a four-point (two in each direction) Gauss-Legendre quadrature scheme, and K can be expressed as:

$$K = \sum_{i=1}^{m} \sum_{j=1}^{n} [B(s_i, t_j)]^T[C][B(s_i, t_j)]|J(s_i, t_j)|\ w_i w_j \qquad [3.3]$$

where

w_i, w_j = the weight functions for the quadrature approximation;

J = the Jacobian matrix expressed in local coordinates.

The resulting element stiffness matrix (K) is an 8x8 symmetric matrix for the four-node quadrilateral elements. The physical meaning of the stiffness matrix becomes apparent in Figure 3.2. The schematic diagram suggests that every degree of freedom (nodal displacement in the x or y direction) depends on the displacement of all neighboring nodes, as governed by the constitutive equation. The eight degrees of freedom of a quadrilateral element correspond to displacements u_1, v_1, ... u_4, v_4, and are represented by **local** equation numbers 1 to 8 in element (i). In this way, an elastic deformation imposed on any node of an element is coupled with all remaining degrees of freedom in this element.

3.4 Joint Elements

The joint element formulation introduced by Goodman *et al.* (1968) is much simpler than the formulation of the intact rock elements. The element can effectively be represented as a four-node, zero-width element. Stresses are expressed as linear functions of displacements, covering the two allowed degrees of freedom as shown below:

$$\begin{aligned} \sigma_j &= K_n \, \delta_n \\ \tau_j &= K_s \, \delta_s \end{aligned} \qquad [3.4]$$

where

σ_j, τ_j = the average normal and shear stresses on the joint plane;

K_n, K_s = the normal and shear stiffness coefficients;

δ_n, δ_s = the average relative displacements across the joint.

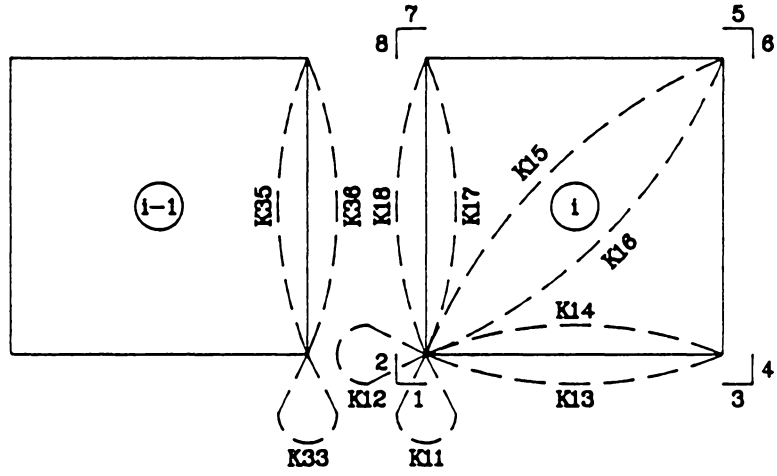

Figure 3.2 Relationship of Stiffness Terms to Nodal Equations for Quadrilateral Elements

The joint element stiffness matrix, K, is defined as:

$$K = \frac{1}{4}\int_L [D]^T[k][D]\ dx \qquad [3.5]$$

where

L = the length of the element;

k = a diagonal material property matrix expressing the joint stiffness per unit length in the normal K_n and shear K_s directions. Stress $\{\sigma\}$ is related to the property matrix by: $\{\sigma\} = [k]\{\delta\}$;

D = the relative displacement / displacement matrix for which $\{\delta\} = \frac{1}{2}[D]\{q\}$;

δ = the relative displacements;

q = the nodal displacements.

After performing the numerical integration, the element joint stiffness (K) is an 8x8 symmetric matrix, expressed as a function of K_s and K_n. Since this formulation results in a stiffness matrix with certain terms always equal to zero, an elastic deformation imposed along a certain direction is **not** coupled with all remaining degrees of freedom in the element.

3.5 Chock (Truss) Elements

Truss elements are one-dimensional elements designed to function as support elements when subject to compression (or simple springs), and can be introduced in the opening when overlap of roof and floor beds occurs. The chock element stiffness matrix (K) is expressed as:

$$K = \frac{1}{4} \int_L [D]^T [k][D]\, dx \qquad [3.6]$$

where

L = the height of the element;

k = the material property matrix (a scalar quantity equal to K_n for one-dimensional elements);

D = the relative displacement / displacement matrix.

After performing the numerical integration, chock element stiffness (K) is a 4x4 symmetric matrix with only four non-zero terms.

3.6 Gravity Forces

Nodal forces corresponding to equilibrium conditions for every element under stress can be calculated from the equation:

$$\{F\} = [K]\{q\} \qquad [3.7]$$

which is simply expressed as:

$$\{F\} = h \int\int_A [B]^T [C][B]\{q\}\, dxdy = h \int\int_A [B]^T \{\sigma\}\, da \qquad [3.8]$$

where

B = the strain-displacement matrix;

σ = the two-dimensional stress state of the element.

Additional stresses (i.e. tectonic) can be added to the stresses due to gravity, so the resulting nodal forces will include their effect as well. After transforming the double inte-

gral into local coordinates by using the Jacobian matrix, and approximating the double integral with a double summation using a four-point Gauss-Legendre quadrature, the following expression is obtained:

$$\{F\} = \sum_{i=1}^{m} \sum_{j=1}^{n} [B(s_i, t_j)]^T \{\sigma\} |J(s_i, t_j)| \; w_i w_j \qquad [3.9]$$

where

K = the global stiffness matrix (symmetric);

q = the global displacement vector;

F = the global force vector.

3.7 Assembly of the Global Matrix and Final Equations

The total number of equations that compose the linear system is, theoretically, two times the number of nodes, since every node has two degrees of freedom. Practically, however, since boundary conditions impose certain restrictions to node movement (e.g. fixed or rollered nodes), the number of equations is less than two times the number of nodes. Stiffness properties corresponding to different elements, which link the same nodes together, are summed, and the global system of equations is created according to the relationship:

$$[K]\{q\} = \{F\} \qquad [3.10]$$

For those boundary conditions, where a fixed displacement different than zero is requested, the appropriate set of equations is modified to reflect that condition.

3.8 Some Material Models and Failure Criteria

Deriving and applying the right material model and failure criteria is one of the most important steps in realistic modeling of rock or soil media. As already mentioned, the non-uniform nature of these materials and their properties dictates the use of a non-linear model where possible. A critical point is the behavior of failed material (due to tension, compression, shear or any combination), and the lack of an adequate numerical description of material disintegration. The Hookean stress-strain relationship, ($\sigma = E\,\varepsilon$), fails to describe material behavior past the plastic or failure point.

The simplest model is the **linear elastic** one, wherein the material is assumed to deform according to a constant Young's modulus and Poisson's ratio. The material can also assume a tensile mode of loading without failing. It should be noted that the term **linear-elastic model** describes the material behavior, although some researchers use the term **linear model** to denote the use of linear interpolation functions for internodal displacements. All the models analyzed in this study use linear interpolation functions, so the above term applies to material behavior. The linear elastic model may be appropriate for homogeneous materials (e.g. steel), but it is not appropriate for non-homogeneous rock, especially since rock materials exhibit very low tensile strength. This type of modeling, however, is very useful for comparison against non-linear models.

Different non-linear material models were examined for their applicability, but none provided for post-failure material behavior. The hyperbolic model (Duncan and Chang, 1970; Duncan *et al.*, 1984), mostly applicable to soils, allows for a continuous changing of the values of Young's modulus and bulk modulus, and thus of all of the elastic

properties, as a function of the stress state of each element. Young's modulus is varied according to the equation:

$$\sigma_1 - \sigma_3 = \frac{\varepsilon}{\frac{1}{E_i} + \frac{\varepsilon}{(\sigma_1 - \sigma_3)_{ult}}} \qquad [3.11]$$

where

E_1 = the initial tangent modulus;

$(\sigma_1 - \sigma_3)_{ult}$ = the asymptotic value of the deviatoric stress.

Figure 3.3 shows a hyperbolic representation of the stress-strain curve, which is assumed to become asymptotic to the deviatoric stress value of $(\sigma_1 - \sigma_3)_{ult}$. The advantage of this model is that it provides a large yield area when close to the maximum stress allowed for the element.

Another failure criterion has been recently applied (Hsiung and Peng, 1985; Tang and Peng, 1986) in order to determine failure of rock strata when incorporated into an iterative procedure. Rock elements are assumed to fail when:

$$\sigma_1 > \sigma_c + q\sigma_3 \quad \text{or} \quad \sigma_3 \leq -T_o \qquad [3.12]$$

where

σ_1, σ_3 = the principal stresses;

σ_c = the compressive strength;

q = the triaxial stress factor;

T_o = the tensile strength.

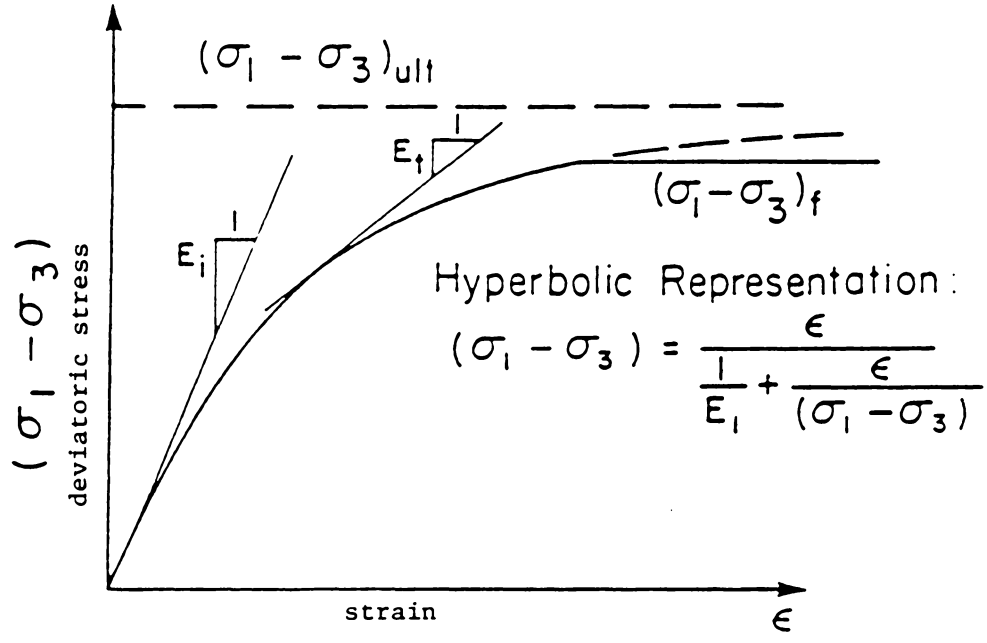

Figure 3.3 **Hyperbolic Representation of Stress-Strain Curve for Primary Loading (Duncan *et al.*, 1984)**

In situ properties were reduced when incorporated into the above criterion, and elastic properties were subsequently calculated according to the stress state of each element.

Another material model, which was defined for the purposes of this analysis, involves piece-wise linear behavior under compression, shear or tension (allowing for different elastic moduli in each segment), as well as a small tensile region (Figure 3.4). The properties assigned to the failed material are at least an order of magnitude less than those of the intact material.

The latter model was further modified so that the uniaxial stress-strain curve obtained in the laboratory could be approximated as a trigonometric function, thus providing a continuous approximation of the elastic modulus as a function of the deviatoric stress ($\sigma_1 - \sigma_3$) for the compressive region. Post-failure elastic moduli were set at 0.1% of intact rock moduli, which, however, inherently assumes that failed material can still behave elastically.

The Mohr-Coulomb and Mohr envelope criteria were used to determine whether failure occurred based on approximated values for material cohesion and angle of internal friction. Plastic yielding criteria do not really apply to rock materials which are, in general, more brittle, and have a higher compressive strength, than soils. To simplify data input, the material model was kept the same within a row of elements or layer (except, of course, when modeling the row representing the opening).

3.9 Failure-Inducing Mechanisms

Mesh deformation is calculated according to equation [3.10], as mentioned previously. This equation can be expanded into the following form:

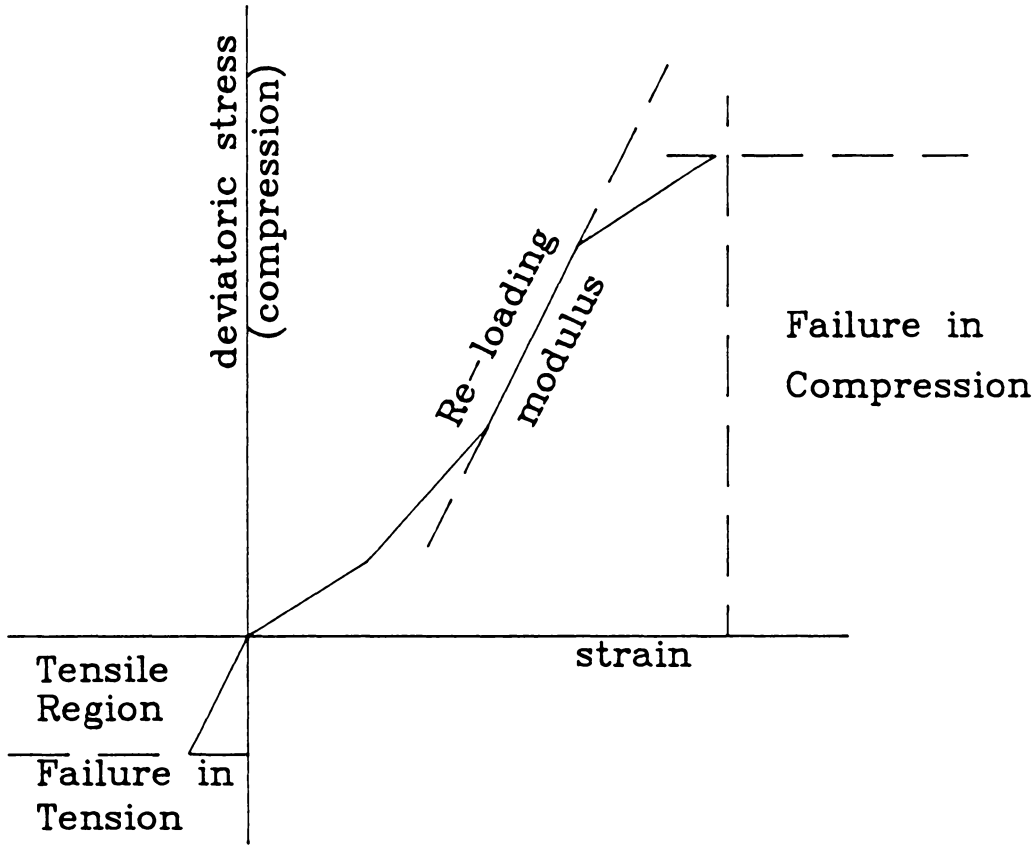

Figure 3.4 **Non-Linear Stress-Strain Model**

$$[K_1 \ \ldots \ K_n] \begin{bmatrix} q_1 \\ \ldots \\ q_i \\ \ldots \\ q_n \end{bmatrix} = \begin{bmatrix} F_1 \\ \ldots \\ F_i \\ \ldots \\ F_n \end{bmatrix} \qquad [3.13]$$

where

$K_1 \ldots K_n$ = terms of the global stiffness matrix;

$q_1 \ldots q_n$ = terms of the nodal displacement vector;

$F_1 \ldots F_n$ = terms of the nodal force vector.

When both the nodal displacement and the nodal force vectors are equal to zero, then the linear system assumes the trivial solution (i.e the displacement vector is zero), and there is no mesh deformation. When even one term of either the force or displacement vectors is non-zero, the nodal displacements can be calculated. The presence of such terms will be referred to as the **driving mechanism** or the **failure-inducing mechanism,** since they allow for either displacements or forces that induce mesh deformation.

The initial stress state of the element reflects the cumulative effect of the gravity and any tectonic stresses incorporated into the gravitational stress field. This information is required when calculating the nodal forces due to gravity, as mentioned below, although it does not participate in the calculation of the nodal displacements.

Failure induced by nodal forces: In this formulation, nodal forces (F_i) are applied to the nodes surrounding the opening, which are calculated as a function of vertical (i.e. grav-

ity) loading. To simulate the effect of gravity, forces should be applied to the upper and lower nodes in the vertical as well as the horizontal direction.

Failure due to gravity loading: In this model, the nodal forces (F_i) acting on each element due to the gravitational load sustained are calculated using equation [3.7], while nodes already fixed or rollered do not assume any loading forces. Horizontal and vertical forces should balance, except for the lack of forces on the nodes surrounding the opening, which provides the driving mechanism. This formulation, however, is subject to roof-floor overlap depending on the magnitude of the forces, as well as to slight overlap of the nodes that define zero-width joint elements, as discussed in later sections. Additionally, all of the elements will experience a slight compaction due to the net compressive force field acting upon them.

Failure induced by fixed displacement nodes: In this formulation, the nodes surrounding the opening are set to obtain a fixed amount of vertical (and/or horizontal) displacement (q_i). The global stiffness matrix must be modified accordingly, in order to reflect the elimination of these degrees of freedom.

All formulations provide the failure-inducing mechanism and achieve mesh deformation, but they exhibit different characteristics. Nodal forces may reflect the effect of gravitational forces most realistically, but do not provide control on nodal movement adequate to the prevention of extreme conditions in intact element behavior, which may result in roof-floor overlap. Fixed displacement nodes, however, can control the problem of roof-floor overlap, but may not initially provide a realistic representation of immediate roof failure. On the other hand, they provide a better overall representation of rock behavior in both the linear and non-linear formulations.

Chapter 4

Analysis and Evaluation of Different Numerical Models

4.1 General

The finite element method, when applied for modeling deformation characteristics due to underground mining, allows for elastic or plastic deformation of the individual elements that comprise the model. Subsidence phenomena, however, are inherently associated with non-elastic material behavior involving rock material disintegration bed separation, block translation and rotation, etc. Conventional finite element techniques are not suitable for describing such phenomena, since they are mainly based on element elasticity and interelement connectivity. Different devices, however, employed with finite element techniques, are known to counteract these weaknesses, resulting in an elastic approximation of inelastic phenomena. These devices include the use of different types of elements (i.e. joint, laminated[4], truss, etc.), that allow strata separation and/or recontact, gob and support system modeling etc. These, coupled with the varying volumetric

[4] developed and used by the ACIRL (Holt and Mikula, 1984)

expansion of the elements which depends upon their elastic properties, model the bulking of the failed material, while still exhibiting an elastic behavior.

Most of these models use multiple iteration schemes, in which elements are examined for possible failure, whereupon they assume lower properties. It is possible that the failure criterion employed might not sufficiently distinguish between different types of failure (i.e. shear, compressive, tensile, etc), thus forcing the model to follow a deformation pattern that will yield the right surface deformation profiles. Magnitudes of properties assigned to failed elements may also play a significant role in mesh deformation characteristics. Park and Ash (1986) reported that, for their application, only elements experiencing high shear were assumed to fail (Figure 4.1).

4.2 Parametric Evaluation Reported by ACIRL

In a series of mathematical modeling investigations carried out by ACIRL (Holt and Mikula, 1984), involving the study of the effects of overburden depth and joint pattern variation for different case studies, the following were observed:

- The use of laminated elements in the model had by far the greatest effect on subsidence.
- Doubling the primitive stress magnitude in the vertical direction resulted in doubling of the maximum calculated subsidence.
- Reducing the moduli of all coal and rock elements by a factor of 2 resulted in an increase in maximum subsidence by a factor of 1.75. The fact that the behavior of the model was not fully linear is probably attributable to the presence of non-linear entities, such as the laminated elements.

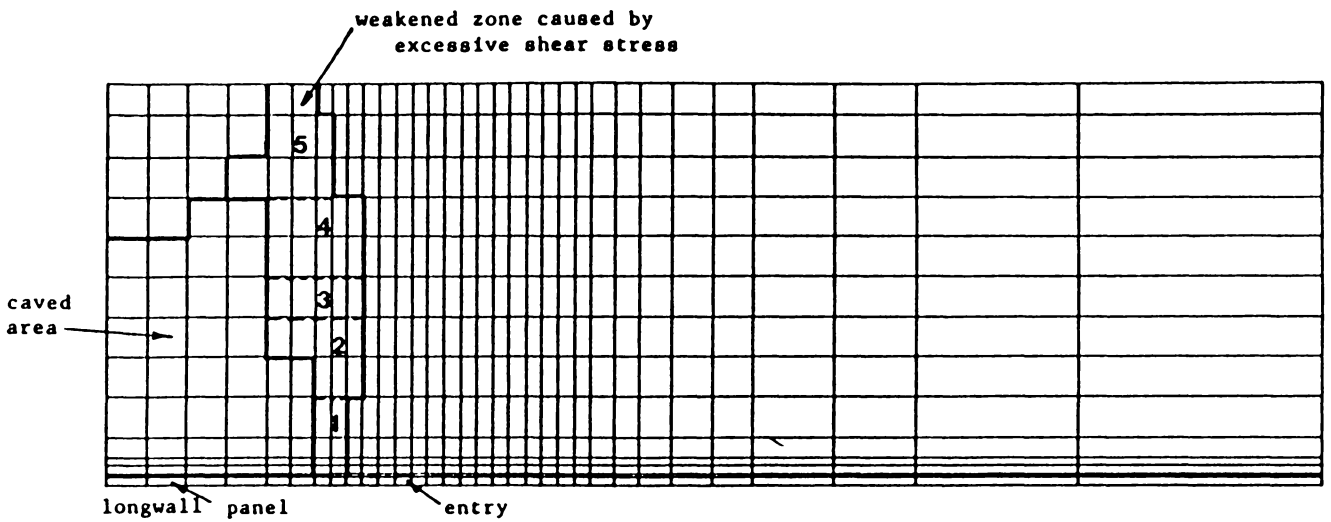

Figure 4.1 **Zones of Failed Material as Identified by Park and Ash, 1986**

- The study of joint pattern variation revealed that models with parallel bedding plane joints showed greater subsidence than did models in which intersecting joints divided the rock mass into large vertical blocks.
- When the overburden thickness was doubled, maximum subsidence values were reduced to about 80%.
- A change in anisotropy, or in the ratio of vertical to horizontal primitive stresses, had very little effect on subsidence.

It should be noted that strain prediction by this model was not satisfactory in any of the case studies investigated in the project.

4.3 Preliminary Analysis Using the ADINA Code

A study of the formulation and behavior of a simplistic model through the ADINA code (Bathe, 1975) was undertaken initially for a preliminary parametric analysis of surface subsidence. The analysis was conducted following a procedure already used for modeling surface subsidence effects.

The grid (Figure 4.2) covered a 650 x 1000 foot (width x height) cross-sectional area, and was divided into horizontal layers. A 4-foot thick coal seam was assumed at roughly the middle of the model grid. The underburden was modeled as shale, while the overburden consisted of layers of shale and sandstone capped by a layer of topsoil. Surveyed subsidence curves were already available for this particular case study. Both the maximum subsidence value and the profile shape were analyzed for each of the subsequent runs of the model. The parameter values used for the analysis are shown in Table 4.1.

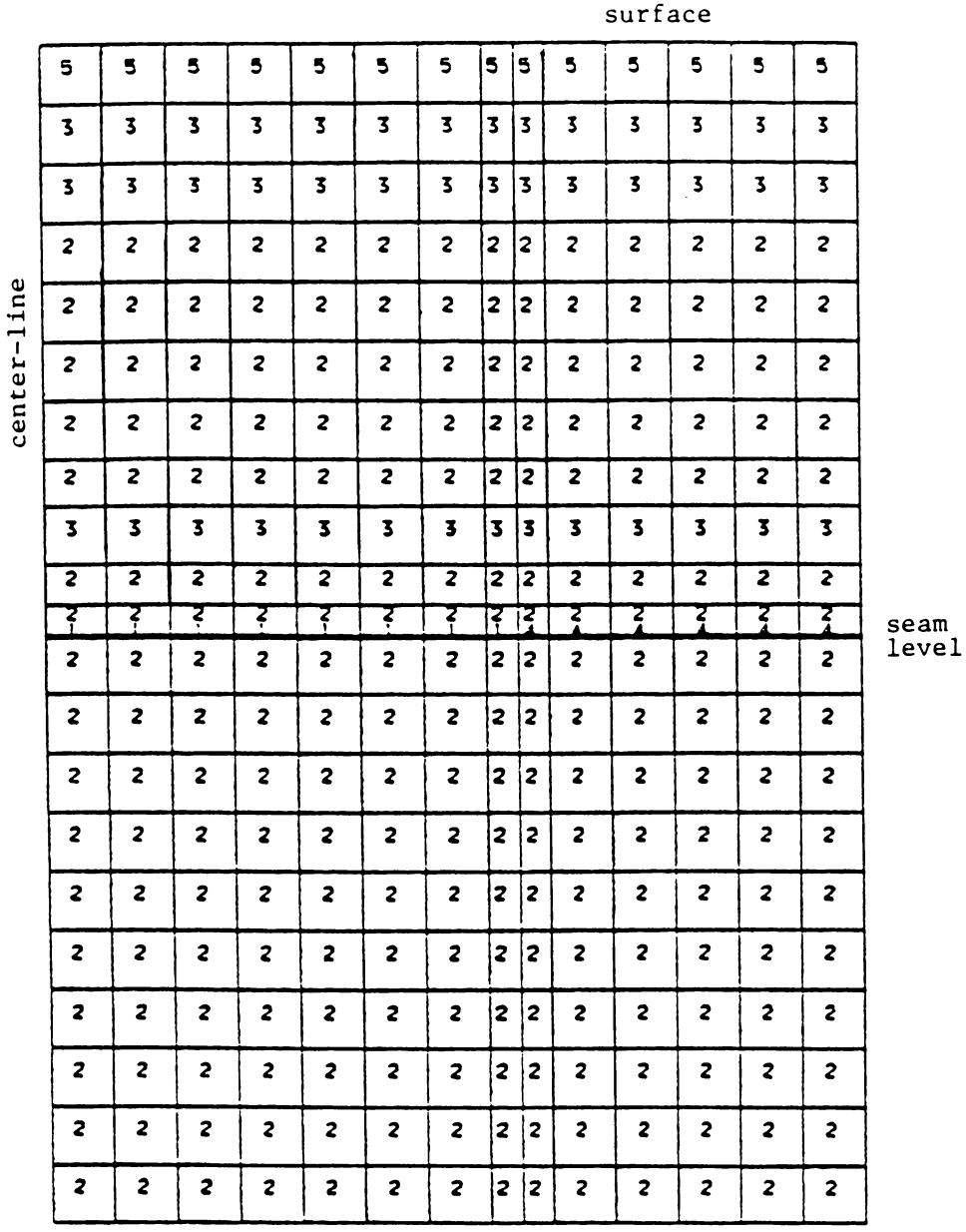

Figure 4.2 Mesh Generated during the Preliminary Analysis Using the ADINA code (Key: 1 = opening, 2 = shale, 3 = sandstone, 4 = coal, 5 = topsoil)

Table 4.1 Material Properties for the ADINA Model

Material	Density [lb/in^3]	Young's Modulus [psi]	Poisson's Ratio
shale	0.1	350,000	0.20
sandstone	0.1	600,000	0.20
coal	0.1	200,000	0.20
soil	0.1	70,000	0.20
air	0.0	1	0.00

The type of analysis performed was essentially linear, although it was treated as non-linear because it involved the **birth and death** process for elements in the minable section. This process describes the death of **rock** elements and birth of **air** or **gob** elements with prescribed properties.

Different types of parametric analysis were attempted under gravity loading conditions, yielding the following results:

- Doubling the size of the grid in one dimension, from 25 x 50 feet to 50 x 50 feet, had very little effect on the subsidence or roof convergence curve.
- Changing the opening width affected both the maximum subsidence value and the profile shape, so that the new profile curve was not a mere translation of the previous one, as seen in Figure 4.3.
- Reducing the underburden by 80% reduced the maximum subsidence, but the profile shape remained the same when translated upwards.
- Reducing the material properties to model very soft strata yielded very large subsidence values, accompanied by an extensive overlap of the roof and floor profiles of the opening. It was suggested that use of truss elements (one-dimensional elements with prescribed stiffness) would overcome this problem. Figure 4.4 compares the curves for a 20% reduction in material stiffness for all layers in the grid.

In all of the above cases, the driving mechanism was generated by assigning forces due to gravity to all elements except the elements in the opening. Thus, the model had to be run once, without generating an opening, in order to determine the amount of strata pre-compaction. The latter was subsequently subtracted from the displacement values calculated when the opening was initiated. However, even when the panel halfwidth was 4% of the total horizontal mesh dimension, the subsidence profile was never asymptotic

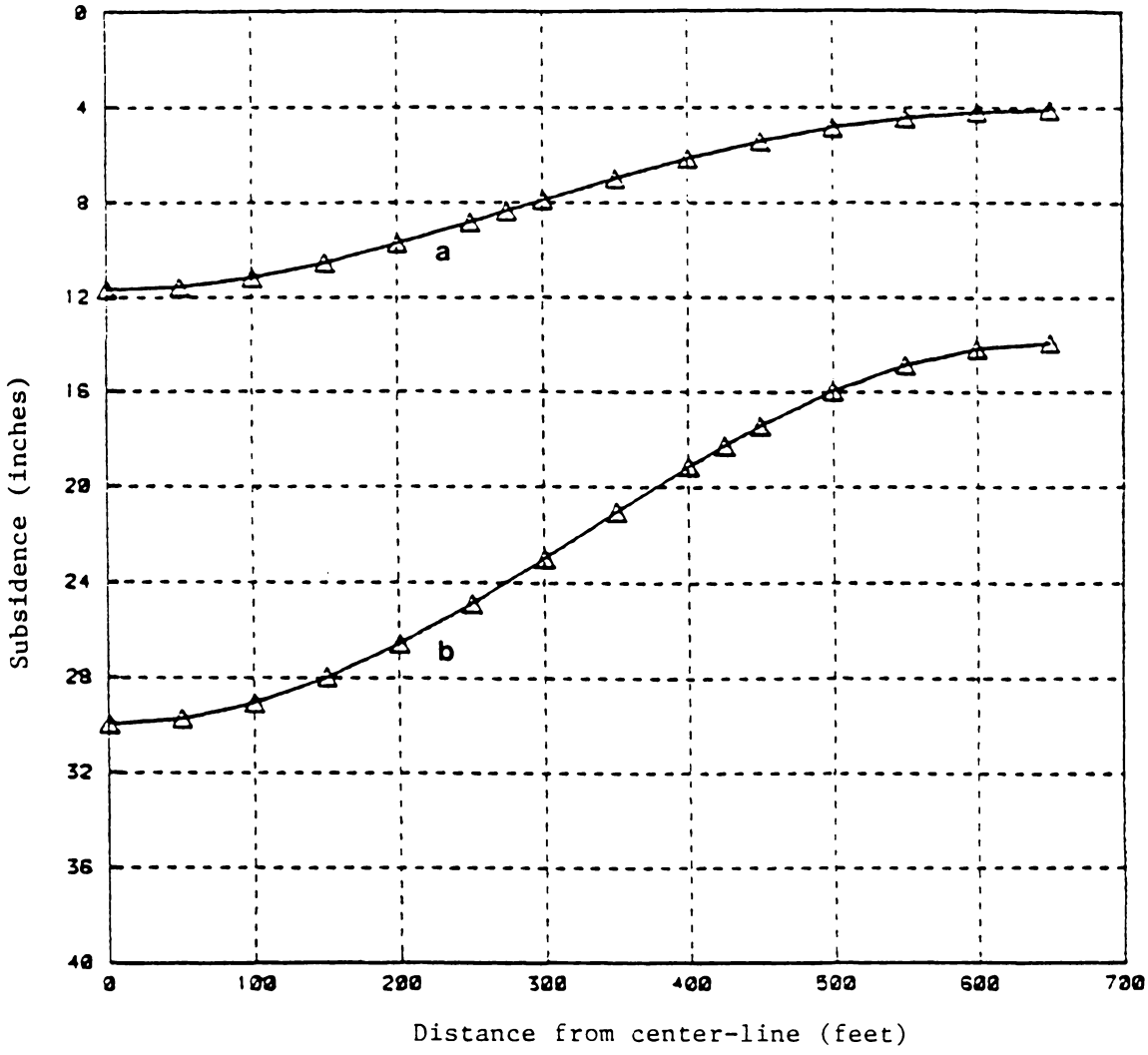

Figure 4.3 **Comparison of Profile Shapes for Different Openings: (a) 275 feet; (b) 425 feet**

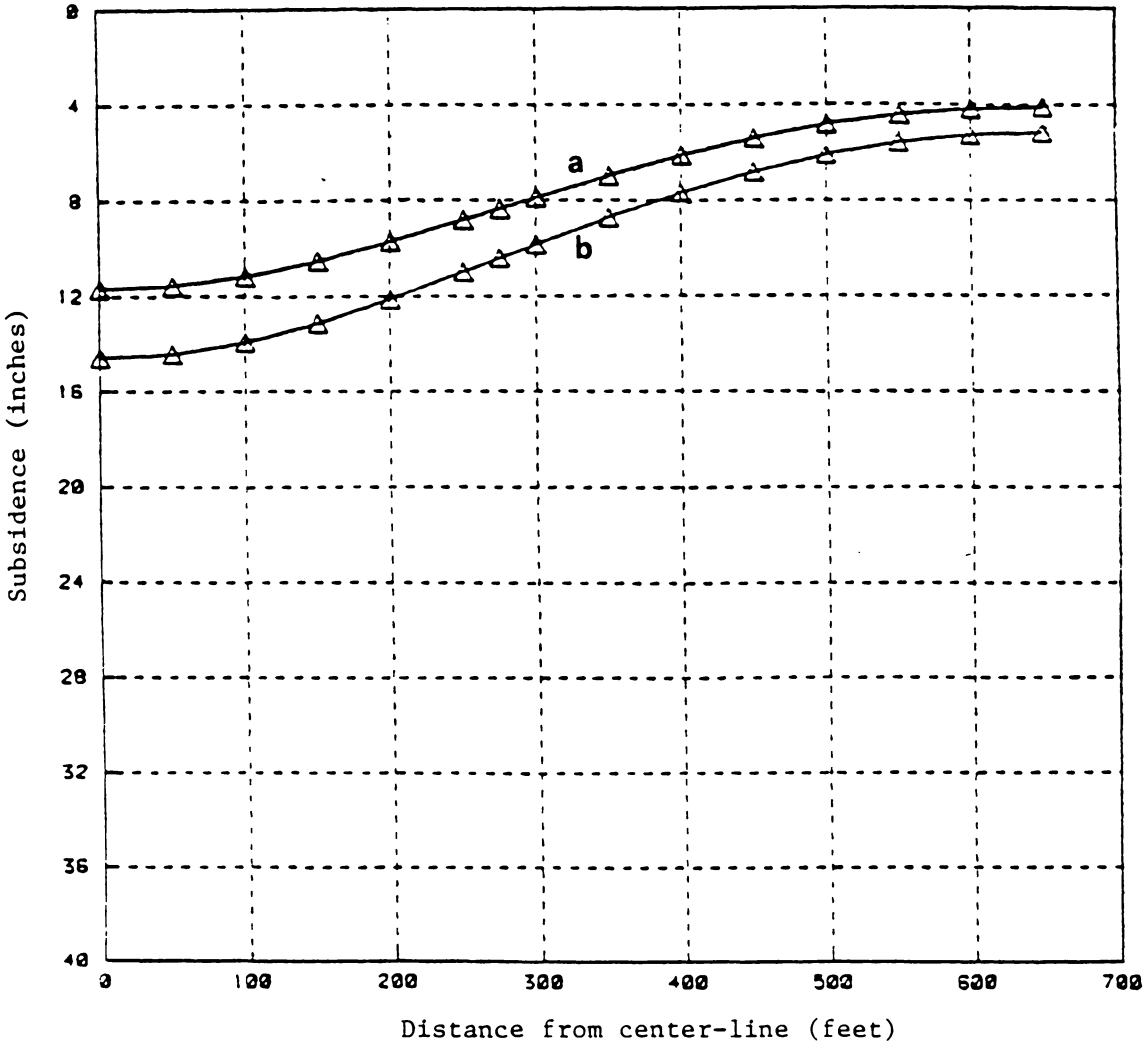

Figure 4.4 Comparison of Profile Shapes for 20% Reduction in Material Stiffness (curve 'b')

to the surface. It leveled off at some value below the surface, which was a function of panel dimensions and material properties.

4.4 The FEASD code

A finite element code was developed based on a modified FEADAM84 code (Duncan *et al.*, 1984). The program included formulations for joint and chock elements, options to calculate nodal forces due to gravity, and different material models as described in Chapter 3. This new code was named FEASD (Finite Element Analysis of Strata Deformation), and retained only the basic solution routines, memory and file management techniques, and quadrilateral element derivations of the FEADAM84 code. Data input routines were simplified, since most data input sequences came directly from the generator program, as mentioned previously. The program could be run under a preset number of iterations (1, 2 or more) and under a variety of material models, which in turn could be adjusted to reflect changes in the properties between iterations.

More details on the structure of the code, and its features, are presented in Appendix C.

4.5 Preliminary Analysis Using the FEASD Code

A study of the characteristics of linear and non-linear models, using the FEASD code was undertaken at this stage, in order to determine mesh deformation patterns under different conditions. Failure was initiated through either nodal forces or nodal displacements, applied to the nodes surrounding the opening. Material properties were manipulated by the material models in effect for multiple iteration schemes, but re-

mained unchanged for single iteration schemes. The geometry of the mesh was also varied, deviating from the typical rectangular cross-section used in most applications, and results were compared.

4.5.1 Effect of Material Models and Properties on Mesh Deformation

Although quite a few applications of finite element codes to study the behavior of underground workings are described in the literature, only a few report in detail the elastic and geomechanical properties assigned to the different elements, the property reduction factor used, and the failure criterion applied.

For the purpose of comparing the different models, the property Reduction Factor is defined as:

$$\text{Reduction Factor} = \frac{1}{\text{Scaling Factor}} \qquad [4.1]$$

where the Scaling Factor is the percentage of the original value used for a particular modeling application. Table 4.2 presents values for the elastic and geomechanical properties used in different case studies and their respective reduction factors, when applicable. It is evident that the magnitudes of these properties vary considerably, when considering the fact that most claim to achieve a good fit of the measured to the predicted data.

4.5.2 Deformation under Nodal Forces

The effects of the different material models under single and multiple iteration schemes and the magnitude of the material properties, were examined for a typical longwall panel

Table 4.2 Material Properties Reported in the Literature

Code Name	Material	E [psi] (MPa)	ν	C_s [psi] (MPa)	T_o [psi] (MPa)	Cohesion [psi] (MPa)	φ [degrees]	Density [lbs/cf]	RF	Failure Criteria and Properties	Reference and Application
NASTRAN	Overburden Strata										
	Coal	$5\ 10^5$ (3450)	0.20	4500 (31)	170 (1.17)	-	-	100	5	$\sigma_1 \geq \sigma_c + q\sigma_3$ or $\sigma_3 \leq -T_o$	Hsiung and Peng (1985)
	Sandstone	$5\ 10^6$ (34500)	0.17	18070 (124.6)	800 (5.52)	-	-	162	5	RF applied to C_s, T_o	Chain Pillar Design for Longwals
	Shale	$2\ 10^6$ (13800)	0.25	14800 (102.1)	230 (1.59)	-	-	168	5	E_{failed} = 1/2, 1/10, 1/20 of E_{intact}	
	Clay Shale	$2.7\ 10^6$ (18000)	0.30	16500 (113.8)	500 (3.45)	-	-	162	5	ν_{failed} = 0.05	
	Packed Gob Material Properties										
	Sandstone	62500 (431)	0.08	-	-	-	-	145	-	E_{gob} = 1/57-1/100 of E_{intact}	
	Shale	25000 (172)	0.08	-	-	-	-	145	-		
	Coal-like	6250 (43.1)	0.08	-	-	-	-	145	-		
NASTRAN	Overburden Strata										
	Coal	$3.62\ 10^6$ (25000)	0.25	850 (5.9)	70 (0.48)	-	-	83	4	$\sigma_1 \geq \sigma_c + q\sigma_3$ or $\sigma_3 \leq -T_o$	Tang and Peng (1986)
	Sandstone	$15.1\ 10^6$ (104000)	0.17	6590 (45)	910 (6.2)	-	-	163	4	RF applied to C_s, T_o	Study of Surface Fractures
	Gray Shale	$8.7\ 10^6$ (60000)	0.19	1870 (13)	197 (1.36)	-	-	161	4		
NASTRAN	Overburden Strata										
	Coal	$1\ 10^5$ (690)	0.30	1193 (8.23)	336 (2.32)	-	-	-	-	$\sigma_1 \geq \sigma_c + q\sigma_3$ or $\sigma_3 \leq -T_o$	Hsiung and Peng (1986)
	Sandstone	$1.12\ 10^6$ (7724)	0.17	11970 (82.6)	1570 (10.83)	-	-	-	-	E_{failed} = 1/10 of E_{intact}	Study of Floor Heave (Case Study #2)
	Gray Shale	$3.5\ 10^5$ (2414)	0.25	2635 (18.2)	946 (6.5)	-	-	-	-		

Table 4.2 Material Properties Reported in the Literature (continued)

Code Name	Material	E [psi] (MPa)	ν	C_s [psi] (MPa)	T_o [psi] (MPa)	Cohesion [psi] (MPa)	φ [degrees]	Density [lbs/cf]	RF	Failure Criteria and Properties	Reference and Application
NASTRAN	Overburden Strata										
	Overburden	-	-	-	-	-	-	-	1.5	Shear Failure RF applied to E (Stress-state Approach)	Park and Ash (1986)
ADINA	Overburden Strata										
	Coal	$4\ 10^5$ (2766)	0.25	1576 (10.9)	120 (0.83)	517 (3.57)	38	-	2	RF applied to E	Beckett (1984)
	Sandstone (average)	$5\ 10^6$ (34500)	0.15	16350 (112.8)	1340 (9.25)	2410 (16.6)	58	-	5-20		Subsidence Modeling
	Shale	$1\ 10^6$ (6900)	0.15	-	-	-	-	168	2-5		
QADFIN	Overburden Strata										
	Coal	$2.5\text{-}2.9\ 10^5$ (1700-2050)	0.32-0.35	-	58-145 (0.4-1.0)	188-435 (1.3-3.0)	-	-	-		Holt and Mikula (1984)
	Sandstone	$3.6\text{-}11.6\ 10^5$ (2500-8000)	0.25-0.38	-	116-623 (0.8-4.3)	145-1450 (1-10)	-	-	-		Subsidence Modeling (Parametric Analysis)
	Carb. Shale	$2.1\text{-}7.9\ 10^5$ (1435-5500)	0.25	-	58-507 (0.4-3.5)	145-1014 (1.0-7.0)	-	-	-		
	Shl./Sand.	$3.3\text{-}3.6\ 10^5$ (1435-5500)	0.19-0.33	-	72-174 (0.5-1.2)	290-1304 (2.0-9.0)	-	-	-		
ADINA	Overburden Strata										
	Coal	$2.0\ 10^5$ (1379)	0.30	4000 (27.6)	-	-	30	-	Yf	$\sigma_F = C + \sigma_c\beta$ $\beta = \frac{1 + \sin\varphi}{1 - \sin\varphi}$	Kripakov *et al.* (1986)
	Shale	$4.0\ 10^5$ (2758)	0.20	-	-	-	-	-	-	$Sf = \sigma_F/\sigma_{max}$ $Yf = E_e/E_o$	Multi-seam interaction
	Gob	20000 (138)	0.40	-	-	-	-	-	-	$Yf_{t+1} \leq Sf_t Yf_t$ $\nu_i, C_i = f(Yf)$	

cross-section. The grid (Figure 4.5) covered a 1000 x 600 foot (width x height) cross-sectional area, and was divided into horizontal layers. A 4-foot thick coal seam was assumed at roughly 100 feet from the bottom of the grid, allowing for 500 feet of overburden material.

The different formulations discussed below apply to **full** meshes deformed under the application of nodal forces (or gravitational loading, which is translated into nodal loading) to the nodes surrounding the opening.

Linear Elastic Formulation: Mesh deformation was entirely dependent upon the elastic properties assigned to the intact rock elements. Since the magnitude of the nodal forces that induced roof collapse was a function of the overburden thickness and/or the primitive stress conditions, their magnitude was easily calculated for a given mesh geometry. Surface deformation curves generally exhibited a much smoother pattern than did the typical curves for the same geometry and overburden properties, extending all the way to the right boundary of the mesh, which was designed to be beyond the influence zone of the excavation. This indicated a gradual absorption of the failure-inducing mechanism by the whole domain, and a flow of material towards the opening from both the overburden and underburden layers. Surface deformation (expressed as node displacement) was directly proportional to the magnitude of the elastic properties. Although different strata properties were used for the individual layers identified in the lithologic column, it was difficult to relate values obtained in the laboratory to in situ conditions, without an appropriate reduction factor. Reducing the values of the elastic properties of the coal and rock elements, however, could cause roof-floor overlap, since the nodes on upper and lower boundaries of the opening were not restricted in any way.

409	410	411	412	413	414	415	416	417	418	419	420	421	422	423	424	425	426	427	428
389	390	391	392	393	394	395	396	397	398	399	400	401	402	403	404	405	406	407	408
369	370	371	372	373	374	375	376	377	378	379	380	381	382	383	384	385	386	387	388
349	350	351	352	353	354	355	356	357	358	359	360	361	362	363	364	365	366	367	368
329	330	331	332	333	334	335	336	337	338	339	340	341	342	343	344	345	346	347	348
309	310	311	312	313	314	315	316	317	318	319	320	321	322	323	324	325	326	327	328
289	290	291	292	293	294	295	296	297	298	299	300	301	302	303	304	305	306	307	308
269	270	271	272	273	274	275	276	277	278	279	280	281	282	283	284	285	286	287	288
249	250	251	252	253	254	255	256	257	258	259	260	261	262	263	264	265	266	267	268
229	230	231	232	233	234	235	236	237	238	239	240	241	242	243	244	245	246	247	248
209	210	211	212	213	214	215	216	217	218	219	220	221	222	223	224	225	226	227	228
189	190	191	192	193	194	195	196	197	198	199	200	201	202	203	204	205	206	207	208
169	170	171	172	173	174	175	176	177	178	179	180	181	182	183	184	185	186	187	188
149	150	151	152	153	154	155	156	157	158	159	160	161	162	163	164	165	166	167	168
129	130	131	132	133	134	135	136	137	138	139	140	141	142	143	144	145	146	147	148
109	110	111	112	113	114	115	116	117	118	119	120	121	122	123	124	125	126	127	128
89	90	91	92	93	94	95	96	97	98	99	100	101	102	103	104	105	106	107	108
61	62	63	64	65	66	67	68	69	70	71	72	73	74	75	76	77	78	79	80
41	42	43	44	45	46	47	48	49	50	51	52	53	54	55	56	57	58	59	60
21	22	23	24	25	26	27	28	29	30	31	32	33	34	35	36	37	38	39	40
1	2	3	4	5	6	7	8	9	10	11	12	13	14	15	16	17	18	19	20

Figure 4.5 Full Mesh Layout and Element Numbers Used in the FEASD code

Linear Elastic Formulation with Joint Elements: In this case, joint elements were introduced between overburden layers in an attempt to slacken the rigidity of the mesh. Initial joint properties (i.e. normal and shear joint stiffness) were comparable in magnitude to solid element properties.

The presence of **non-failing**, zero-width joint elements between layers of materials, had little effect on the total subsidence observed. The largest part of vertical deformation generated was proportional to intact element thickness, so joint elements (which by definition are zero-width elements) did not contribute significantly to vertical displacements. Predicted surface deformation profiles were almost identical to those generated without the use of intact joints.

Non-Linear Elastic Formulation: This formulation involved the execution of at least two iterations. In the first iteration, the same properties used for the linear elastic models were assigned. Then the current stress state of each element was calculated, based on the strain displacement matrix and/or the initial stress state, and was subsequently compared to the initial stress state. A specific material model (i.e. piece-wise linear, hyperbolic, etc.) was then used along with an appropriate failure criterion (i.e. Mohr-Coulomb) to adjust the material properties of each element according to a continuous or stepped function. Surface movements expressed in both horizontal and vertical node displacements were **not** proportional to the magnitude of the elastic properties, since these changed after every iteration. Typically, failure was detected for the elements over the opening, and their properties were reduced according to the material model. This, however, resulted in excessive movement of these nodes, causing roof-floor overlap and, at the same time, reducing the **impact** of the driving mechanism to higher layers, and

thus reducing the downward movement of the surface nodes. Surface deformation profiles still extended over the expected area of influence.

Non-Linear Elastic Formulation with Joint Elements: The properties of the joint elements for which excessive relative movement was detected after the first iteration were reduced by approximately three orders of magnitude (0.1%). It was determined that, when the properties of the failed joints were set to zero, inter-element continuity was disturbed and the numerical system (equation [3.10]) was unstable. Additionally, the impact of the driving mechanism was diminished between failed joints, so that the higher layers (elements) in the overburden sequence would not experience their appropriate share of nodal forces. Finally, since inter-layer continuity was reduced, the lower overburden layers had to **absorb** the whole impact of the forces assigned to the opening nodes, which resulted in very high nodal displacement values, causing roof-floor overlap.

By introducing **failing** joint elements, gaps developed between layers, and the total vertical displacement observed on the surface was less than that calculated for the intact case. The magnitude of the failed joint properties was directly related to the transmission of the failure-inducing mechanism from the lower to the upper element rows. Predicted surface deformation profiles, however, still showed considerable movement outside of the expected influence area.

Linear Elastic Formulation with Chock (Truss) Elements: In this formulation, one-dimensional chock elements were inserted between the nodes surrounding the opening. Initially the chock elements remained inert (i.e. the corresponding stiffness matrix was zero). After the first iteration was completed, the nodes corresponding to the chock elements were examined for overlap. Initial stiffness properties comparable to the average

stiffness properties of the layer were then assigned to the affected chock elements. Once one chock element was activated, however, the rest were also stiffened in order to achieve uniform loading of the upper layers. The system was solved again, and chock stiffness properties were incremented if overlap persisted. This option was only implemented when there was a need to compensate for the excessive forces introduced to initiate failure, or when the elastic properties of the immediate roof were very low.

The disadvantage of utilizing chock elements, whose action was determined by roof convergence at the end of each iteration, was that nodes without any support exhibited excessive movement compared to those with activated chock elements (especially under high loads), resulting in an uneven roof convergence curve.

4.5.3 Deformation under Nodal Displacements

In this formulation, the failure-inducing mechanism was provided by assigning a downward vertical displacement to the nodes surrounding the opening. It was, however, necessary to establish a a roof convergence curve for the width of the opening. Initially, roof convergence curves were defined assuming a complete collapse of the immediate roof and the subsequent filling of the extracted area. In other words, for an extraction height of 6 feet, roof convergence was set to 5.90 feet for all nodes except those close to the rib of the excavation. In such a case, roof was assumed to move less due to the support provided by the intact rib, so convergence was reduced for the last 2 nodes before the rib, in order to achieve a smoother transition between simulated roof failure and roof bending close to the rib. The shapes of the roof convergence curves had a pronounced effect on the surface deformation curves obtained, as will be discussed in later sections. This formulation eliminated the need for chock elements, since roof and/or floor movement was preset according to an assumed failure line.

Linear Elastic Formulation: Mesh deformation was dependent on the shape of the roof convergence curve. The introduction of **fixed** nodal displacements for certain nodes imposed additional restrictions to the model, in the sense that certain degrees of freedom (i.e. linear equations) were eliminated from this system, compared to the system formulated for nodal forces as the **driving** mechanism. Due to this reduction in degrees of freedom, the model seemed to be insensitive to a reduction of the Young's modulus of the overburden layers, although changes in the Poisson's ratio of the layers seemed to have a small effect on the surface subsidence deformation profiles. Predicted surface deformation profiles, however, still showed considerable movement outside of the expected influence area.

Linear Elastic Formulation with Joint Elements: Mesh behavior associated with linear elastic formulations with joint elements was similar to that observed for deformation under nodal forces, although roof-floor overlap was not possible due to the restrictions imposed by the fixed nodal displacements.

Non-Linear Formulation: Since the system appeared to be insensitive to changes in the elastic properties of the overburden, multiple iteration schemes that reduced the properties of the failed intact and/or joint elements did not affect mesh deformation in any significant way. Additionally, a reduction of the surface subsidence effects was also observed when the properties of the elements surrounding the opening were selectively reduced.

Conclusions: The introduction of failing joint elements, detection of failed elements and reduction of their properties was expected to simulate actual conditions and produce a surface subsidence profile matching those empirically predicted for the panel analyzed.

The effort, however, cannot be considered as having been successful, since the method was too sensitive to the magnitudes of the nodal forces applied and the elastic properties used. As already mentioned, surface subsidence curves generally exhibited a much smoother pattern than did the typical measured curves. The flow of material towards the opening, primarily from the overburden layers, could not be contained within the theoretical influence area as represented in the schematic of Figure 4.6. Additionally, the different failure criteria and property reduction methods did not prove successful in producing the desirable surface effects.

Examination of the effects of modifying the elastic properties of the material (i.e. Young's modulus, Poisson's ratio, bulk modulus, cohesion, etc.), on the behavior of a **full** mesh, revealed that:

- Elastic material compaction is proportional to element thickness and elastic modulus.
- An increase in the Poisson's ratio reduces the volumetric strain of the material, and, thus, results in a slightly higher maximum subsidence value.
- When using the Mohr-Coulomb failure criterion, an increase in the cohesion and/or angle of internal friction modifies the failure criterion and, therefore, elements may fail at different stress levels than in previous cases.
- Use of the hyperbolic model resulted in unusually high values for the Poisson's ratio, calculated from the reduced properties of the failed material.

It was also evident that the surface deformation patterns needed to be restricted, within the expected area of influence. The failure criteria examined did not establish failure zones at locations that should theoretically be present and, therefore, were not useful in an iterative scheme. Additionally, when using **fixed** displacements as the failure-inducing

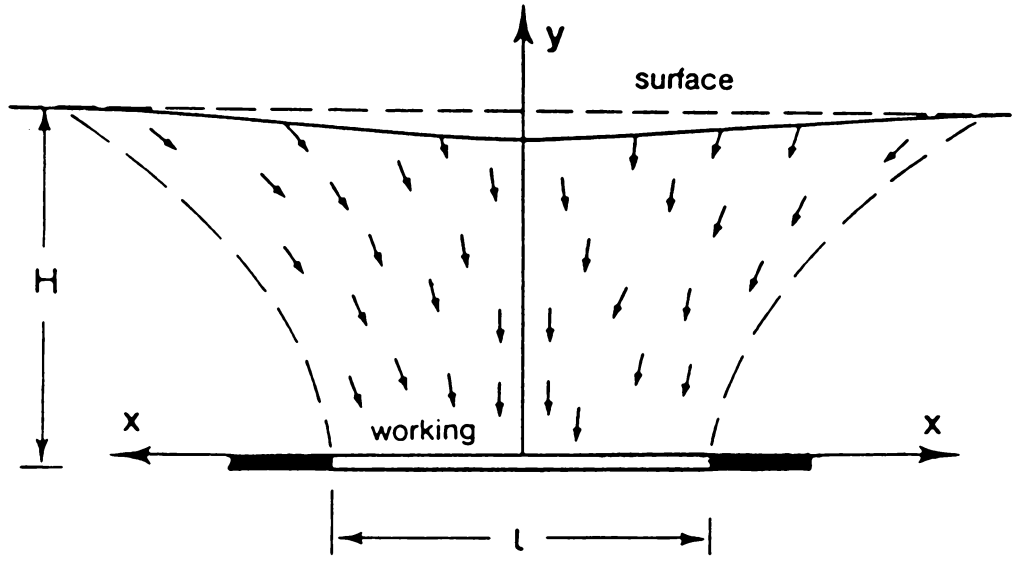

Figure 4.6 **Theoretical Flow of Material towards the Working Area**

mechanism, mesh deformation appeared to be less sensitive to the magnitudes of the elastic properties.

4.5.4 Effect of Mesh Geometry on Mesh Deformation

As previously mentioned, strata deformations above underground extractions are phenomena inherently associated with non-elastic material behavior involving rock material disintegration, bed separation, block translation and rotation, etc. and therefore, elastic equations have difficulty in describing this behavior. In an attempt to model only the part of the overburden associated with elastic deformations, the geometry of the mesh was modified, and the results are analyzed below. In all cases, a **fixed** displacement formulation was employed so that all results could be comparable.

Analysis Using a Full Mesh: This case has been fully analyzed in the previous sections, but the following comments are appropriate with respect to model behavior. Although the horizontal mesh dimension extended beyond the influence zone, it has been shown that vertical displacements of the surface nodes could still be non-zero in areas theoretically unaffected by the underground disturbance. This can be attributed to the fact that there was enough free-to-move material surrounding the opening, which tended to move both downwards and sideways when closure was initiated, in order to fill the void. Since the material model was constant along a row of elements, and since there were no fault or joint lines interrupting the continuity of the layer, the initiated movement was only restricted by the boundary conditions on the mesh sidelines. Also, surface deformation was directly related to the magnitude of the nodal displacements inducing failure, and to the shape of the imposed deformation on the immediate roof.

Analysis Using a Full Mesh with a Disturbed Zone: Strata deformation was assumed to be inelastic within the caved zone (immediate roof) and part of the fractured zone, where large displacements and rock failure are known to occur. The term **disturbed zone** was introduced to describe the area above the opening, where inelastic strata behavior may be expected. Therefore, if elements corresponding to the disturbed zone were not included in the mesh formulation, this mesh could be assumed to deform under elastic conditions. Another roof convergence curve, however, needed to be defined, applicable to that portion of the roof. It was evident that main roof movement would be less than that of the immediate roof, but no information existed with respect to its magnitude either in the vertical or horizontal directions. Surface deformation profiles obtained were still not considered satisfactory, since movement extended beyond the influence zone.

Analysis Using a Restricted Mesh with a Disturbed Zone: In this formulation, the line connecting the point on the surface where zero subsidence is observed (draw point) to the rib of the excavation constituted the right boundary of the modeled area. This line was assumed linear, for simplicity, although many researchers have proposed alternate shapes. For example, the following equation estimates the shape of the bounding curve as a function of geometric and empirical parameters (Gren, 1983):

$$r_z(z) = r \left[\frac{z}{h}\right]^n \qquad [4.2]$$

where

z = the distance from the top of the seam;

r_z = the horizontal offset of the bounding curve from the rib as a function of z;

h = the depth of the excavation;

$n = \sqrt{2\pi} \tan \beta$;

β = the angle of influence.

Figure 4.7 shows the different types of curves obtained for $n < 1$, $n = 1$ and $n > 1$. The curve resulting for $n > 1$ was incorporated into this model. Additionally, a disturbed zone was introduced to eliminate the inelastic behavior of the immediate roof, as explained earlier. The resulting mesh was termed **restricted** (Figure 4.8), since movement was not allowed outside of the theoretical influence area. The following were assumed when formulating the restricted meshes:

- Strata movement outside of the area bounded by the line defined by the angle of draw is minimal; therefore, the mesh was extended up to that line where fixed nodes in both the x- and y-direction were introduced.
- The line defined by the angle of draw can be modeled either as a straight line or as a concave or convex curve passing through two fixed points, i.e. the point of zero subsidence on the surface and the rib of the excavation.
- Fracturing and non-elastic deformations in the immediate roof occur within a zone bounded by a line extending from the rib to the maximum caving height in the middle of the panel. The elastically deformable region of the overburden is then bounded by that line, which can be assumed straight, for simplicity, or curved, resembling that of a dome or pressure arch.

In general, these models had less degrees of freedom than did the full meshes, which made the models insensitive to the elastic properties of the overburden, when assumed constant per layer, as well as when a multiple iteration scheme was used, and reduced post-failure properties were assigned to the failed materials. Again, the models were

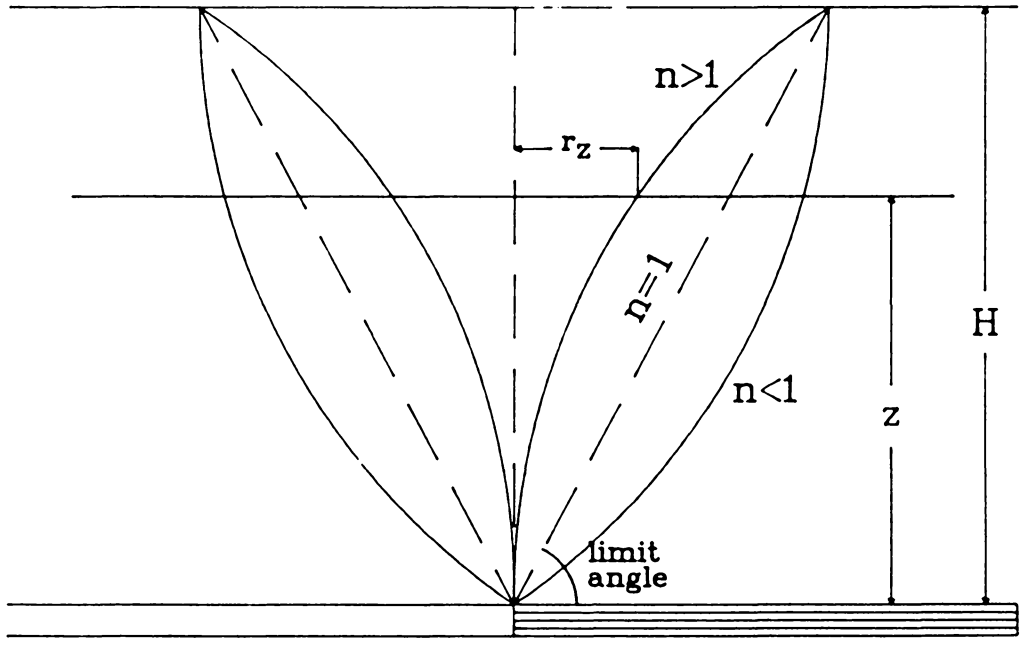

Figure 4.7 Possible Strata Movements along the Draw Line

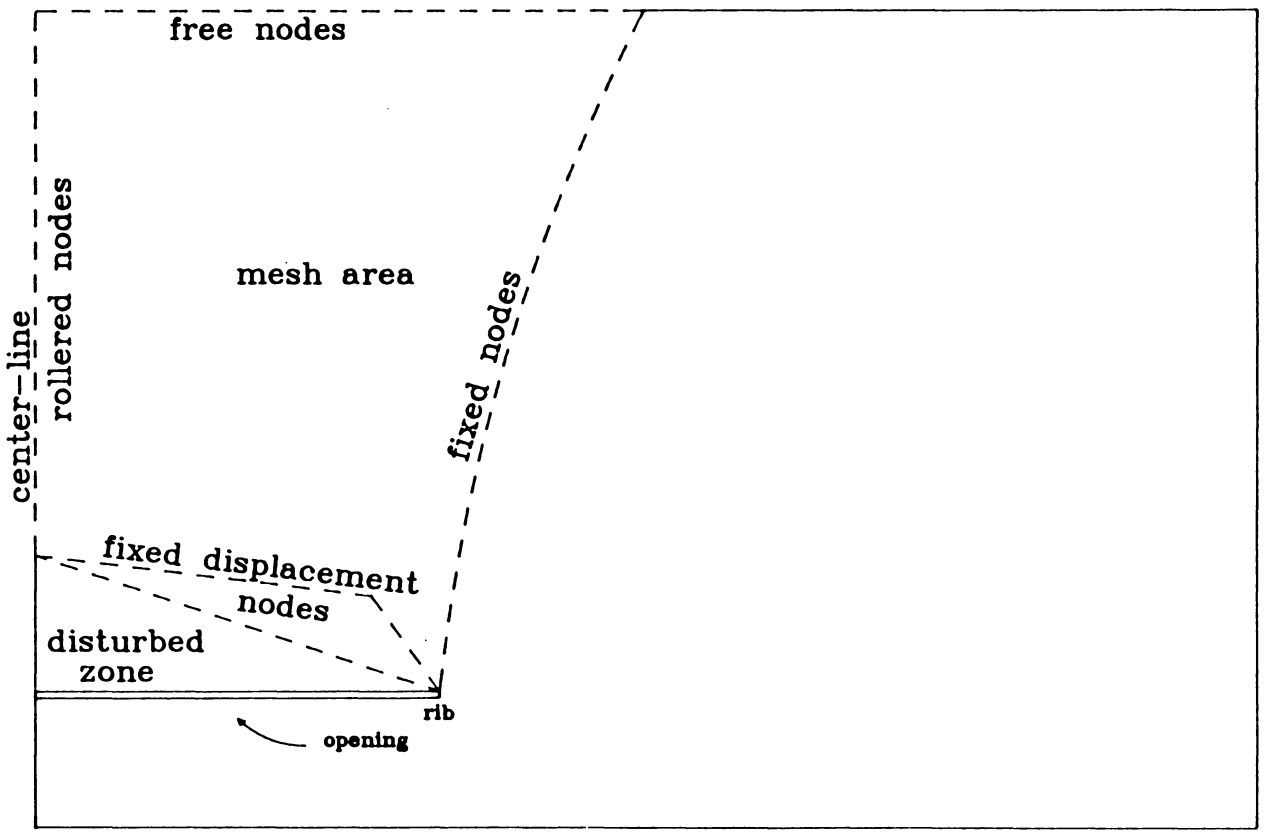

Figure 4.8 **Definition of the Restricted Mesh Used in the FEASD code**

sensitive to the magnitude of fixed displacement nodes inducing deformation. Further comparison between different model geometries is given below:

A model employing a **linear bounding** curve over the disturbed zone was compared to one using an approximated **elliptical bounding** curve. Fixed displacements applied to the disturbed zone nodes were proportional to the distance of the node to the seam level. Results indicated that the resulting shape of the surface subsidence curve was similar between the two models, and that the shape of the bounding curve was not very significant when the material properties were kept constant. When comparing the curves obtained from the unrestricted model to those obtained from the restricted model, the latter were contained within the influence area and exhibited steeper transition characteristics (i.e. around the inflection point) than did those obtained from the unrestricted model.

Conclusions: Although the restricted model concept was attempted under the speculation that it might reveal deformation patterns of the overburden, given some logical assumptions for strata behavior, it can be safely stipulated that a **restricted** mesh does not exhibit the flexibility to freely deform, since the linear system lacks the necessary degrees of freedom. The concept, however, was implemented in the full mesh design when different material properties were initially assigned around a potential failure line, delineated by the angle of draw or the angle of break as measured or calculated for a specific case study. Additionally, the presence of a disturbed zone in the immediate roof presented more disadvantages than benefits, since a roof convergence curve had to be assumed in an area where not even the maximum convergence value could be estimated.

4.6 Analysis Assuming Vertical Failure Zones

In this approach, the overburden was divided into distinct zones possessing different elastic properties. Properties of intact rock (or rock assumed to remain intact after failure was initiated) were assigned to the underburden elements and to the elements to the right of a line connecting the rib of the excavation to a specified point on the surface. This point was either defined as the draw point (DP), the break point (BP), or as a point with minimum surface effects (i.e. on the radius of influence). To the left of this line, and for varying widths, properties scaled down from 1/30 to 1/100 were assigned to the intact rock elements. These elements were assumed to represent the **shear zone** generated in the overburden because of the extraction. The rest of the elements directly above the opening assumed properties ranging between those assigned to the intact elements, and those assigned to the elements in the shear zone.

This distribution of elastic properties was based on the observations of mesh behavior during the preliminary analysis, and the application of the theoretically and empirically predicted stress zones to numerical procedures. The models were run for one iteration and, therefore, no failure criterion was utilized, since failure properties were preset.

Since failure was initiated using the **fixed** displacement formulation, absolute values for the elastic properties did not have a significant influence on the model. This model, however, appeared to be sensitive to the ratios of the elasticity moduli assigned to the different zones, which eliminated the need for accurate property determination for the different case studies.

4.6.1 Conclusions

It appears that the surface deformation characteristics produced by the above formulation match those predicted using empirical and analytical methods for similar panel layouts. Subsidence troughs were contained within the area of influence, and their shape was directly related to the width and position of the highly-stressed and, therefore, weak zones in the overburden. Horizontal strain profiles also followed the predicted patterns. The validation of the model, as well as the physical interpretation of the different zones established in this preliminary analysis, are contained in Chapter 6.

Chapter 5

Description of Field Data

The field data utilized in the study of strata deformation mechanisms and the validation of the numerical model can be divided into two categories. The first included data obtained from direct **underground** deformation measurements of the strata, during and after mining (Case Studies U1 and U2). The second set consisted of data related to the description of **surface** deformation characteristics, in terms of precise subsidence and strain measurements, for five case studies (S1 to S5). In addition, a number of empirical relationships developed from a comprehensive data bank, relating mining and surface deformation parameters, were utilized (Schilizzi, 1987).

The case studies used for this analysis are described in this chapter, while the corresponding evaluation of the strata deformation characteristics and the numerical analysis are presented in Chapter 6.

5.1 Measurements of Overburden Movement

5.1.1 Determination of Caving Height (Case Study U1)

The first case study (U1) relates to a longwall mine located in Wise County, Virginia. The layout of the mine and a detailed lithological column of the overburden layers are shown in Figure 5.1. Panel width was about 600 feet, with a total advance of approximately 2800 feet at an average depth of 800 feet (for the center panel). Average extraction height was approximately 52 inches. Overburden characterization properties, such as RQD, were determined by logging the cores obtained from boreholes drilled prior to mining.

For post-mining caving measurements, a surface borehole was drilled at the middle of the gob area (Point A, Figure 5.1), and the strata was logged using a borehole camera. The borehole was checked along its length for signs of bed separation, initiation of fractures, and voids.

Figure 5.2 shows typical photographs (reproduced from the video images obtained with the borehole camera) of strata layers and the observed conditions. Further drilling of the borehole was stopped when a large void area was identified by the drill operators, whereupon it was assumed that the uppermost major bed separation between the main and the immediate roof strata was reached. Thus, the height of the disturbed zone was estimated to extend to about 105 feet above the seam. Logging stopped before the bottom of the borehole had been reached, when the camera malfunctioned due to the presence of water. The points along the borehole, where evidence of strata disintegration was observed, were marked and subsequently compared to the lithologic column. The geomechanical properties of most of the overburden formations were determined

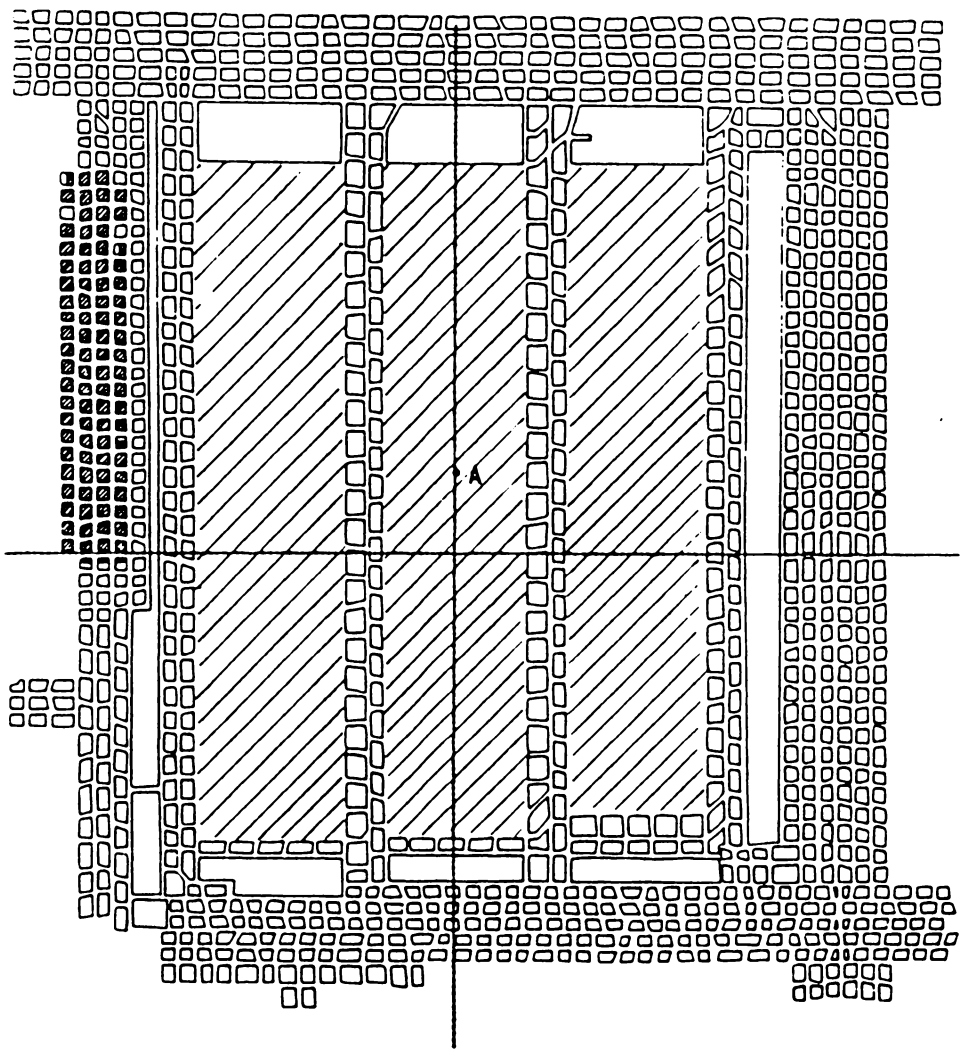

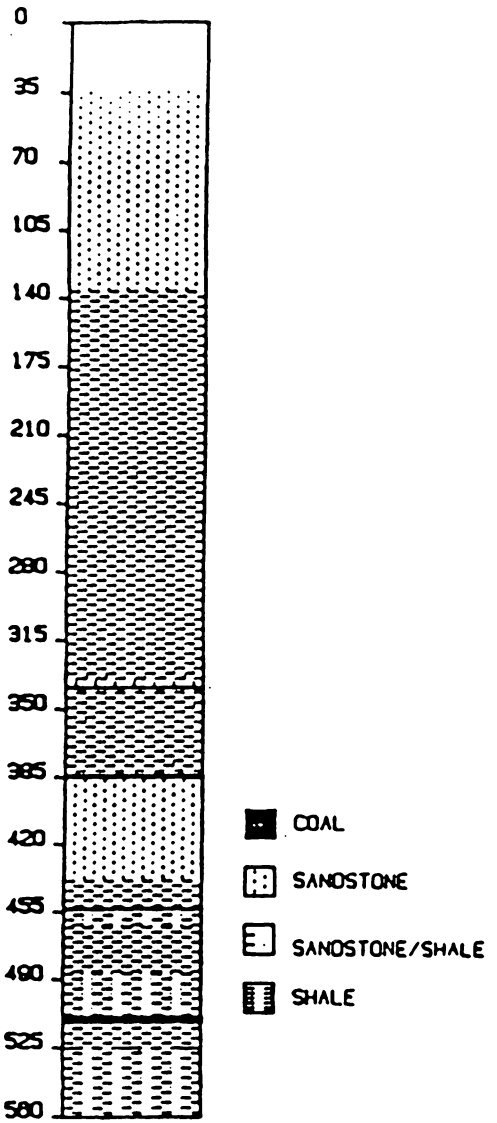

Figure 5.1 (a) Layout of the Longwall Panel and Location of the Borehole for Case Study (U1); (b) Detailed Lithologic Column of the Overburden

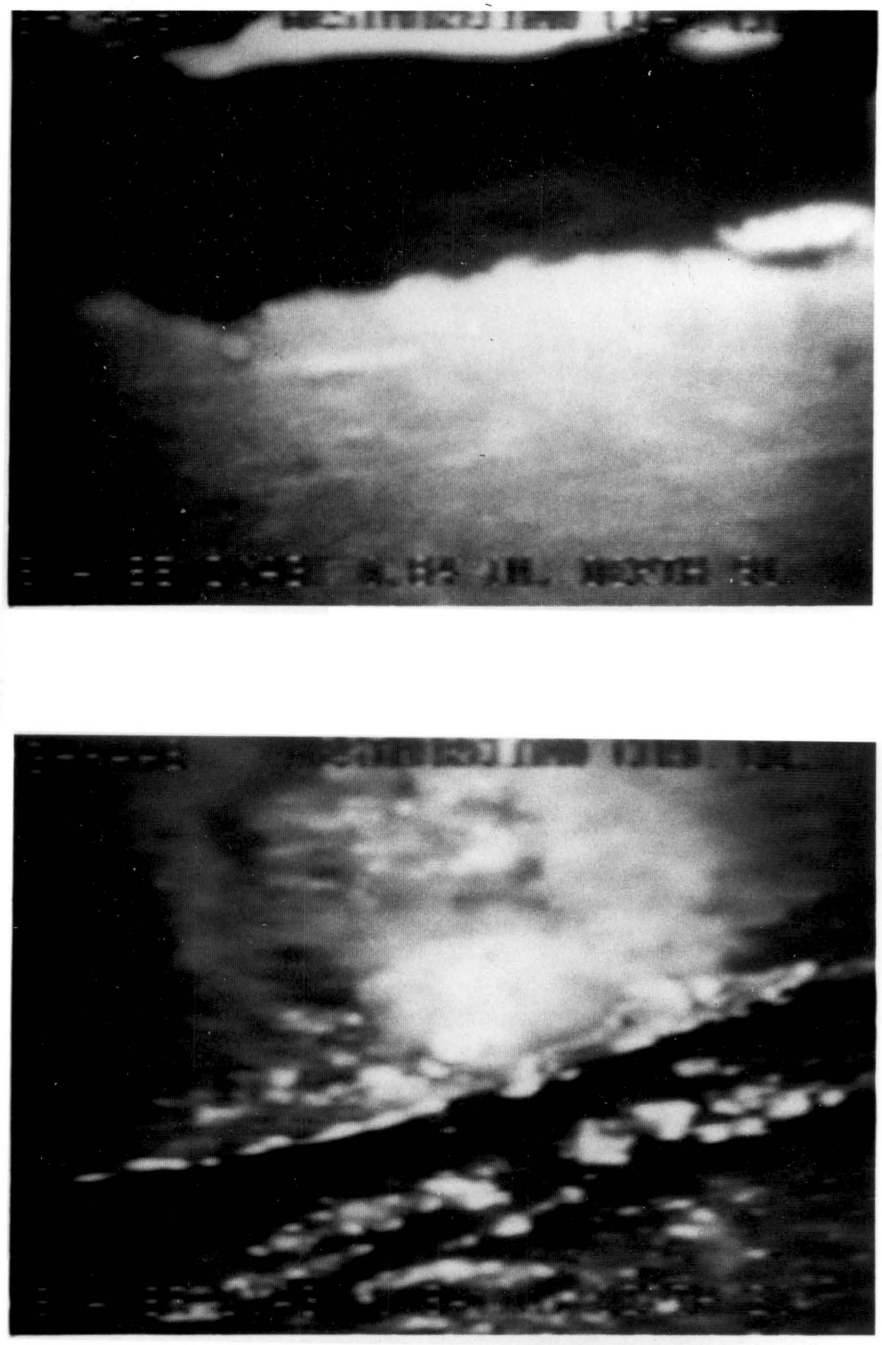

Figure 5.2 **Photographs of Bed Separation Detected by Borehole Camera**

through laboratory testing. The Young's modulus was obtained from samples tested under uniaxial compression, while the tensile strength was determined from Brazil Disk tests on different samples. The results are presented in Table 5.1.

It should be noted that the elastic modulus was calculated as the slope of a linear segment in the middle of every stress-strain curve, although results varied when a different linear segment was assumed for a particular curve. In any case, even the values calculated for different formations did not deviate more than 50% from the average value for all samples. Additionally, the results from the compressive and tensile strength tests indicated that the different overburden layers, with the exception of any thin coal seams, had similar properties. This important observation allowed considerable simplification to the input required by the numerical analysis procedure, as will be shown in subsequent sections.

5.1.2 Determination of Layer Separation and Recontact (Case Study U2)

This case study (U2) is associated with a longwall panel located in Alabama, where an extensive monitoring program had been conducted in order to determine the height of **detached** blocks in the main roof (Matthews, 1986). The longwall panel was 600 feet wide and approximately 2200 feet long, with an extraction height of 4.5 feet at an average depth of 550 feet. Four boreholes were drilled from the surface ahead of the operating longwall face, as shown in Figure 5.3. As the face approached the location of the boreholes, each hole was sequentially logged with a caliper instrument until the face had moved past their respective locations. The study showed that the initial break over the face extended to a distance of between 22 and 27 feet above the coal seam (Matthews, 1986). The raw data for this study were subsequently processed in order to analyze roof behavior patterns with respect to bed separation and recontact.

Table 5.1 Overburden Strata Properties for Case Study U1

Compressive Strength [psi]	Young's Modulus [psi]	Sample Rock Type
16098	1.90E+06	sandstone
13022	1.88E+06	sandstone
16039	2.26E+06	sandstone
12538	1.44E+06	sandstone
18457	2.49E+06	sandy shale
19370	2.28E+05	sandy shale
16974	2.28E+06	shaly sand.
16139	2.38E+06	sandstone
16676	2.36E+06	sandstone
16438	2.47E+06	sandy shale
22319	2.92E+06	sandy shale
21231	2.17E+06	sandstone
18903	2.42E+06	sandstone
21268	2.51E+06	sandstone
21522	2.43E+06	shaly sand.
23807	4.30E+06	shale
18439	2.53E+06	shale
25887	3.11E+06	shale
25128	3.00E+06	shaly sand.
20255	2.40E+06	sandstone
19025	2.48E+06	average

Tensile Strength [psi]	Sample Rock Type
1058	sandstone
1094	sandstone
1294	sandstone
1303	sandstone
1041	shaly sand.
1142	sandstone
1049	shaly sand.
1192	sandstone
1632	sandy shale
2233	sandy shale
1921	sandstone
1975	sandstone
1545	shale
1439	sandstone
1598	sandstone
1653	shaly sand.
1342	shale
1154	shale
1512	sandstone
1430	average

Average Values per Formation

17217	2.17E+07	sandstone
22711	9.95E+06	shale
20030	1.58E+07	interbedded

1412	sandstone
1347	shale
1522	interbedded

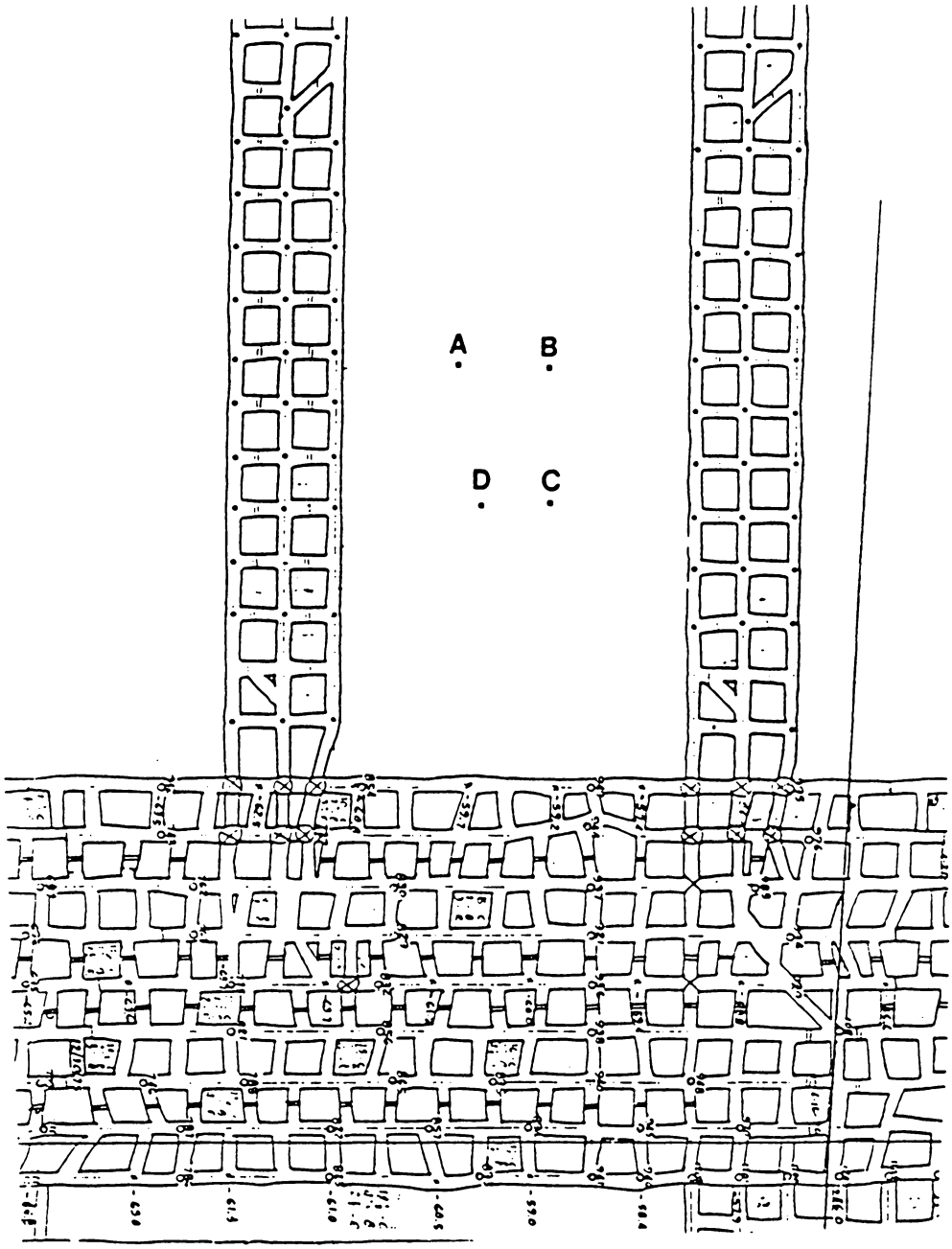

Figure 5.3 **Mine Layout and Location of Boreholes for Case Study U2**

5.2 Surface Deformation Data Bank

An extensive data bank has been established by the Department of Mining Engineering at VPI&SU, and is comprised of longwall, as well as room-and-pillar, case studies. Mining parameters include mining height (m), depth (h), panel width (W) and overburden lithology (expressed in the analysis as the percent hardrock[5]). Surface deformation parameters include the angle of draw (γ), maximum subsidence (S_{max}) and maximum strain (E_{max}), and deformation profiles.

The regression equations developed based upon the above data, relating subsidence to mining parameters, have been used to develop a number of surface deformation prediction methods (VPI&SU, 1987). In all of these methods, the value of maximum subsidence for critical and supercritical panels must be known, and it has been determined as a function of the overburden geology, as given in the following equation and in Figure 5.4.

$$\frac{S_{max}}{m} = 0.12 + 0.66\ e^{-0.00034\ HR^2} \qquad [5.1]$$

where

S_{max} = the maximum subsidence;

m = the extraction thickness;

HR = the percent hardrock in the overburden.

Additionally, the method predicts the location of the maximum subsidence point as:

---

[5] Percent hardrock (%HR) is percent competent strata in the overburden, such as limestones, sandstones, etc., having a thickness in excess of two feet.

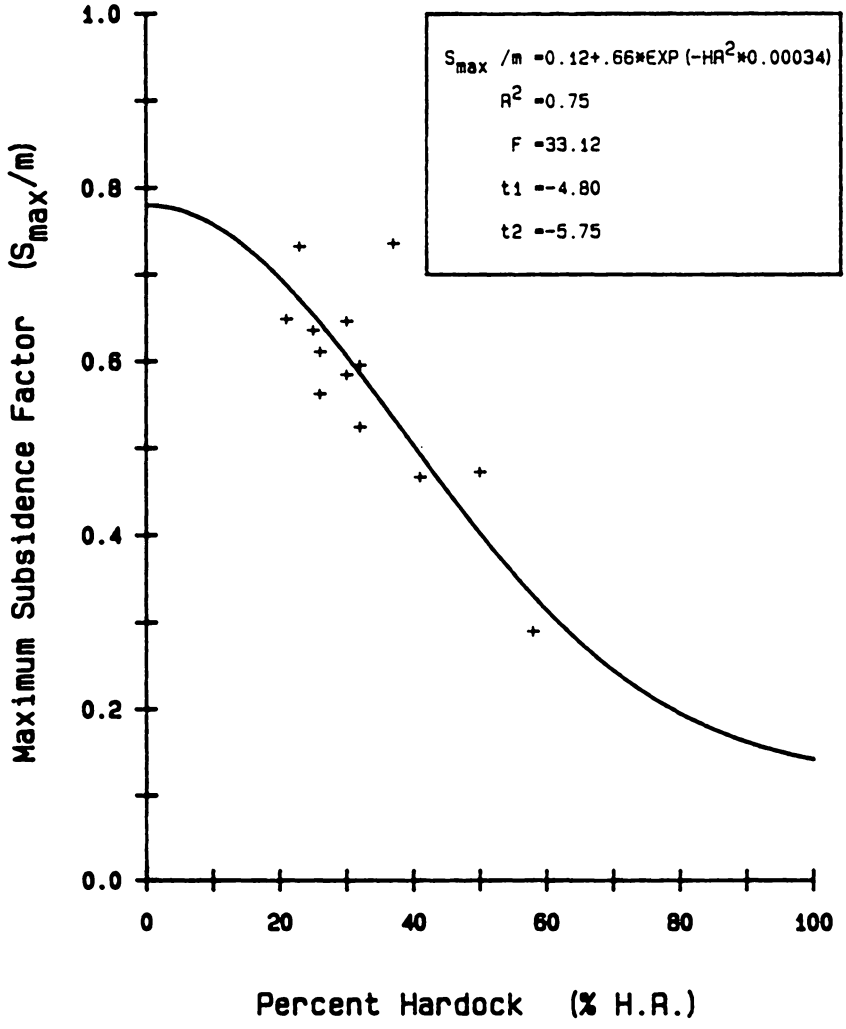

Figure 5.4 Influence of Hardrock in the Overburden on the Maximum Subsidence Factor (Critical and Supercritical Panels, Longwall Case Studies) [after Schilizzi, 1987]

- 0.5 W, i.e. the panel center for critical and subcritical panels (where W is the panel width); and
- 0.6 h for supercritical panels (where h is the overburden depth), i.e. at the point where the profile begins to **stretch** without any additional increase in subsidence value.

Using the curves shown in Figure 5.5, the maximum subsidence factor (a) for longwall panels can be predicted as a function of the overburden lithology (percent hardrock) and panel geometry. Additionally, Figure 5.6 and the following equation show the effect of the width-to-depth ratio (W/h) on the location of the inflection point (d/h)[6] for the longwall and room-and-pillar case studies:

$$d/h = 0.36 - \frac{0.14}{(W/h)} \qquad [5.2]$$

It should be noted that, for W/h ratios greater than 1.2, the panel was assumed to have reached supercritical conditions, and, therefore, the location of the inflection point was assumed to remain constant.

Additionally, accurate measurements of vertical and horizontal displacements were available for several case studies, so that complete surface deformation profiles were obtained.

Although the application of vertical zoning of properties was selected as the best approach to modeling surface deformations (Chapter 4), it was necessary for the model to

---

[6] d is the distance of the inflection point from the rib and h is the depth of the excavation.

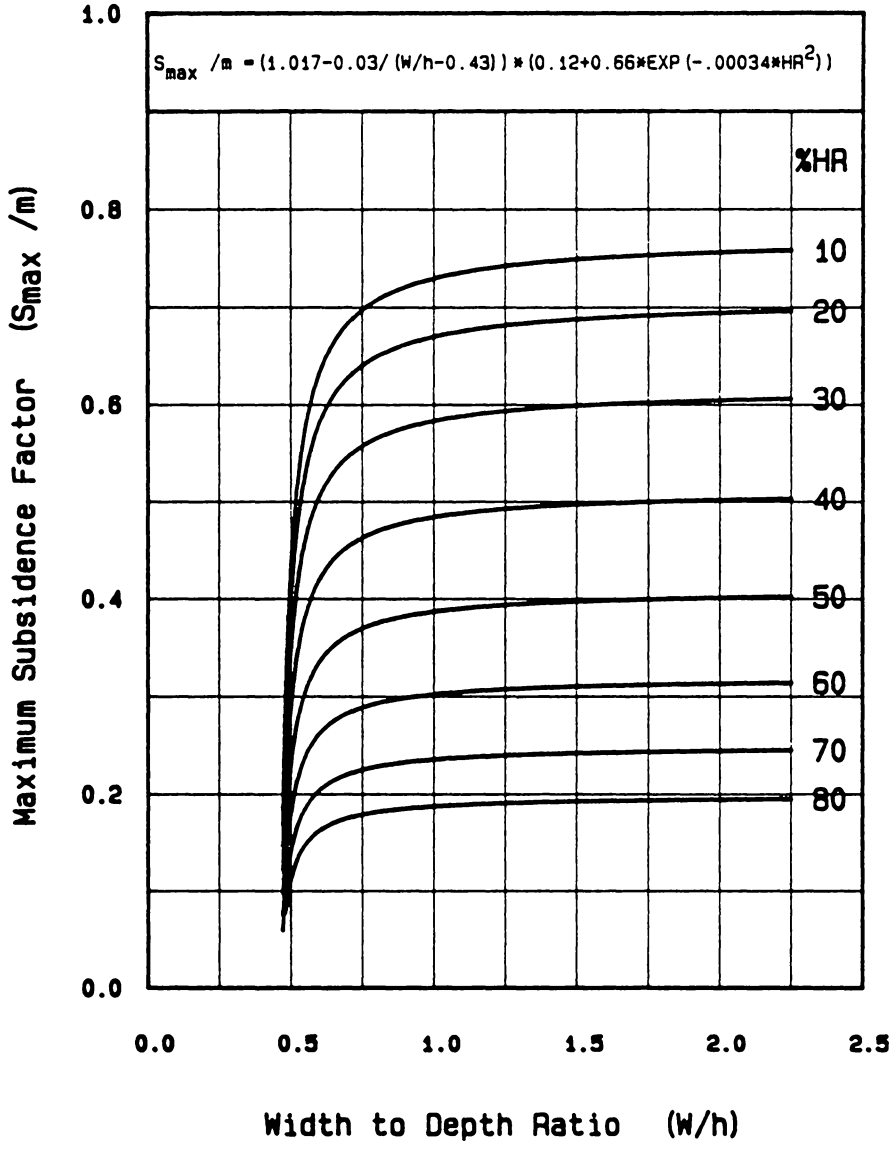

Figure 5.5 Prediction of the Maximum Subsidence Factor (Longwall Case Studies) [after Schilizzi, 1987]

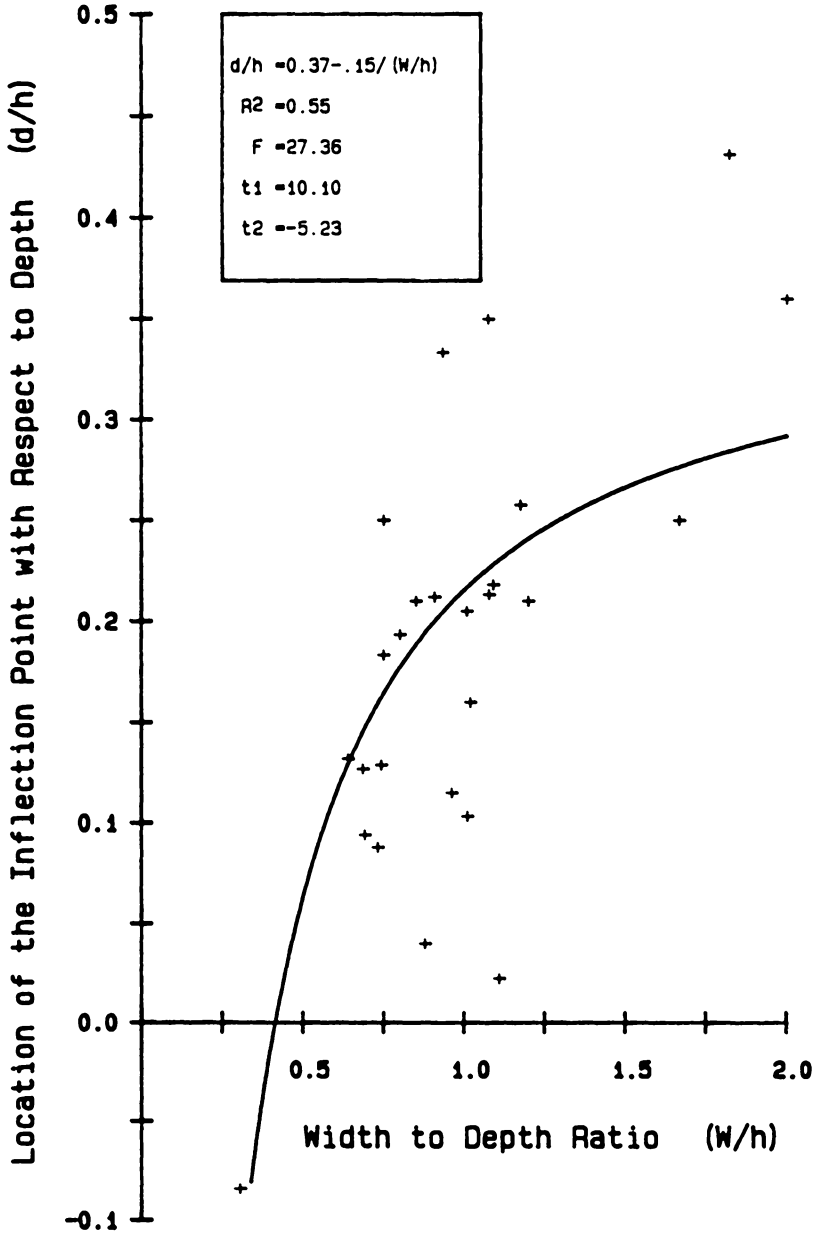

Figure 5.6 Effect of Width-to-Depth Ratio on the Location of the Inflection Point (Longwall Case Studies) [after Schilizzi, 1987]

produce a satisfactory match between measured and calculated deformation values, before overburden strata deformation mechanisms could be examined. The validation of the numerical model, with respect to prediction of surface deformation patterns, (i.e. subsidence and horizontal strains), is given in Chapter 6. A numerical procedure, incorporating some deformation parameters determined by the empirical prediction methods, is also proposed.

5.2.1 Surface Deformation Case Studies

Five case studies were selected in order to determine the potential of the numerical model developed, with respect to modeling surface deformations. Although the model was primarily designed to simulate longwall mining conditions, it also had considerable application to high extraction room-and-pillar mines, especially in areas where no remnant pillars were present and extraction was uniform.

The surface deformation profiles of these case studies were analyzed, and the subsidence parameters were calculated for each profile. Since, in some cases, these values deviated from the average parameters for the case study and/or the region, the site-specific values were utilized in order to obtain a better representation of the specific surface deformation profile. Figure 5.7 shows the longwall panel pertaining to Case Study S1, and includes the monument layout that was utilized during surface deformation monitoring (Schilizzi, 1987). Case Study S2 (Figure 5.1) represents the information on surface deformation for case study U1, where measurements to determine the height of the disturbed zone were also made. The room-and-pillar panel for Case Study S3 is shown in Figure 5.8, while Figure 5.9 shows a typical geological column for the area. The panel was modeled on a transverse cross-section (line A-A), which coincided with the transverse monitoring line used for surveying. Figure 5.10 shows the room-and-pillar panel

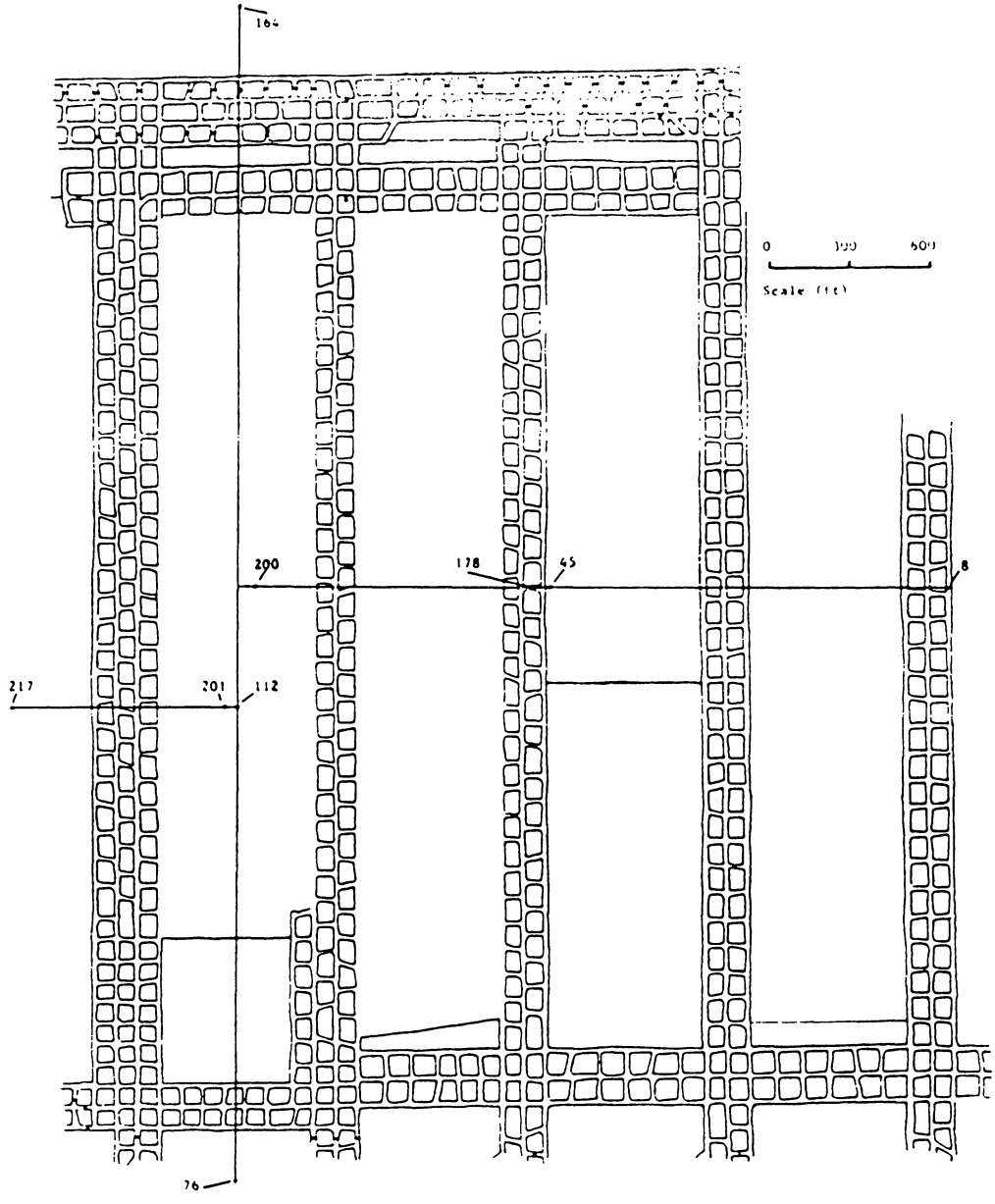

Figure 5.7 **Mine Plan and Monument Layout for Case Study S1**

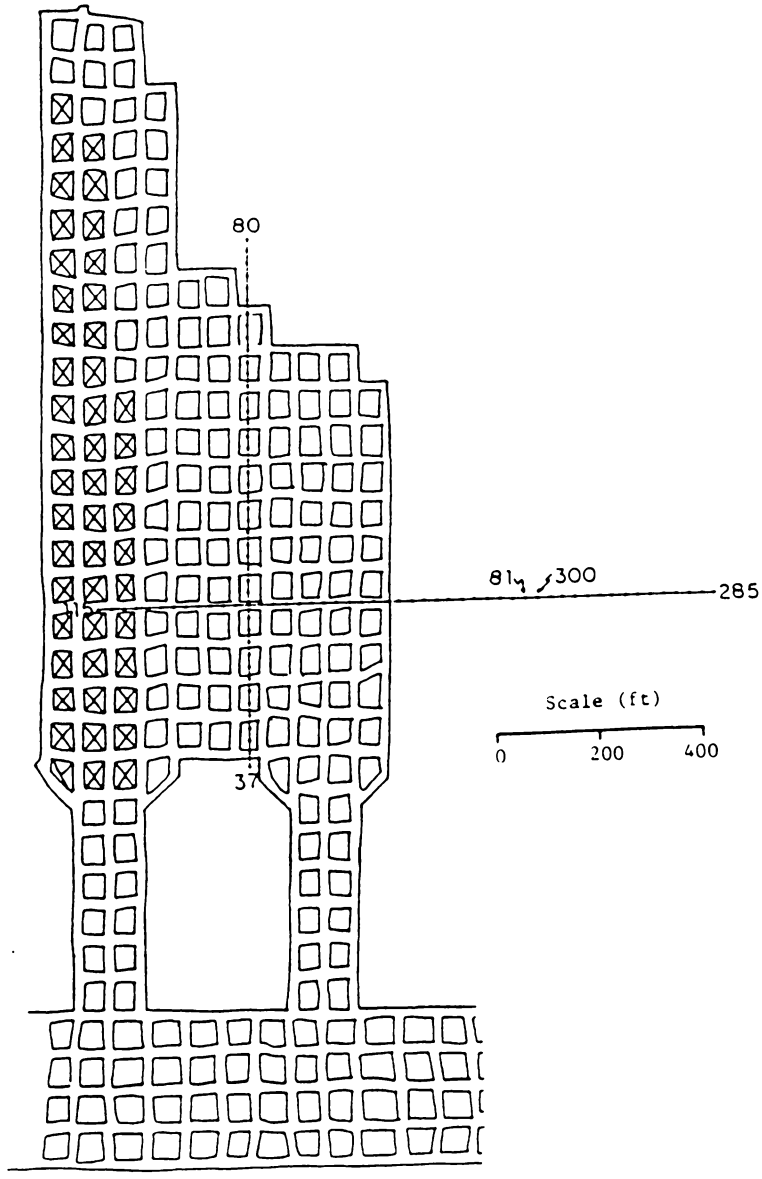

Figure 5.8 **Mine Plan and Monument Layout for Case Study S3**

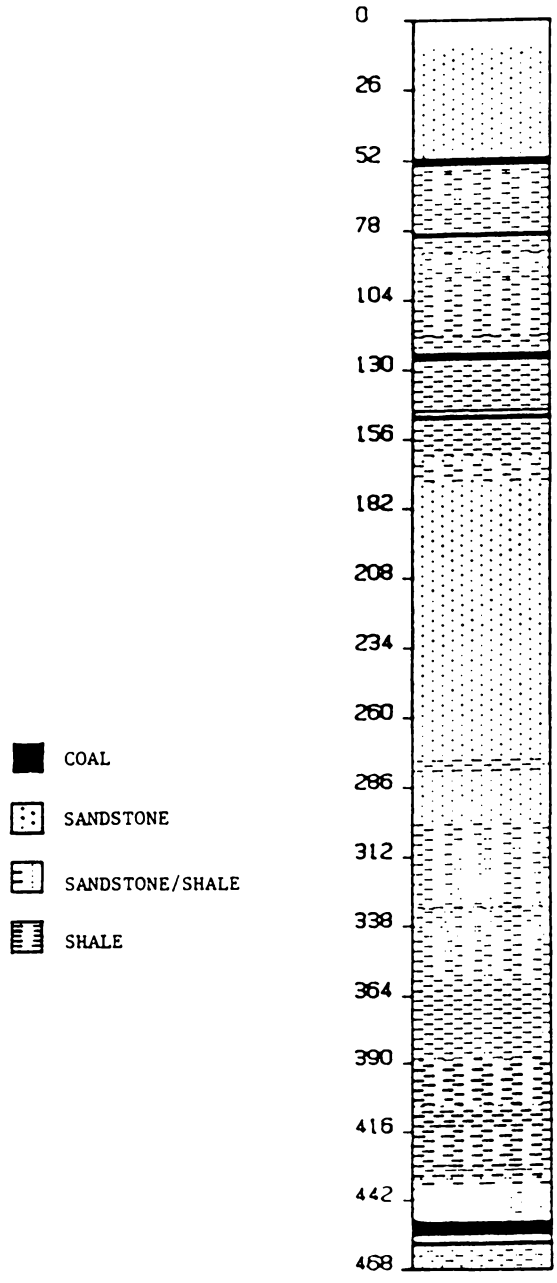

Figure 5.9 **Detailed Lithologic Column of the Overburden for Case Study S3**

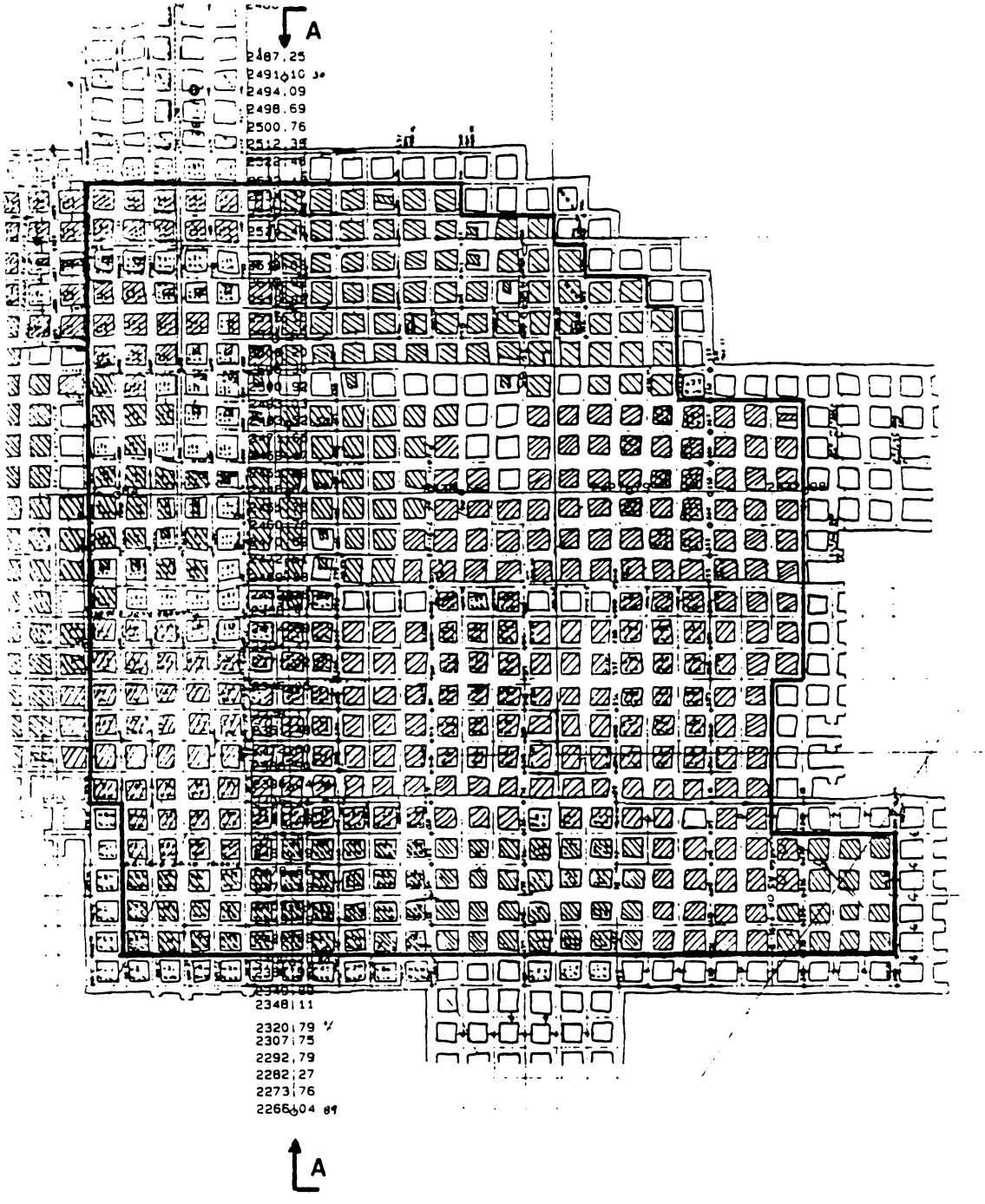

Figure 5.10 **Mine Plan for Case Study S4**

for Case Study S4. The panel was modeled along a transverse cross-section (line A-A), which coincided with the transverse monitoring line used for surveying.

Finally, Figure 5.11 shows the longwall panel for Case Study S5. Surveying data were also available for a transverse monitoring line located in the middle section of the panel.

Table 5.2 summarizes the mining and subsidence parameters for each case study. The location of the inflection point, the draw point and the break point given for each case study were extracted from the measured subsidence profiles.

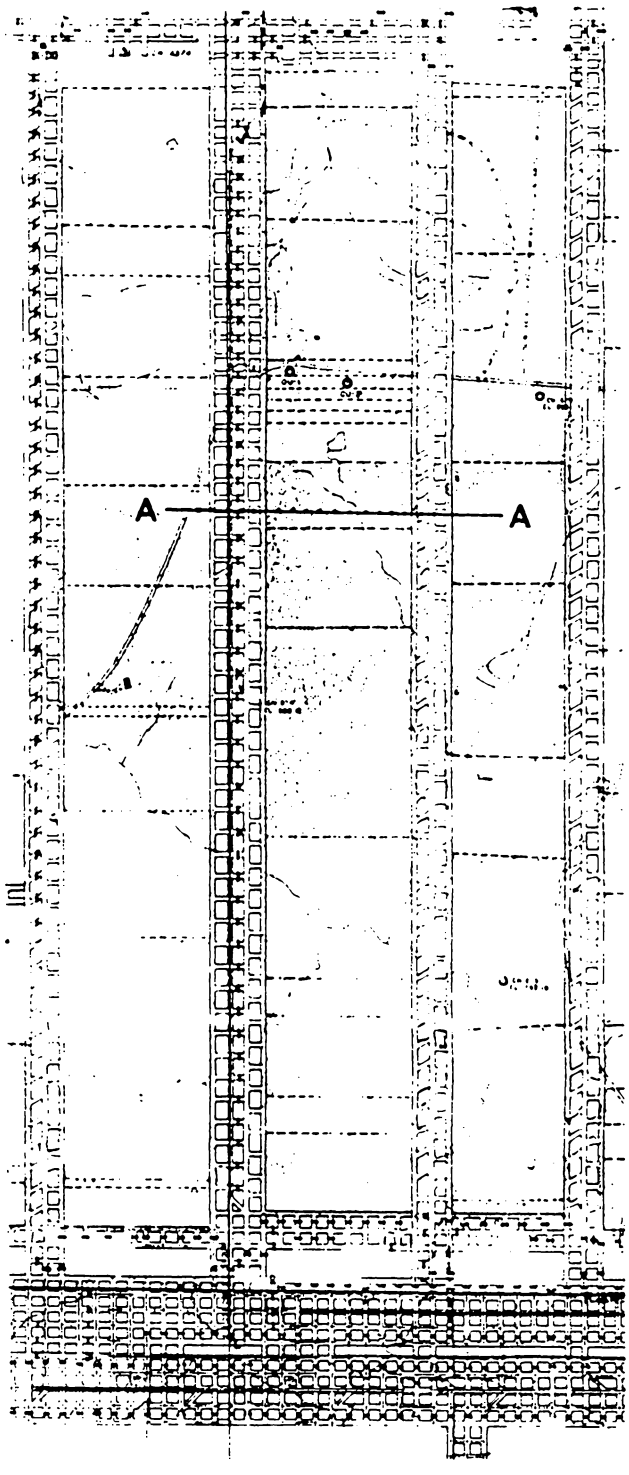

Figure 5.11 **Mine Plan for Case Study S5**

Table 5.2 Mining Parameters of Selected Case Studies

Case Study	Mining System	Location	Depth (h) [feet]	Width (W) [feet]	Width to depth (W/h) ratio	Percent Hardrock (%HR)
S1	Longwall	Virginia	700	600	1.17	46
S2	Longwall	Virginia	625	580	0.93	50
S3	Room & Pillar	Virginia	600	600	1.00	32
S4	Room & Pillar	Virginia	480	900	1.88	50
S5	Longwall	Ohio	360	700	1.94	34

Case Study	Seam height (m) [feet]	Maximum Subsidence (S_{max}) [feet]	Draw Point [1] (DP) [feet]	Draw Angle (γ) [degrees]	Break Point [1] (BP) [feet]	Break Angle (δ) [degrees]	Inflection Point [1] (IP) [feet]
S1	7.0	3.20	200	16	100	8	-150
S2	5.5	2.40	200	14	50	4	-150
S3	4.5	2.05	200	18	-25	-2	-150
S4	3.4	1.45	200	22	-50	-6	-140
S5	6.4	3.80	300	39	-50	-8	-100

[1] Draw, Break and Inflection Point distances are given from the rib of excavation. Negative distances indicate displacement towards the center line of the panel.

Chapter 6

Analysis of Strata Deformation Mechanisms

The study of overburden deformation mechanisms has not been the subject of a single methodology. Empirical, analytical and numerical procedures have been proposed by different researchers in an effort to explain the observed phenomena, and to develop a predictive tool for the field engineer. An attempt was made in this study to validate different methods for the study of overburden movements and their surface manifestations. The necessary input for the application of the various methods, however, is not always available for every case study. Thus, a collection of case studies (presented in Chapter 5) was analyzed, and the results were compared.

6.1 Analytical and Empirical Approach

In this approach, both analytical methods (i.e. beam and plate theories) and rock classification methods, utilizing some roof strength evaluation parameters to determine whether part of the roof is liable to fail under certain conditions, were used. Since it was necessary to evaluate the sequence of failure in the immediate roof and to compare it to the sequence given by the empirical methods, a computer program was developed in BASIC (run under MS-DOS), in order to facilitate calculations. In an effort to evaluate

the caving height, the roof was allowed to fail, and the loose material to fill the void until bulking arrested the caving process. The value for the initial bulking factor was assumed, but the program allowed for its reduction due to compaction of the material during panel advance. Figure 6.1 shows a set of typical curves used for reducing the bulking factor of the lower layers, due to compaction, which in turn resulted from failure of the upper roof layers. The bulking factor reduction was calculated for each failed layer and was subsequently subtracted from the initial bulking factor of the layer. Bulking factors were recalculated as the caving height increased and more material failed.

The **first weighting** was estimated using the different empirical methods, i.e. equations [2.9], [2.10] and [2.12], and the beam/plate theory approach. More specifically, failure was assumed when the maximum normal stresses given by the plate theory equations exceeded the strength of the material, as the exposed roof area was increased in a stepwise fashion. Figure 6.2 shows a typical sequence of progressive roof failure generated by the aforementioned procedure. Immediate roof quality was also evaluated according to the classification system presented previously.

A full description of the program and its features is given in Appendix A.

6.1.1 Analysis of Case Studies

In an effort to evaluate the sub-surface movements for Case Study U1, a set of predicted subsidence and strain curves was calculated using the Budryk-Knothe influence functions (Karmis and Jarosz, 1985). The measured profile at the surface was matched to that calculated by the influence functions, in order to find the case-specific empirical parameters. The overburden was then gradually reduced, and the corresponding surface deformation profiles calculated. Although the sub-surface movements calculated at a

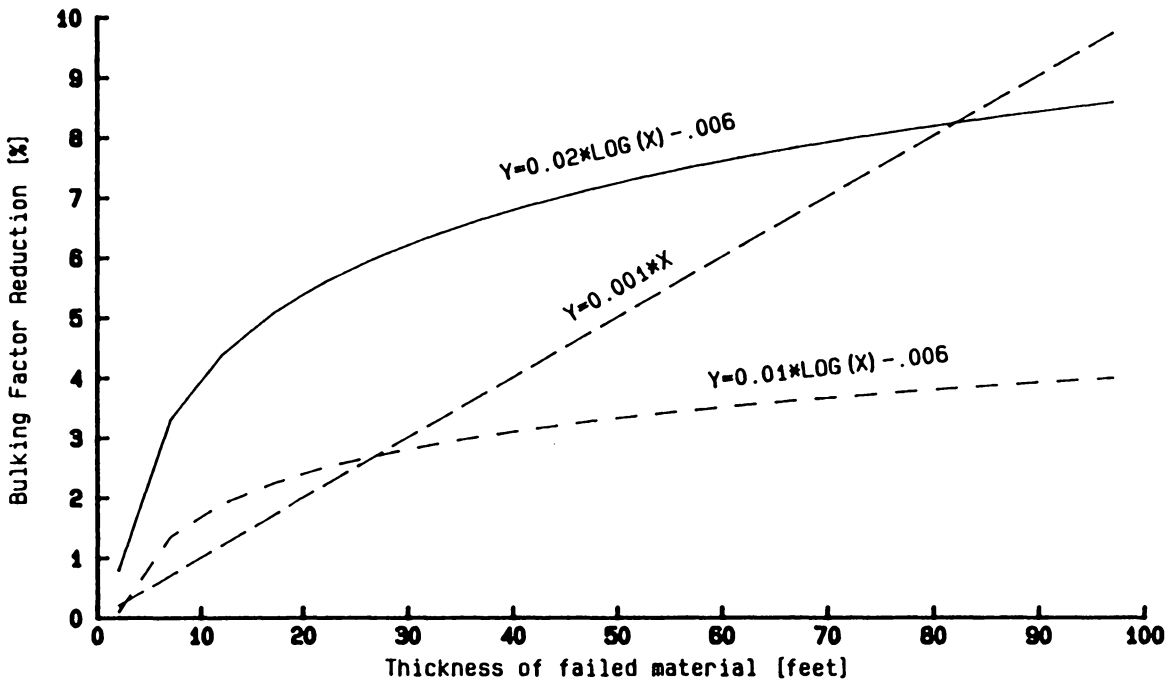

Figure 6.1 **Typical Curves used for Reducing the Bulking Factor of the Caved Material**

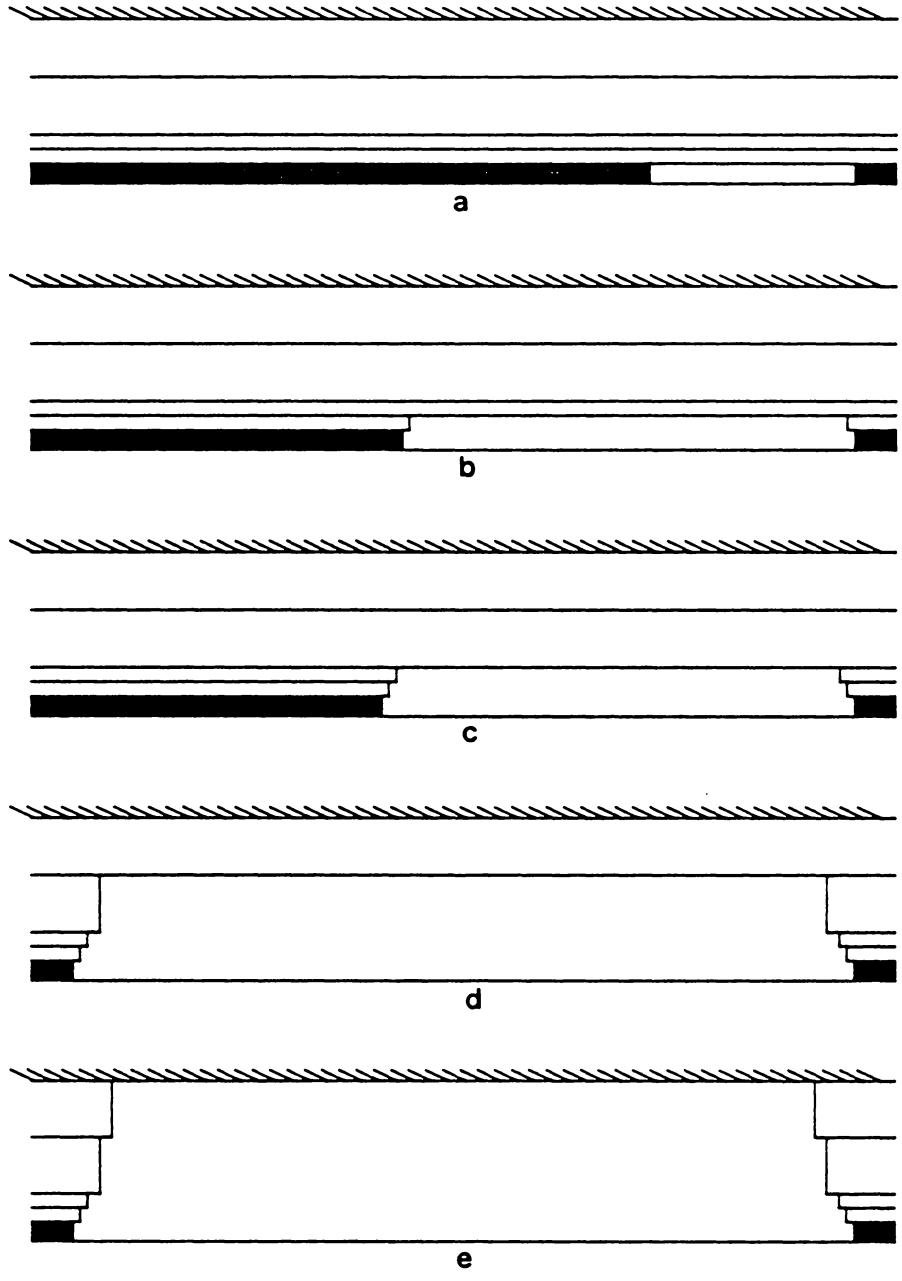

Figure 6.2 Progressive Roof Failure Calculated by the Beam/Plate Theory

given horizon treat that particular horizon as the surface, a comparative evaluation of sub-surface behavior was obtained. Figure 6.3 shows the subsidence and strain profiles obtained under the above assumption. The subsidence curves became supercritical as the width-to-depth ratio of the panel increased and the transition area on the curves was minimized. The shape of the curves indicated that, up to 200 feet from the top of the seam, there was an almost direct roof collapse. Subsequent profiles, however, exhibited a transition between the concave and convex areas, thus indicating that beam bending had taken effect.

Figure 6.4 shows the maximum tensile strain plotted as a function of distance from the top of the seam, under the above assumptions. A sharp increase in tensile strain can also be observed for distances of less than 200 feet, and particularly for distances of less than 100 feet. This value coincides with the estimated height of the **disturbed zone** for this case study, i.e. the height of the immediate and main roof. This, however, is different from the **caving height**, which is assumed to represent the height of the immediate roof, where complete collapse of the strata is expected.

The geomechanical properties obtained in the laboratory for the overburden layers for Case Study U1 were used without any reduction in the different empirical and analytical formulations. The roof classification system, however, required the use of stress reduction factors (K_1, K_2, K_3), which were assumed to be 0.6.

Table 6.1 describes the immediate roof parameters used in the analysis, and Table 6.2 presents the estimated first weighting distances calculated for Case Study U1. Furthermore, an **observed** value obtained from practical experience at the site is given.

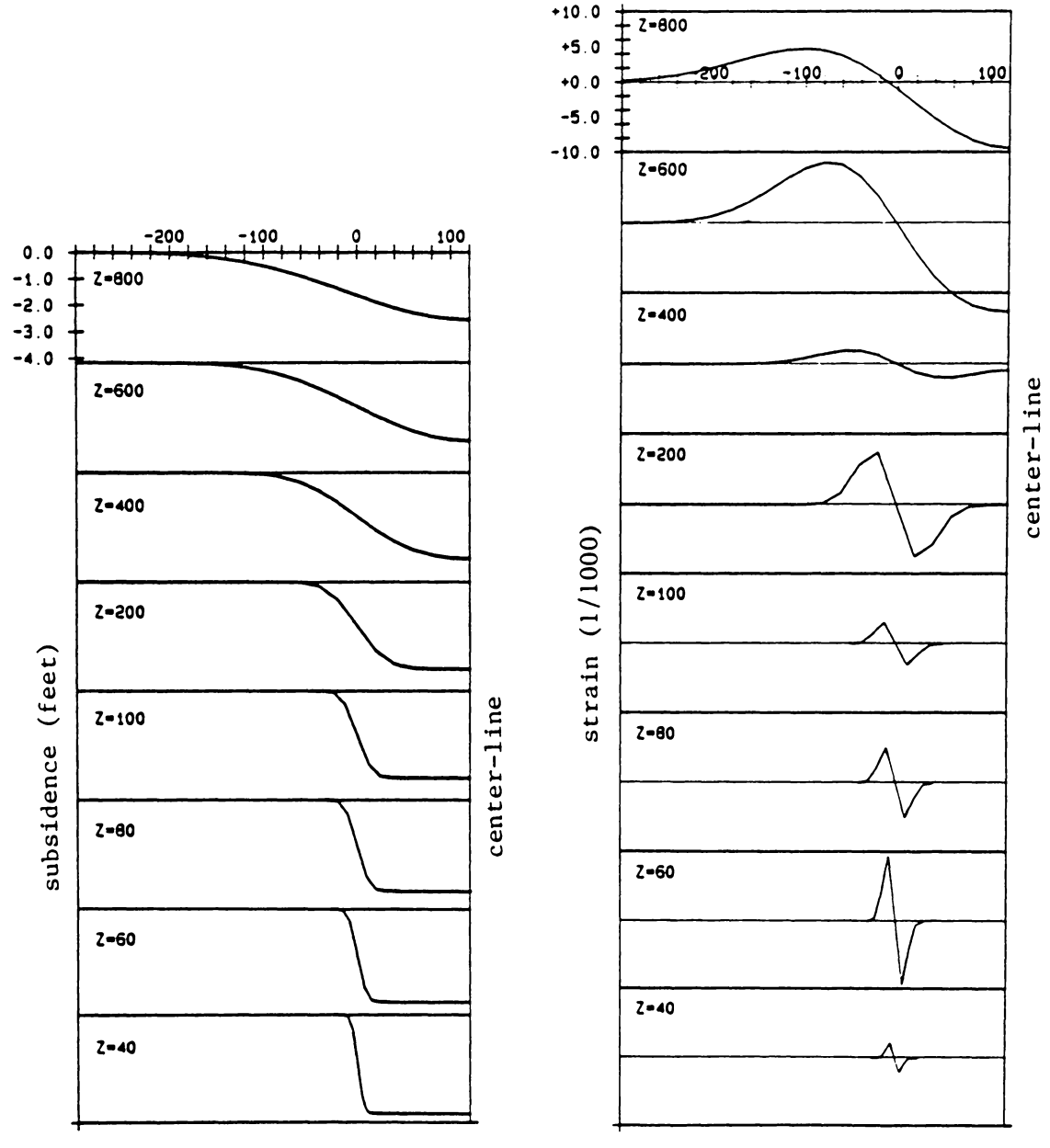

Figure 6.3 Model of Subsidence and Strain Development from Seam Level to the Surface, Using the Influence Function Method

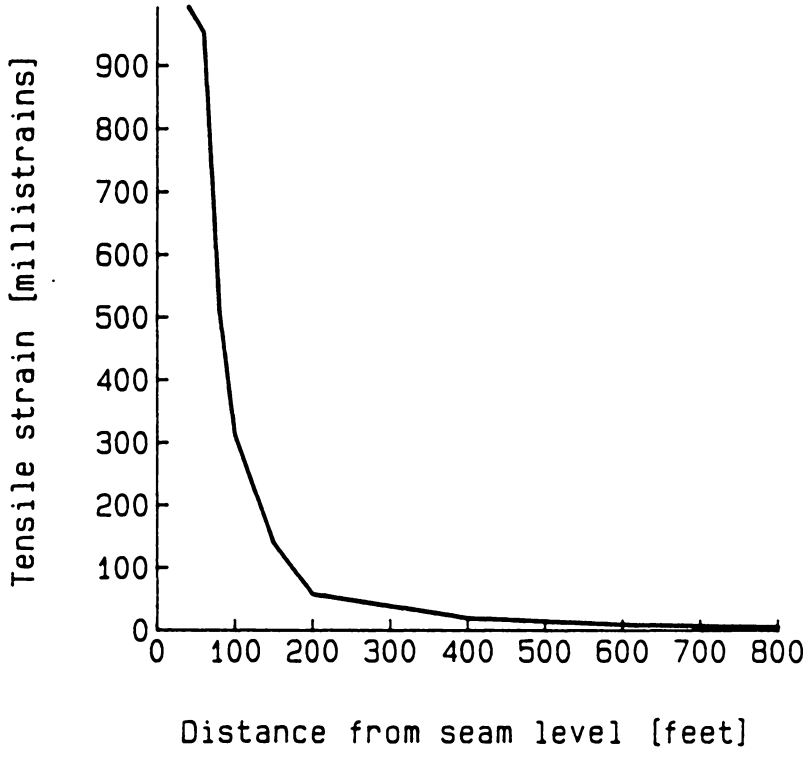

Figure 6.4 **Maximum Tensile Strain versus Distance from the Seam, Using the Influence Function Method**

Table 6.1a Immediate Roof Parameters for Case Study U1

Rock Type	Density [lbs/ft^3]	Thick-ness [feet]	Initial Bulking Factor	Compressive Strength [psi]	Tensile Strength [psi]	Young's Modulus [psi]	Strength Reduction Factor[1]
shaly sand.	150	3.0	1.15	18,000	2,000	$1.6\ 10^6$	0.22
sandstone	150	3.0	1.15	20,000	2,000	$1.5\ 10^6$	0.22
sandstone	150	24.0	1.15	20,000	2,000	$1.5\ 10^6$	0.22
shale	150	19.0	1.15	20,000	2,000	$1.7\ 10^6$	0.22
sandy shale	150	6.0	1.15	20,000	2,000	$1.7\ 10^6$	0.22
coal	90	1.0	1.15	2,000	200	$1.8\ 10^5$	0.22
sandy shale	150	15.0	1.15	20,000	2,000	$1.5\ 10^6$	0.22

[1]: for roof classification method

Table 6.1b Analytical Model Parameters for Case Study U1

Total Layers	7
Seam Thickness [feet]	4.2
Panel Width [feet]	600
Total Entry Width [feet]	40
Total Advance [feet]	500
Advance Increment [feet]	2

Table 6.2 First Weighting Calculations for Case Study U1
(Thickness of First Layer = 3 feet)

Method	Distance [feet]
Plate theory	106
Roof Classification	161
Equivalent Span Method (RQD = 60%[(2)])	133
Simple Tension Formula[3] (Bulking Factor = 1.25)	248
Simple Tension Formula[3] (Bulking Factor = 1.50)	176
Observed	150-200

[2]: estimated value from information on higher layers
[3]: equation [2.10]

The complete set of measurements of overburden movement during operation of the longwall in Case Study U2, along with the lithologic columns pertaining to the area, are presented in Figures 6.5 to 6.7. Every break in the strata continuity, however small, was logged, and is presented on these graphs. On many occasions, the gaps were detected temporarily and did not appear in subsequent logs, while in other instances gap width increased, followed by a downward movement of both upper and lower boundaries of the gap. The lithologic columns shown in each figure were obtained from three boreholes close to the monitored area, and the actual conditions prevailing at the site were assumed to be approximated by the available data. It is evident that bed separation occurred mostly at layer boundaries (i.e. points A, B in Figure 6.5), in the immediate roof, and in the main roof. Additionally, many of the resulting gaps were not detected by subsequent measurements, indicating that they closed due to either sagging or plastic deformation of the overlying layers.

The data were utilized to determine the size of the detached blocks in the immediate roof for support capacity evaluation and, thus, the caving height was evaluated as being between 27 and 33 feet (Matthews, 1986).

Table 6.3 presents the immediate roof parameters used in the analysis, and Table 6.4 presents the estimated first weighting distances calculated for Case Study U2. The caving height was also estimated by applying the beam/plate theory, utilizing different initial bulking factors (Table 6.5).

6.1.2 Utilization of Empirical Results in Model Formulation

Both empirical and analytical evaluation of strata deformation parameters are possible using a variety of approaches. The results, however, pertain to the specific case study

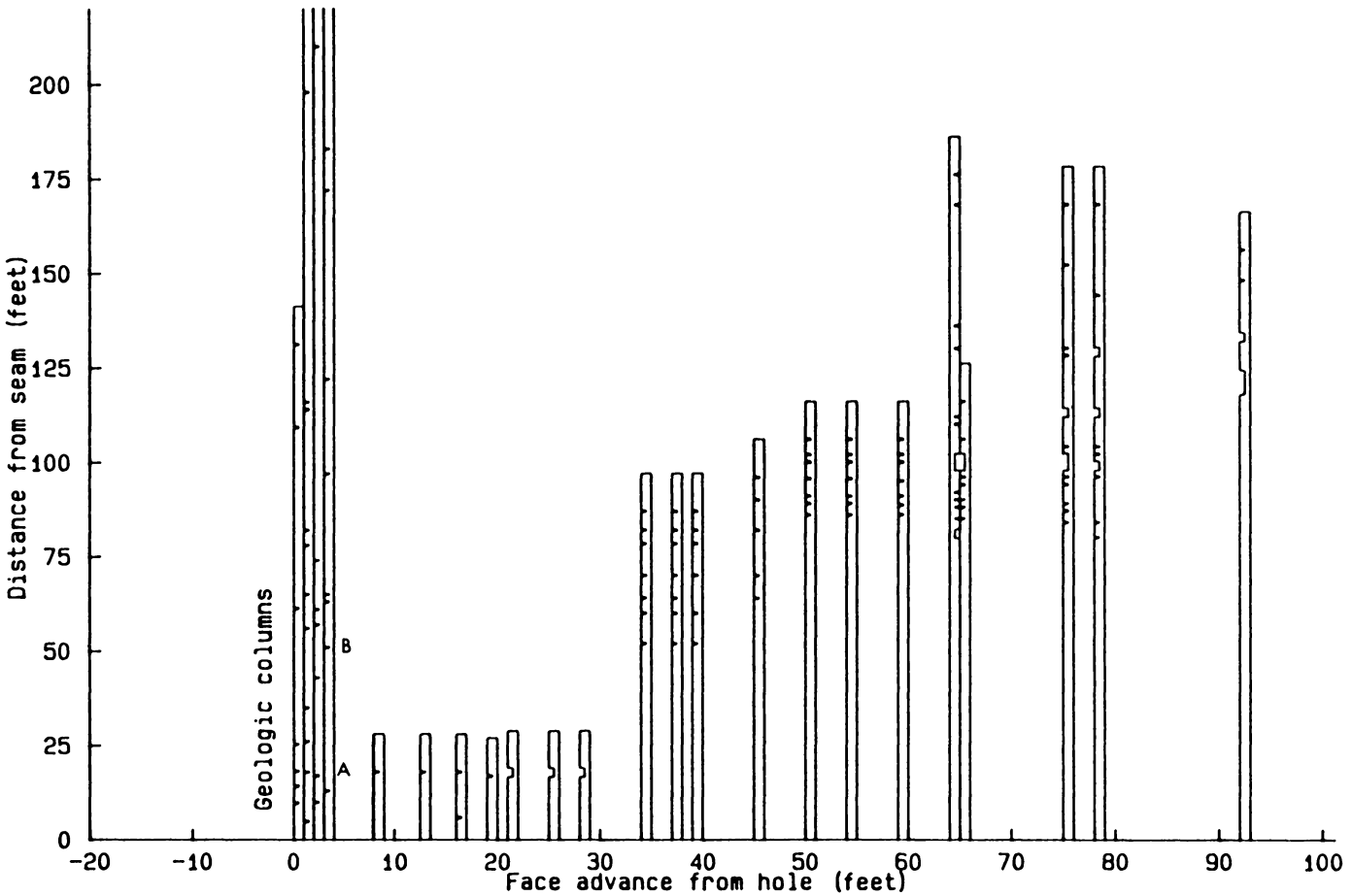

Figure 6.5 **Measurements of Overburden Movement (Borehole A, Case Study U2)**

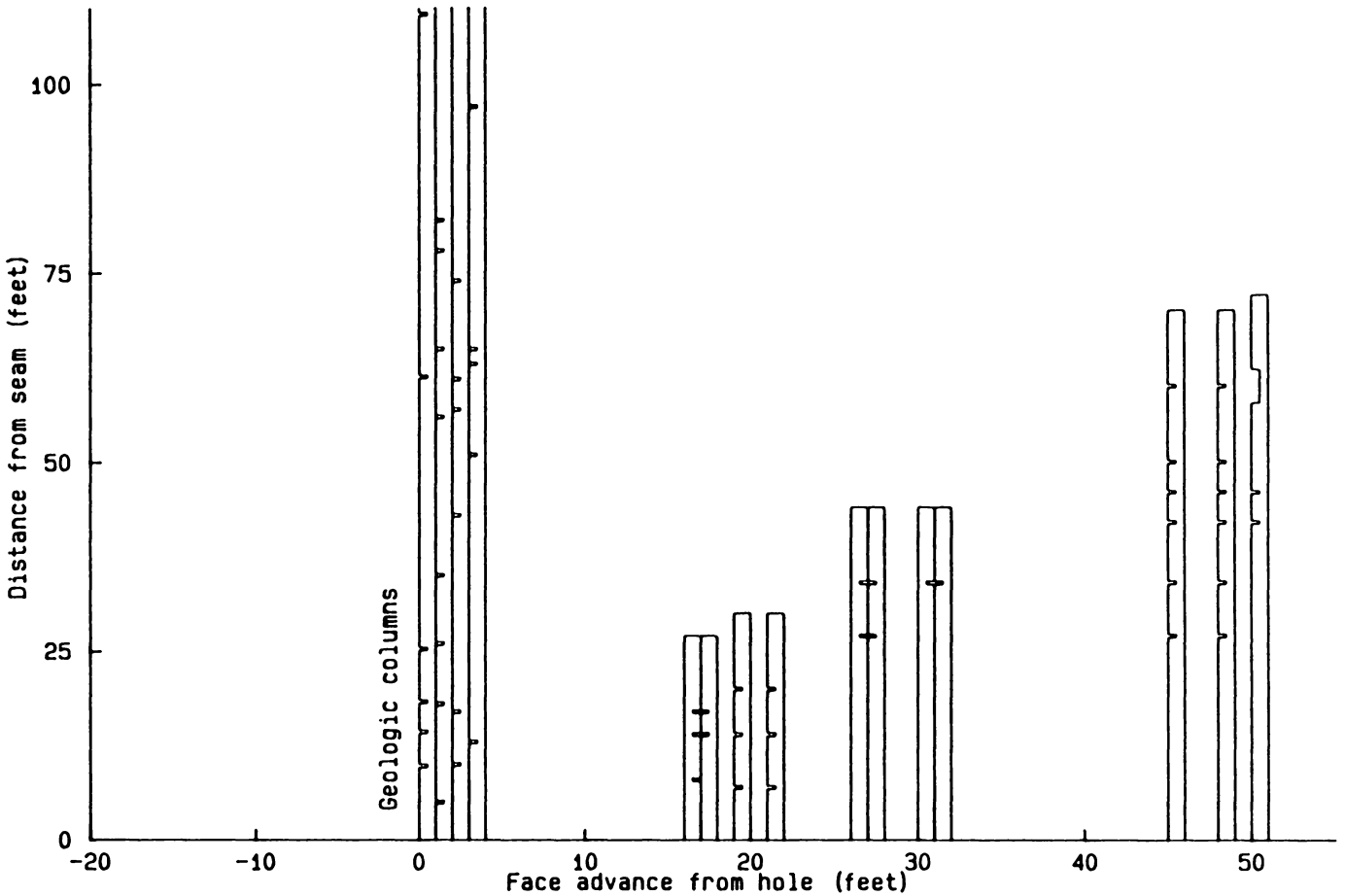

Figure 6.6 **Measurements of Overburden Movement (Borehole B, Case Study U2)**

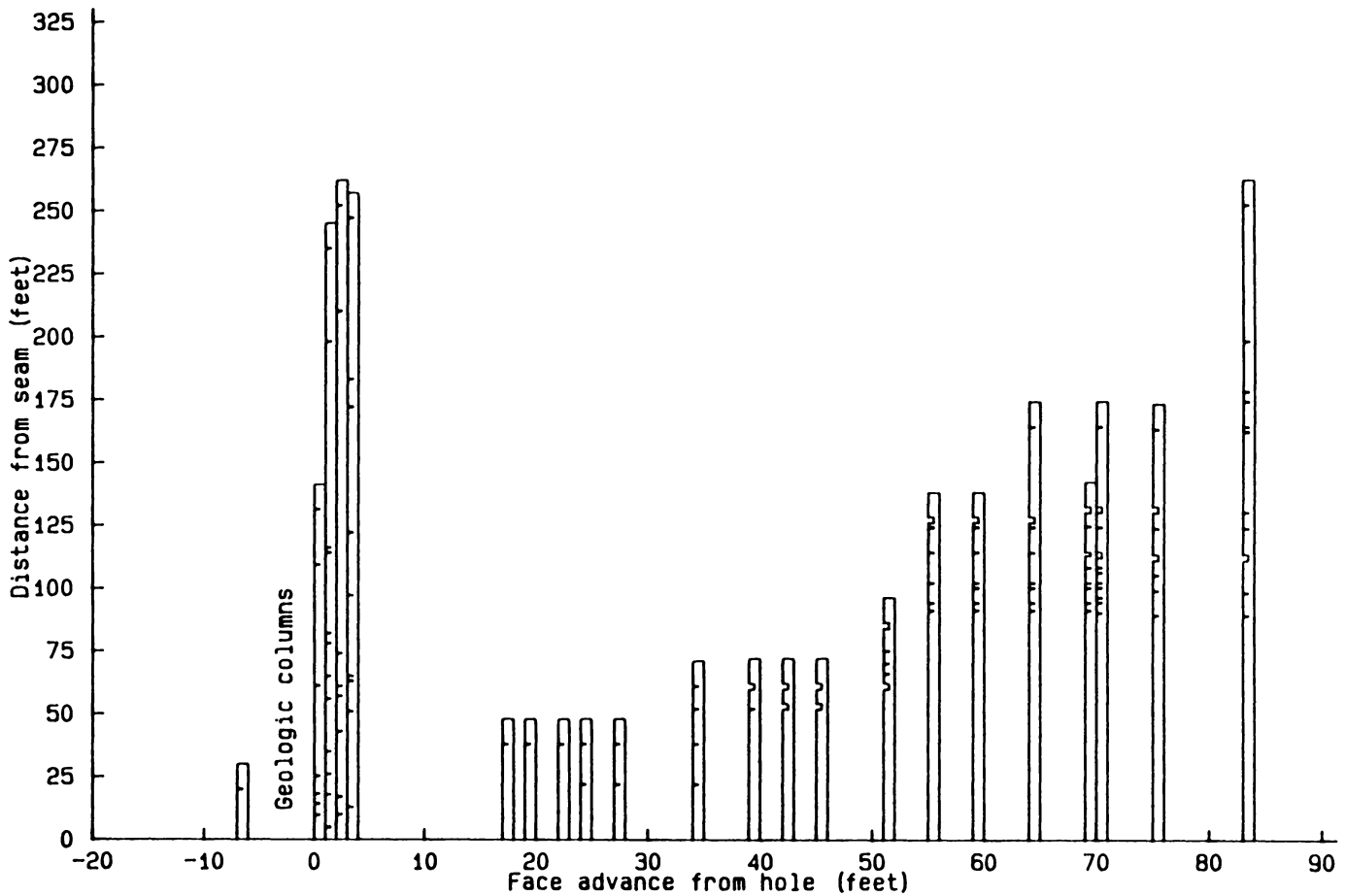

Figure 6.7 **Measurements of Overburden Movement (Borehole C, Case Study U2)**

Table 6.3a Immediate Roof Parameters for Case Study U2

Rock Type	Density [lbs/ft^3]	Thick-ness [feet]	Initial Bulking Factor	Compressive Strength [psi]	Tensile Strength [psi]	Young's Modulus [psi]	Strength Reduction Factor[4]
gray ss[1]	150	10.0	1.25	9,500	1,400	$1.20\ 10^6$	0.22
bur. gray ss[2]	150	5.0	1.25	9,000	1,200	$1.10\ 10^6$	0.22
interbedded[3]	150	2.5	1.25	8,000	1,000	$1.00\ 10^6$	0.22
shale	150	7.0	1.25	7,200	750	$0.96\ 10^6$	0.22
black shale	150	35.0	1.25	7,200	750	$0.96\ 10^6$	0.22

[1]: gray sandstone
[2]: burrowed gray sandstone
[3]: interbedded shale and sandstone
[4]: for the roof classification method

Table 6.3b Analytical Model Parameters for Case Study U2

Total Layers	5
Seam Thickness [feet]	4.2
Panel Width [feet]	600
Total Entry Width [feet]	40
Total Advance [feet]	500
Advance Increment [feet]	2

Table 6.4 First Weighting Calculations for Case Study U2
(Thickness of First Layer = 10 feet)

Method	Distance [feet]
Plate theory	114
Roof Classification	200
Simple Tension Formula[1] (Bulking Factor = 1.25)	147
Simple Tension Formula[1] (Bulking Factor = 1.50)	104

[1]: equation [2.10]

Table 6.5 Caving Height Calculations for Case Study U2

Method	Bulking Factor	Caving Height [feet]
Plate Theory	1.10	> 50
Plate Theory	1.15	> 50
Plate Theory	1.20	25
Plate Theory	1.25	25
Volumetric Expansion[2]	1.25	17

[2]: equation [2.1]

for which direct measurements were performed, and do not necessarily reveal the strata deformation mechanisms. Determination of in situ strata properties, the bulking factors of the different materials, and other empirical coefficients are essential to these calculations.

The differentiation between the immediate and the main roof and the process of bed separation and recontact were identified, and an attempt was made to represent this deformation in the numerical formulation. The model employing a disturbed zone, for example, examined the behavior of the mesh when the inelastic zone over the opening (the immediate roof and part of the fractured roof) was removed from the formulation. It was, however, determined in the preliminary analysis that such a model lacked the flexibility to exhibit deformation patterns when the **driving** criterion varied. Figure 6.8 compares the measured subsidence curve to subsidence curves obtained using (a) a full mesh under a linear formulation, (b) a full mesh after multiple iterations based on a non-linear formulation, and (c) a restricted mesh. It can be observed that, although the use of the restricted mesh differentiated the influence area from the intact rock area, the shape of the measured profile was not successfully approximated. It should be noted that, since the restricted model appeared to be insensitive to changes in the elastic properties, both under nodal forces and fixed displacement formulations, the application of a scaling factor on the calculated displacements was not theoretically justified. Therefore, the restricted model could not even approximate maximum deformation values. Additionally, the displacements calculated by the second iteration of the non-linear formulation were equally scaled to those calculated by the first iteration, which incorrectly suggested a reduction in vertical movement under material failure.

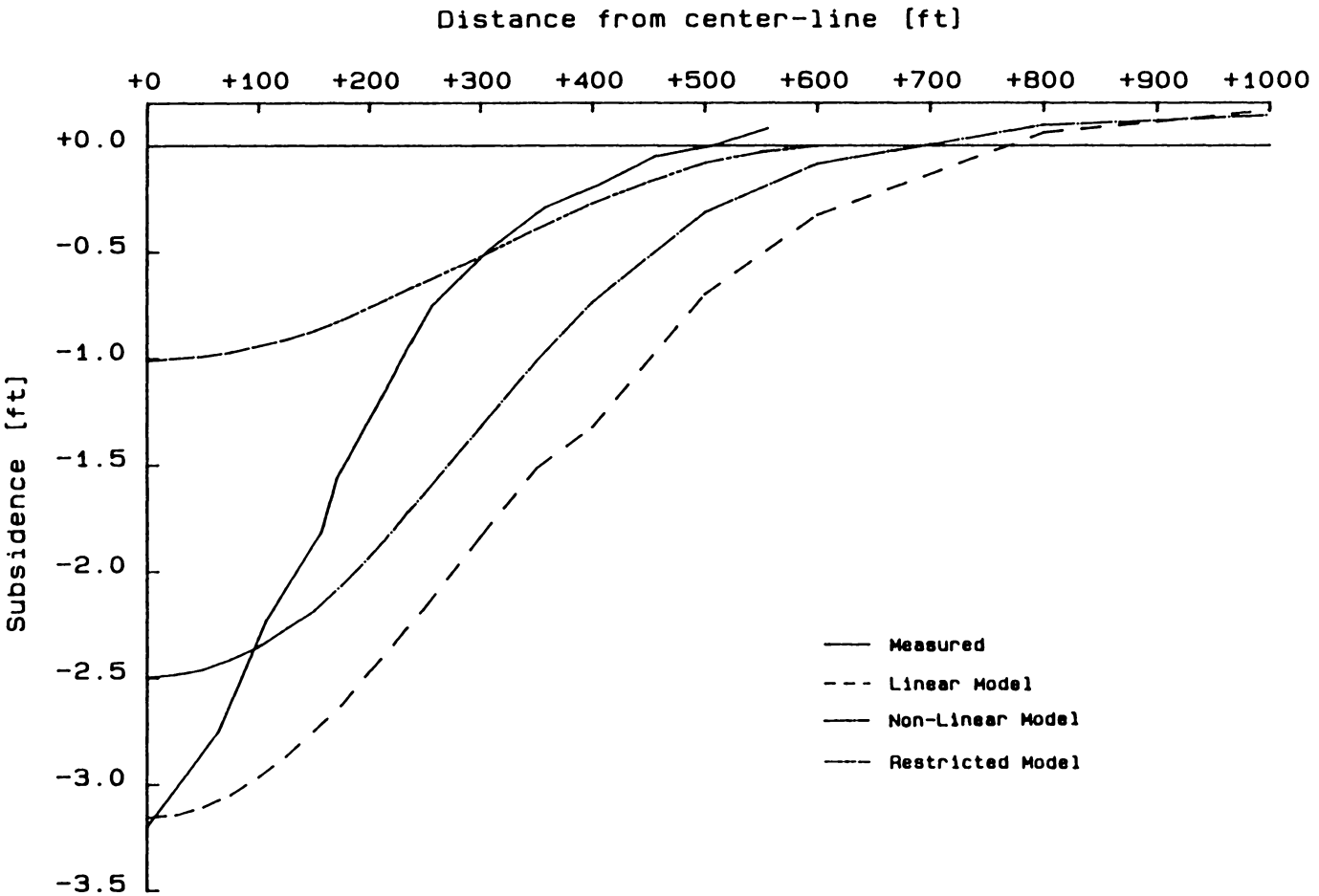

Figure 6.8 Comparison of Subsidence Profiles Obtained from Linear, Non-Linear, and Restricted Models

On the other hand, the joint elements introduced into the immediate roof and the lower main roof simulated the effects of bed separation with respect to overburden movement and deformation. Figure 6.9 shows a typical example of bed separation, obtained in the immediate roof, which decreased with increasing distance from the seam. Surface deformation patterns, however, did not match those measured when employing both failing and/or non-failing joints, as shown in Figure 6.10. This was attributed to the fact that the presence of failing joint elements (implemented when separation occurred) reduced the effect of the driving mechanism to the upper layers of the overburden, resulting in lower surface subsidence values and no significant change in the shape of the profiles. Furthermore, the **loosening** of the global stiffness matrix, achieved through the use of such elements, did not have a pronounced effect on the calculated surface subsidence profiles.

The observation that the coal measure strata encountered in certain case studies exhibited reasonably similar elastic properties was utilized in simplifying the input to the numerical models. Uniform initial overburden properties could not be assumed for all case studies, but coal measure strata that had not undergone extreme metamorphism (Case Study U1) usually exhibited similar corresponding properties. Additionally, since it was previously demonstrated that the **ratio** between the different properties employed had a more pronounced effect on model behavior than did the absolute magnitude of the values, simple guidelines for model construction could be established.

6.2 Numerical Approach

An approach based on an iterative mathematical procedure, which can detect the failing elements and subsequently adjust their properties, is a complicated process requiring

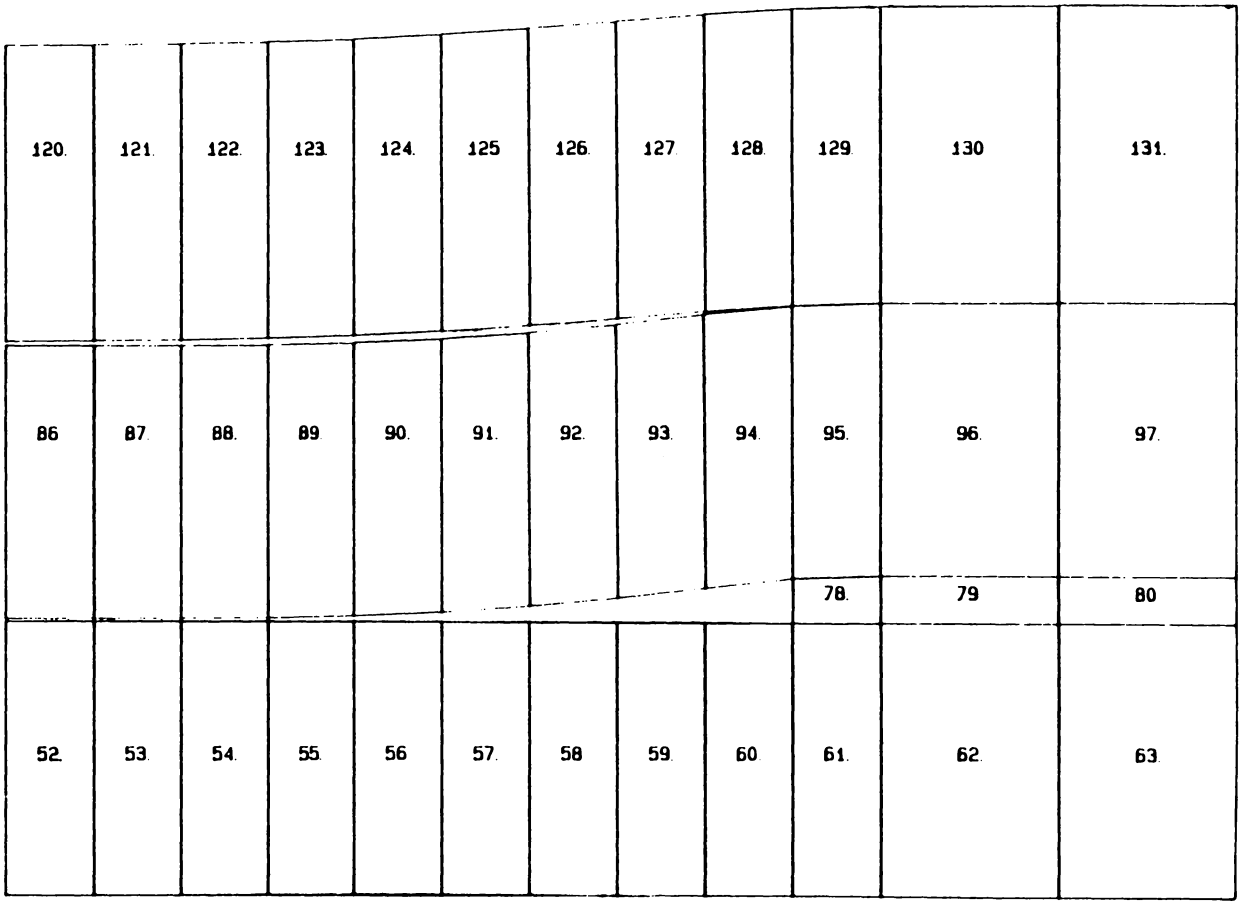

Figure 6.9 **Calculated Separation along Joint Elements (Scale Factor for Vertical Displacements = 4.0)**

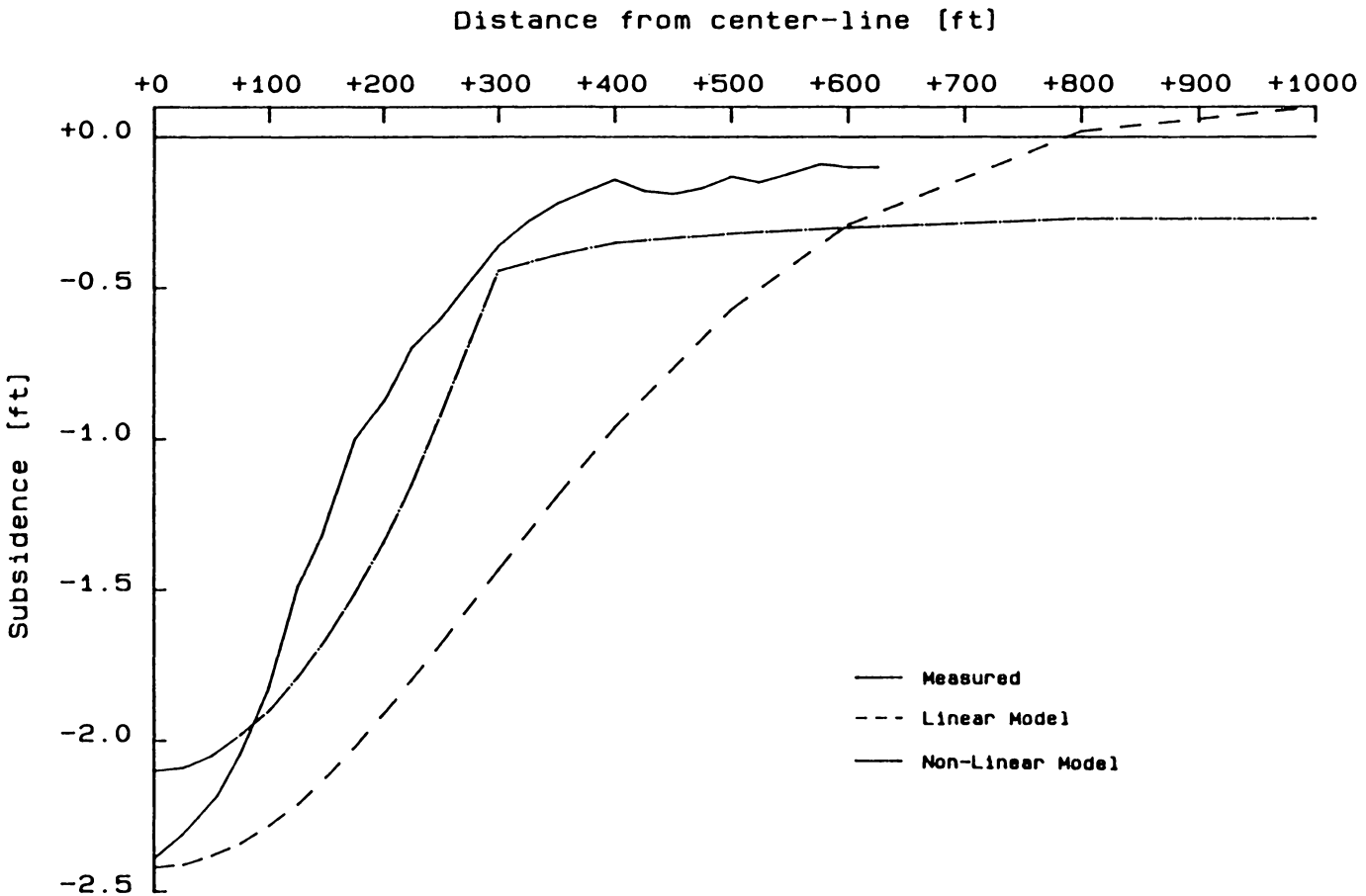

Figure 6.10 Comparison of Subsidence Profiles Obtained from a Linear and a Non-Linear Model, Using Joint Elements

very precise failure criteria and exact determination of both the initial elastic properties of the innerburden and the initial stress field. Even when these requirements are met, empirical information available for a specific region cannot easily be incorporated into the model for adaptation to a given application. It should also be emphasized that such models have not generally produced satisfactory results with respect to prediction of horizontal strains on the surface (Holt and Mikula, 1984). This may be due to the difficulty of utilizing empirical data, as well as due to the fact that a relationship between the observed surface phenomena and overburden deformation mechanisms, with their resulting stress states, has not been correctly established. As a result, an attempt was made to pre-assign lower elastic properties to elements that would be in a highly stressed zone when failure was initiated. Surface phenomena were interpreted in terms of element stressing, and their effects were subsequently translated into the overburden in order to establish vertically oriented zones.

Analysis was performed under the assumption that a satisfactory match between measured and fitted values could subsequently allow a correlation of strata behavior and deformation patterns, in order to relate empirical data to overburden deformation mechanisms. Furthermore, the ability of the model to predict surface deformations could then be evaluated.

6.2.1 Model Formulation

A mesh was generated for every case study according to the geometry of the panel cross-section, with element size decreasing in the area around the rib of the excavation. In the case of longwall panels, the opening width was set equal to the panel half-width. In the case of room-and-pillar panels, if the panel was supercritical ($W/h > 1.2$), then the opening was set at approximately $0.6h - 0.7h$. Otherwise, it was set equal to half the

dimension of the panel in the direction of the cross-section. An alternative approach to reducing the opening width for the supercritical cases was to modify the roof convergence curve, as presented below, in order to reflect such conditions. The latter approach was considered to represent the geometry and physical characteristics of the panels better than did the former. Varying properties were then assigned to different overburden zones (Figure 6.11), which were defined as follows:

- The **Intact Zone**, or **Zone 1**, included the strata below the seam and the undisturbed rock outside of the influence area. The latter was bounded by a line connecting the rib to a surface point, defined by either the location of the break point, or one-half of the distance of the draw point from the rib. During model validation the location of the break point was calculated directly from the measured strain profiles. The rock strata corresponding to this zone were assumed intact, and appropriate properties were assigned to the elements.

- The **Fractured Zone**, or **Zone 3**, included the high shear area around the inflection point (i.e. the transition between tension and compression, as it developed through the overburden strata). The location of the inflection point on the surface was calculated for each case study, according to the empirical equations given in Chapter 5. During model validation, the location of the inflection point was calculated from the actual surface deformation profiles available for the case studies.

  Zone 3 was defined by two lines. Each line was defined by a point on the surface and a point at seam level, respectively. The left boundary line connected a surface point located within 50 feet of the point of maximum subsidence, if the panel was subcritical, or the point of maximum subsidence, if the panel was supercritical, to the rib of the excavation. The right boundary line of this zone (Zone 3a in Figure

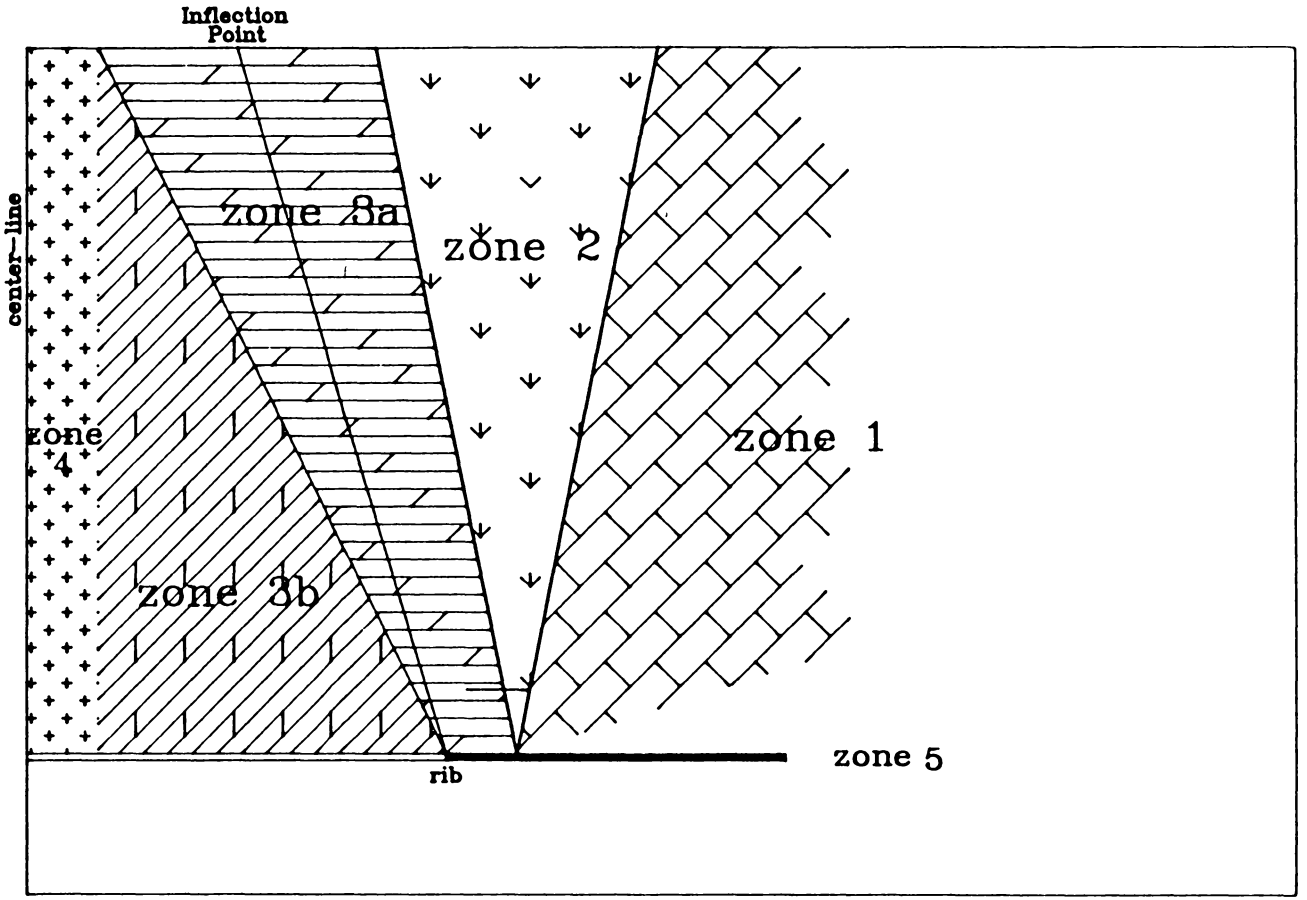

Figure 6.11 **Definition of Overburden Zones, Based on Strata Deformation Characteristics**

6.11) connected a surface point, located symmetrically to the left boundary point, with respect to the inflection point, to the outer edge of the element on the rib of the excavation at seam level. Additionally, the right boundary point was always kept within the point defined by the surface projection of the excavation rib. The material properties assigned to this zone typically measured 1/60 of those of the intact rock. It was subsequently determined that extending Zone 3 all the way to the seam level (Zone 3b) eliminated the need for defining an additional zone, and thus simplified the construction of the model. Furthermore, the lower portion of Zone 3b corresponds to the highly fractured immediate roof.

- The **Intermediate Zone**, or **Zone 2**, was defined between the outermost boundary of Zone 3 and the boundary of Zone 1, over the rib of the excavation. The elastic properties assigned to the elements in this zone typically measured 1/30 of those of the intact rock. The location of the break point (BP), when available, was also used to define the right boundary of this zone, as mentioned under the definition of the intact zone. It should be noted that the location of the break point also indicated the extent of severe influence which the underground workings exerted upon the surface.

- The **Affected Zone**, or **Zone 4**, extended from the innermost boundary of Zone 3 to the center-line of the panel. In this zone, the strata was assumed to have been primarily subject to translation, without being exposed to the high stresses associated with the high shear zone. The strata was, therefore, initially assumed to be slightly weaker than the original intact rock. However, since the zone was in the middle of the disturbed strata, and had been subjected to dynamic phenomena, its elastic properties were assumed to be 1/5 to 1/10 of those of the intact rock.

During the preliminary analysis, it was determined that the magnitude of the elastic properties assigned to Zone 4, with respect to the corresponding properties of the intact rock, had a great influence on the maximum subsidence value (S_{max}) and the maximum compressive strain value ($-E_{max}$), as calculated by the model. This sensitivity, however, could be controlled through the application of a scaling factor to the calculated displacements, as explained below.

- The **Extraction Zone**, or **Zone 5**, represented the coal seam. The elastic properties assigned to this zone ranged from 1/10 to 1/30 of those of the intact rock.

The Poisson's ratios associated with the different zones were not subject to such reductions, although the ratios assigned to weaker zones were consistently lower than those assigned to competent zones. Table 6.6 summarizes the elastic moduli and Poisson's ratios assigned to each zone.

6.2.2 Roof Convergence Curve

Before failure could be initiated, it was necessary to define the displacement assigned to the nodes surrounding the opening, which would provide the **driving** mechanism for mesh deformation. As already mentioned, such fixed displacements were only assigned to the nodes comprising the roof of the opening. Floor movement was assumed to be negligible for the case studies under consideration. It should also be noted that initial horizontal displacements were not assigned to these nodes and, therefore, were free to move along the horizontal direction.

In the case of subcritical or critical panels (i.e. width-to-depth ratio (W/h) $<=$ 1.2), the node on the center-line of the panel (symmetry axis) was assumed to have maximum

Table 6.6 Elastic Properties Assigned to Each Zone

Zone Number	Description	Young's Modulus	Poisson's Ratio
1	Intact Zone	E_1	0.25
2	Intermediate Zone	$1/30 \times E_1$	0.20
3	Fractured Zone	$1/60 \times E_1$	0.10
4	Affected Zone	$1/5\text{-}1/10 \times E_1$	0.25
5	Extraction Zone	$1/10\text{-}1/30 \times E_1$	0.20

convergence, i.e. equal to 97-98% of the extraction thickness. Roof convergence was assumed to decrease linearly from that node to the node on the rib of the excavation, as represented by curve 1 in Figure 6.12. Piece-wise linear curves (curve 2, Figure 6.12) were attempted, but no significant difference was observed on the surface deformation curves, since the difference in initial roof convergence was small. Moreover, the definition of such curves was more complicated than that of the linear curves.

In the case of supercritical panels, (W/h) > 1.2), the roof convergence curve needed to be adjusted (curve 3, Figure 6.12) in order to allow maximum surface subsidence to remain constant in the supercritical areas.

The numerical procedure, therefore, was much more accurate when the approximate location of the point of maximum subsidence could be estimated. As already discussed, the different empirical subsidence prediction methods (i.e. the profile function method) can approximate the location of the point of maximum subsidence, given the geometry of the panel and geology of the overburden.

The definition of the roof convergence curve for a particular case study reflects the effect of the in situ stresses on the roof of the opening during mining. A conventional translation of such stresses into nodal forces would follow the mathematical formulation described in Section 3.6. This, however, assumes uniform nodal forces along the opening, without considering the effect of the rib. The latter, alternatively termed the **edge effect**, in essence diminishes the effect of gravity forces on the roof, since part of the theoretically imposed load can be absorbed by the rib.

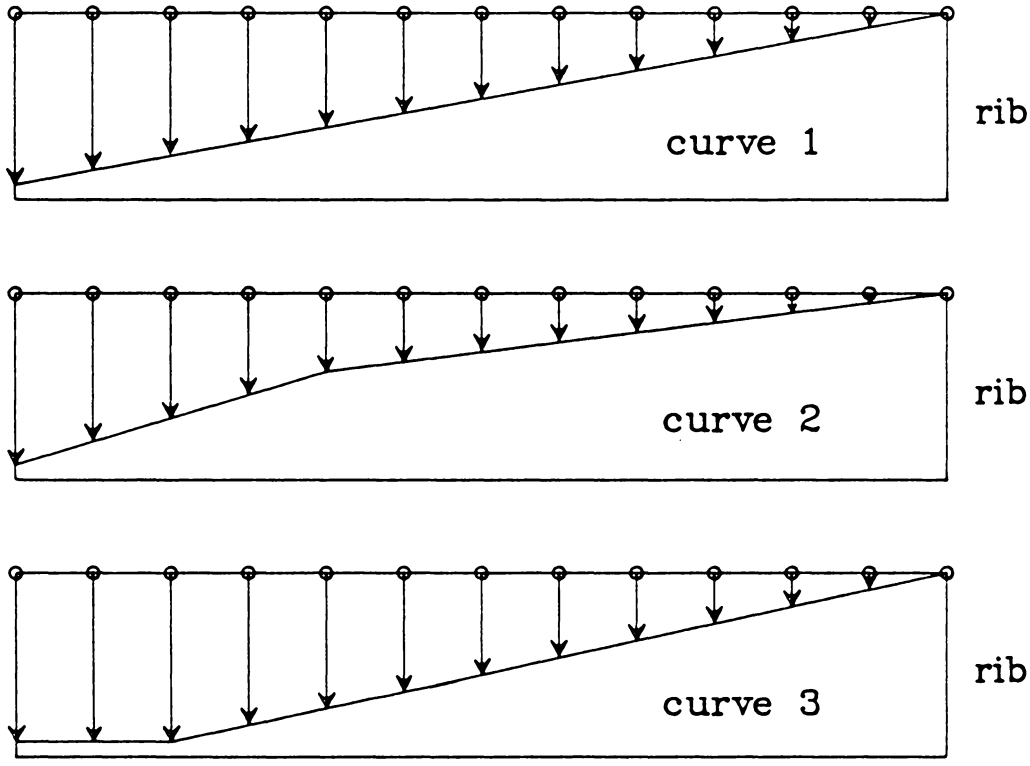

Figure 6.12 Roof Convergence Curves: (1) Linear; (2) Piece-wise Linear; (3) Super-critical Panel

6.2.3 Scaling of Displacements

As already mentioned, the ratio of the elastic properties assigned to the elements in Zone 4 to the intact rock properties had a great influence on the maximum subsidence value obtained by the numerical model. In order to simplify data input, this ratio was assumed constant for all case studies. Adjustment of the resulting displacements, however, was necessary in order to scale the maximum subsidence value down to that predicted by the empirical models. It has already been established that scaling the element properties does affect the model employing fixed nodal displacements as the driving mechanism. In the case of a linear model employing nodal forces, however, variation of the element properties results in an equal percentile variation, which is reflected in the calculated displacements. Similarly, variation in the magnitude of the nodal forces is directly related to the magnitude of the calculated displacements. Utilizing this concept, the magnitude of the fixed displacements defining the roof convergence curve was varied, and an appropriate variation was observed in the calculated displacements. In order to simplify the procedure, however, the roof convergence curve was defined only as a function of the opening dimensions and the location of the point of maximum subsidence, and a scaling factor (calculated by the following equation) was applied directly to all displacements calculated by the **fixed displacement model**, in order to adjust the surface deformation curves:

$$\text{Scaling Factor} = \frac{\text{empirically predicted or measured } S_{max}}{\text{calculated maximum vertical displacement}} \qquad [6.1]$$

It should be noted that displacement scaling cannot be applied when employing non-linear (multiple iteration) formulations, because the application of the failure criteria, and the re-distribution of elastic properties are indirectly related to the initially calcu-

lated displacements (e.g. such criteria usually evaluate element stresses, which are derived from the calculated displacements). Scaling the initial calculated displacements would affect the application of the above criteria and, therefore, would affect the results of subsequent iterations.

6.2.4 Model Validation

In summary, to analyze a given case study using the proposed model, the following steps were necessary:

- construction of the mesh, which described the panel cross-section;
- determination of empirically predicted parameters, such as the location of the inflection point, the maximum subsidence value and the location of the point of maximum subsidence and the angle of draw (the location of the break point on the surface was also of considerable importance to the accurate definition of the zones, since it signified the beginning of the highly deformed region);
- identification of the different material zones, and assignment of the corresponding elastic properties;
- determination of the roof convergence curve, based on the location of the point of maximum subsidence;
- execution of the finite element program;
- scaling of all the resulting displacements, based on the empirically predicted maximum subsidence factor; and
- plotting of subsidence and strain profiles.

It should be noted that the procedure described above pertains to the general model. During model validation, however, the necessary empirical parameters were determined

directly from the available surface deformation profiles, in order to verify the ability of the program to fit a known profile. When the program was used as a predictive tool, as described in Chapter 7, the predicted values for these empirical parameters were employed.

Figure 6.13 shows the mesh and the zone definition for Case Study S2. Figure 6.14 presents the transverse measured subsidence profile over the longwall panel, the profile calculated using the finite element method and, for comparison, the profile calculated using the influence function method (Karmis and Jarosz, 1985)[7]. The scaling factor used to reduce both the vertical and horizontal displacements was 0.815. Figure 6.15 presents the corresponding strain profiles. It should be noted that horizontal strain values were calculated using the following formula:

$$\text{strain}\left[\frac{x_i + x_{i+1}}{2}\right] = \frac{\text{disp}\,[x_i] - \text{disp}\,[x_{i+1}]}{x_i - x_{i+1}} \qquad [6.2]$$

where

x_i = the horizontal coordinate at point i;

disp $[x_i]$ = the calculated horizontal displacement at point i.

The calculated subsidence profiles were very close to those measured, considering the general definition of the zones and the coarse mesh utilized. A discrepancy, however, can be noted between calculated and measured strain profiles, which was also present

---

[7] The application of the influence method in the eastern U.S. coalfields, for prediction of surface deformation indices, has been very successful, and the results obtained for the different case studies are presented for comparison.

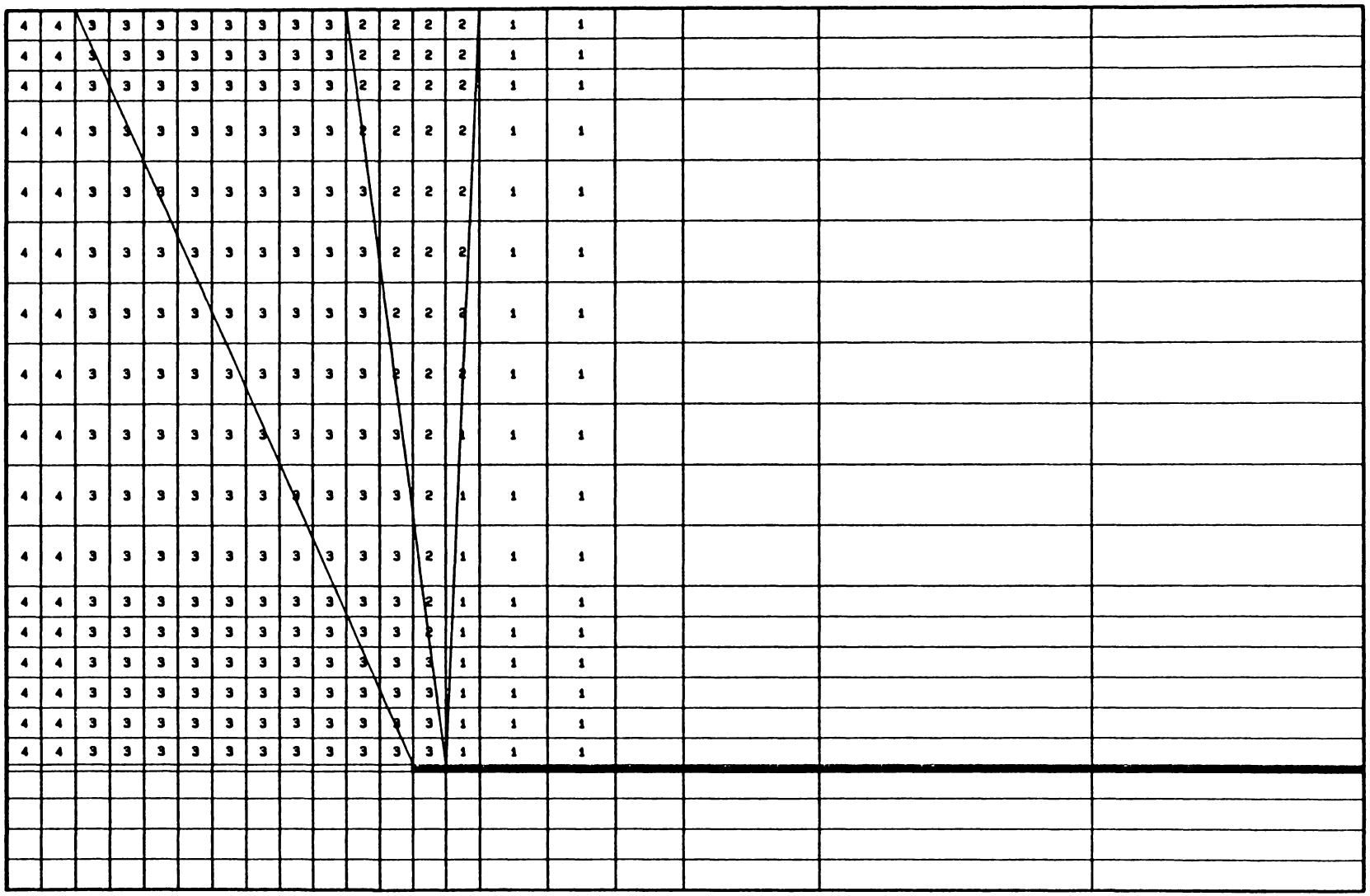

Figure 6.13 Mesh and Zone Definition for Case Study S2

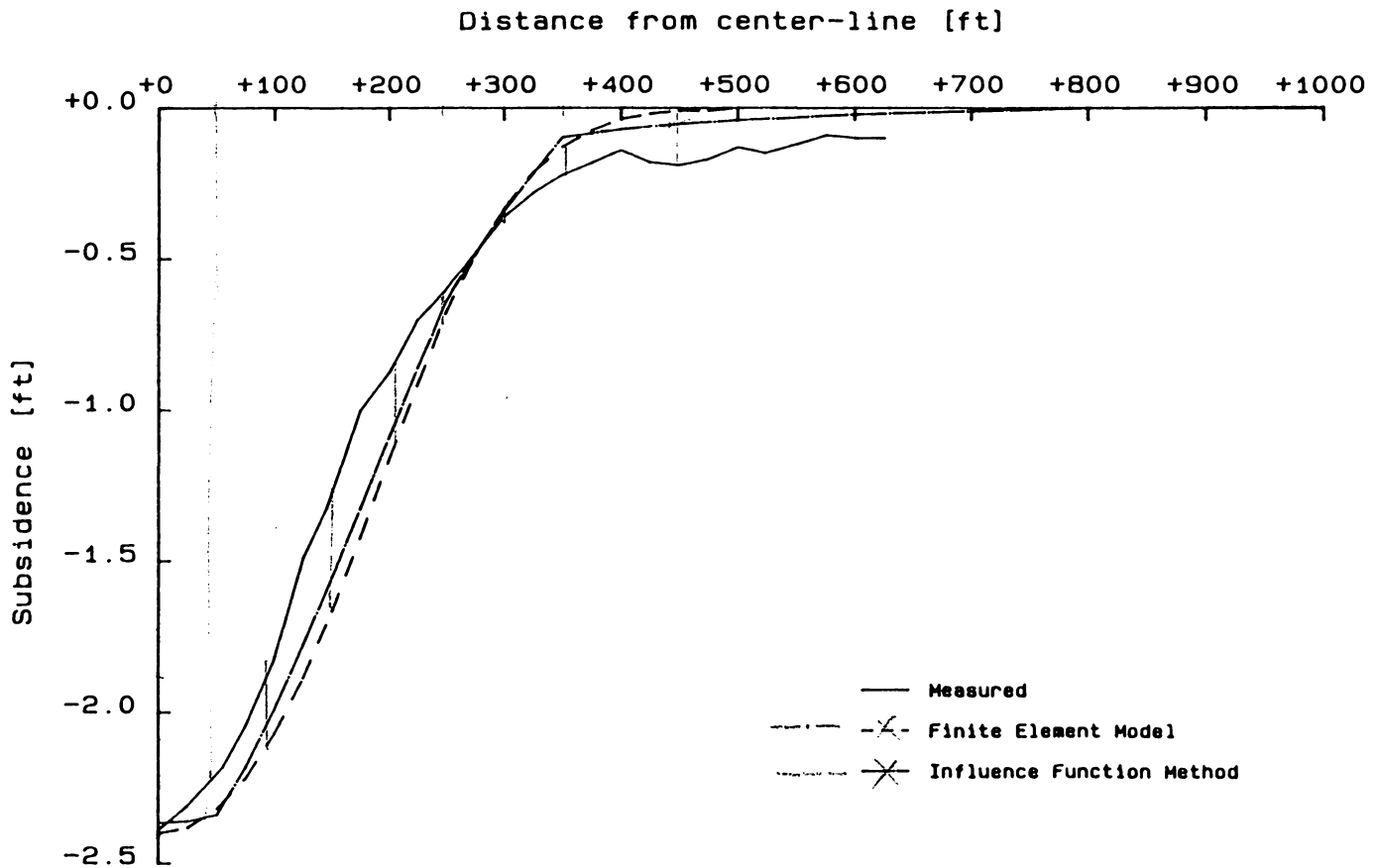

Figure 6.14 Comparison of Measured and Calculated Subsidence Profiles for Case Study S2 Using: (a) the Finite Element Model; and (b) the Influence Function Method

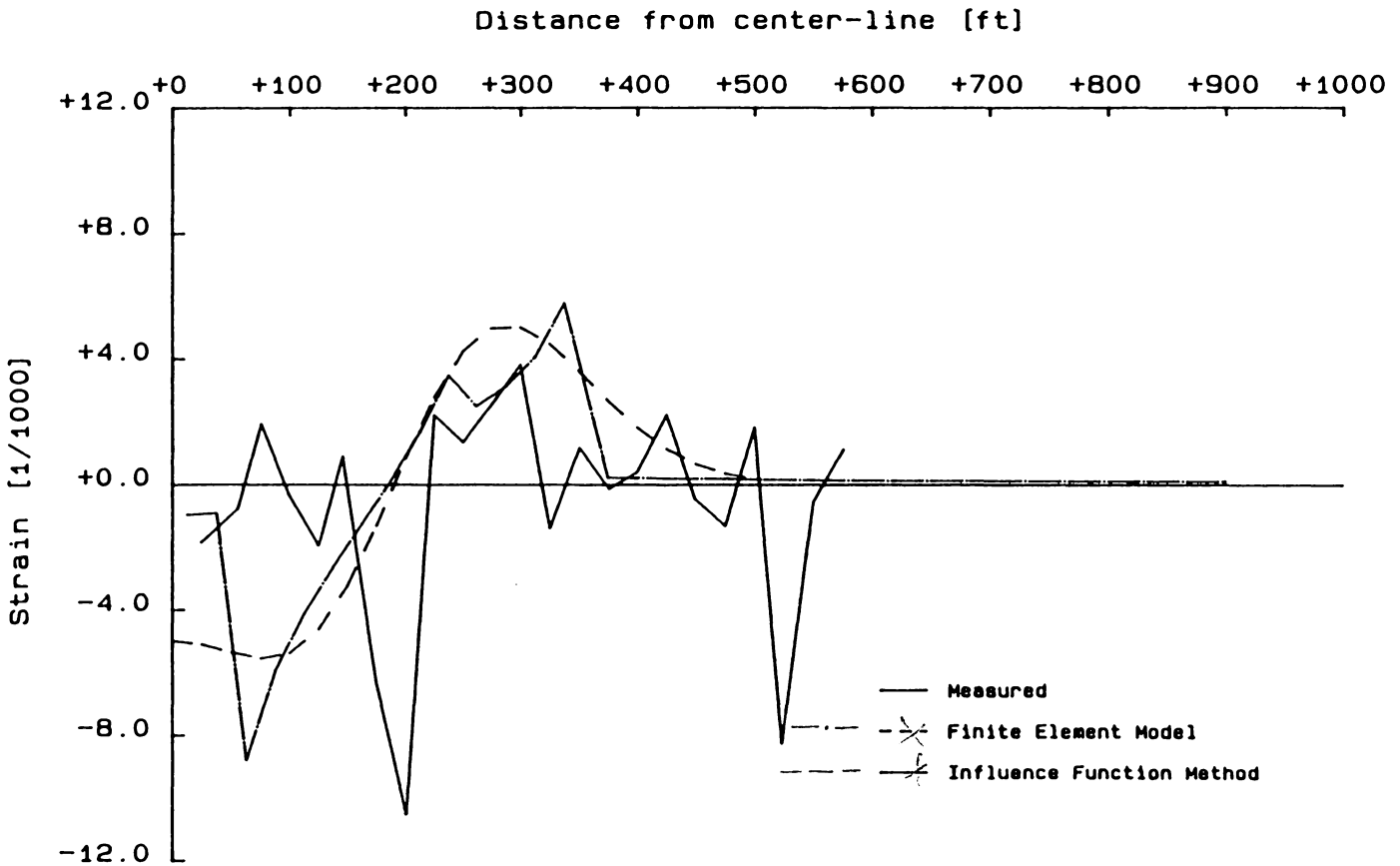

Figure 6.15 Comparison of Measured and Calculated Strain Profiles for Case Study S2 Using: (a) the Finite Element Model; and (b) the Influence Function Method

when comparing the curve calculated through the use of other prediction methods (i.e. the influence function method).

Figure 6.16 shows the mesh and the zone definition for Case Study S3. Figure 6.17 presents the transverse measured subsidence profile over the room-and-pillar panel, the profile calculated using the finite element method and, for comparison, the profile calculated using the influence function method. The scaling factor used was 0.75. Figure 6.18 presents the corresponding strain profiles.

Similarly, the calculated subsidence profiles were considered to be very close to those measured. Although strain profiles are generally difficult to match, the model calculated maximum values close to those measured. The general shape of the profile also fits the one measured.

It should be noted that the calculated subsidence profiles exhibited a significant increase in slope at the boundary between Zones 1 and 3, which can be attributed to the sudden change in material properties between the two zones. A gradual change would have been more appropriate for all transition areas, but that would have complicated the model significantly, since the mesh would have needed to be finer in such areas, and more zones would have had to be defined.

The calculated strain profiles appeared to end abruptly, close to the panel center-line. This is attributable to the fact that the nodes on the panel center-line were rollered and, therefore, could not assume horizontal displacements.

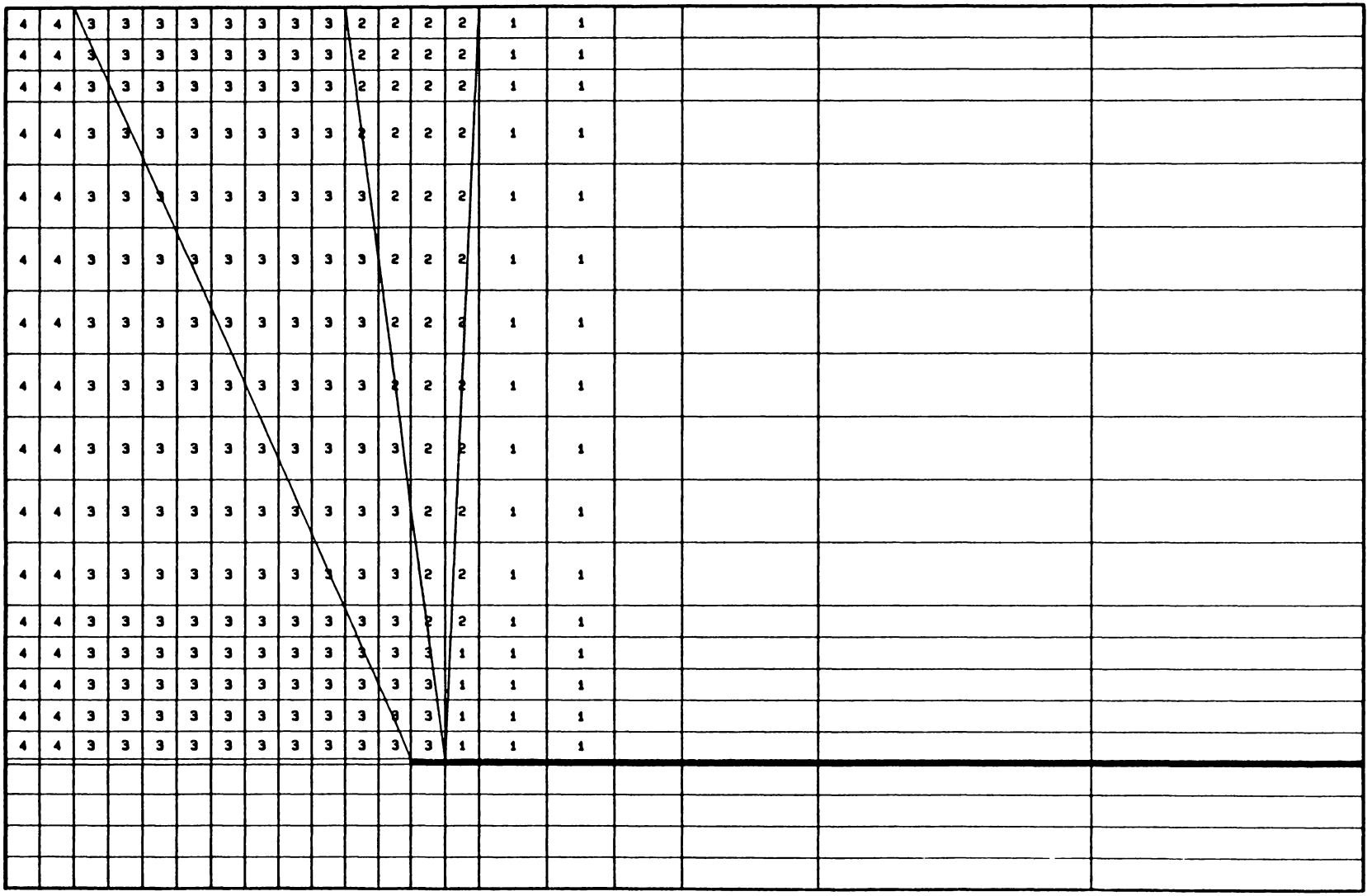

Figure 6.16 Mesh and Zone Definition for Case Study S3

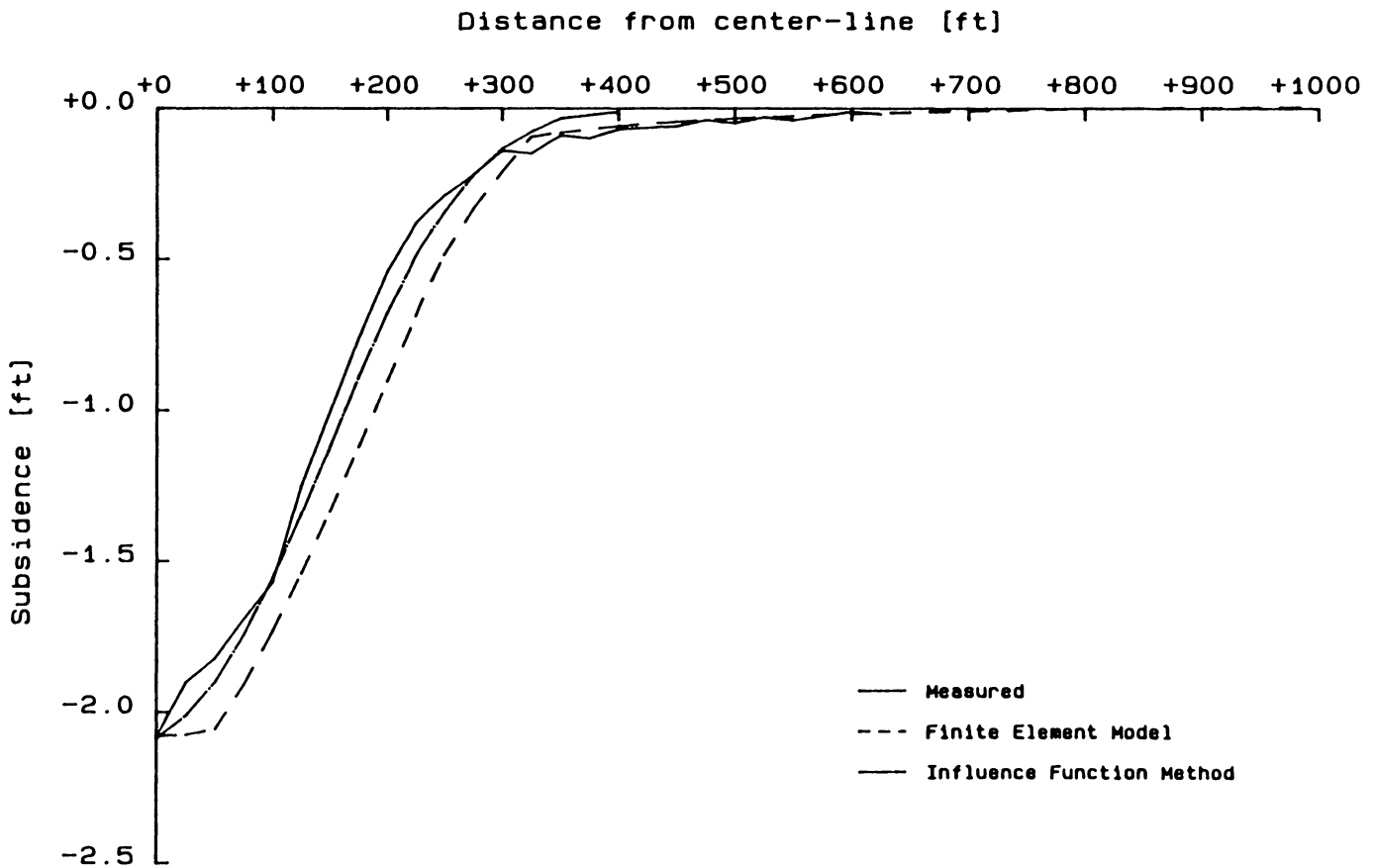

Figure 6.17 Comparison of Measured and Calculated Subsidence Profiles for Case Study S3 Using: (a) the Finite Element Model; and (b) the Influence Function Method

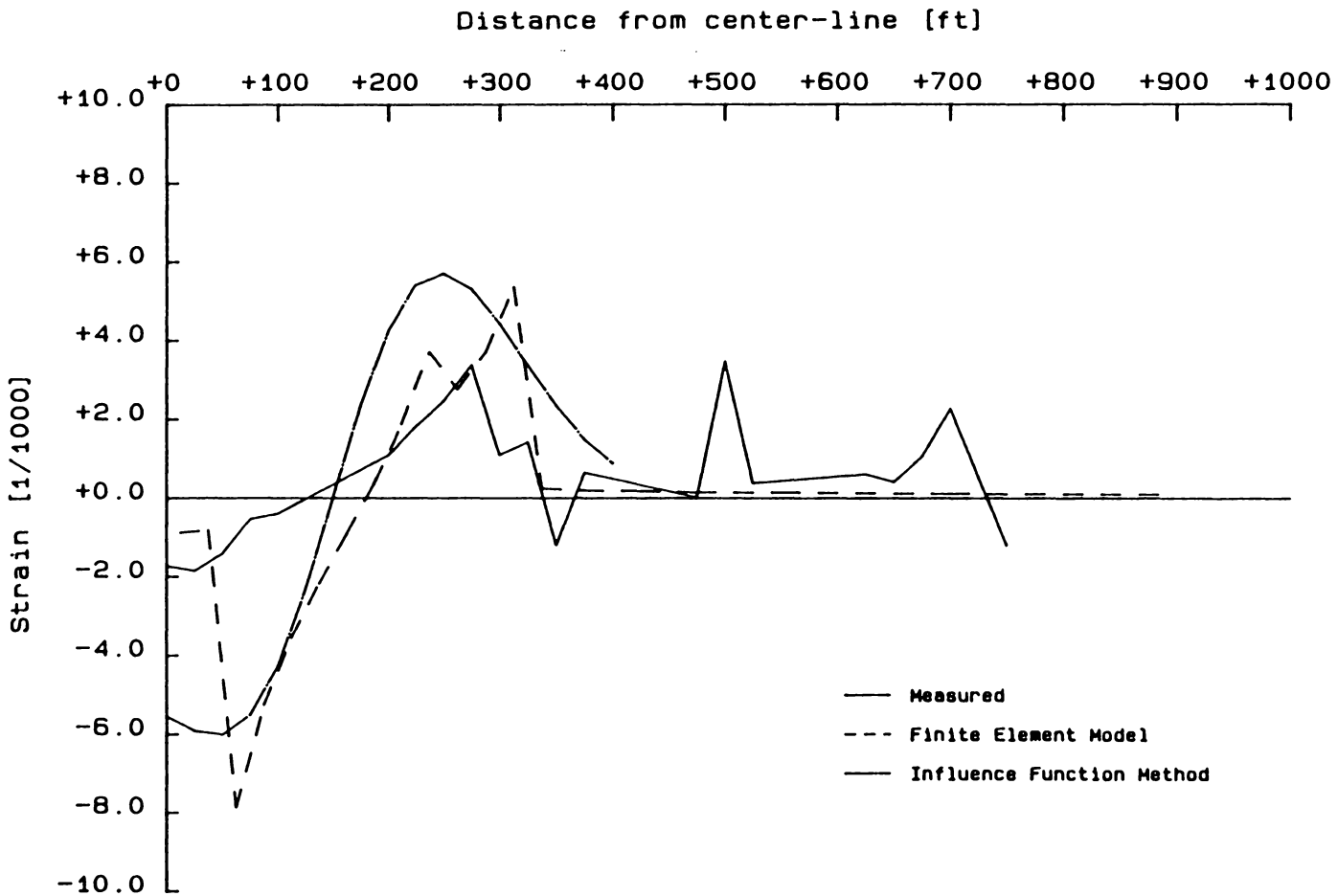

Figure 6.18 Comparison of Measured and Calculated Strain Profiles for Case Study S3 Using: (a) the Finite Element Model; and (b) the Influence Function Method

6.2.5 Conclusions

The model produced a good overall match to the measured subsidence profiles and, also, a good approximation of horizontal strains. The inability to accomplish the latter had previously been a major drawback of the majority of the reported applications on numerical modeling of strata deformation.

The use of empirical data enhances the accuracy of the model, and simplifies the required input with respect to exact representation of overburden conditions and properties.

The use of distinct overburden property zones based on the expected stress conditions (i.e. high shear), proved successful in representing strata conditions and, therefore, in representing corresponding deformations due to these conditions.

The above procedure, although seemingly difficult to implement when employing the fixed displacement nodes to represent roof convergence, was in fact easier to apply than was the procedure utilizing nodal forces as the driving mechanism. Its advantages included elimination of the potential roof-floor overlap problem, and its insensitivity to the absolute magnitude of the elastic properties of the overburden. Also, it did not require definition of any special type of element in order to model gob behavior, and it utilized an already existing surface deformation databank for determining the necessary empirical parameters. Among its disadvantages was the fact that the roof convergence curve had to be defined for every model based on empirical data, without which the procedure may not yield accurate results.

Chapter 7

Application of the Numerical Model

The numerical procedure for calculating deformation characteristics over underground coal mines that was proposed, and subsequently validated, in Chapter 6 can also be used in order to **predict** surface deformations. Its successful implementation complements the existing prediction methods, namely the profile function method, the zone area method and influence function method (Schilizzi, 1987). Furthermore, the influence function method and the proposed numerical model are the only methods capable of calculating horizontal movements, which in turn are necessary in order to calculate horizontal strains. In addition, only the numerical model can be used for parametric analysis, in order to study surface behavior when the geometry and/or elastic properties of the strata are varied.

7.1 Prediction of Surface Deformation Profiles

Once the numerical procedure was established, the model was applied for predicting surface deformation profiles based on empirical data. As previously mentioned, the empirical data was obtained from statistical relationships derived for the eastern U.S. coalfields. The magnitude of the properties assigned to the various zones were kept the

same as those determined during model validation. Additionally, the boundaries of the zones were defined according to the regional empirical model, or were based on empirical information pertaining to more than one panel for the specific case study, if such information was available. Table 7.1 summarizes the data used for predicting surface deformation characteristics for Case Studies S1, S4 and S5.

Figure 7.1 presents the transverse measured subsidence profile over the longwall panel for Case Study S1, the profile calculated using the finite element method and, for comparison, the profile calculated using the influence function method. The scaling factor used to reduce both the vertical and horizontal displacements was 0.73. Figure 7.2 presents the corresponding strain profiles. Although the finite element model predicted the locations of the points of maximum tension and compression displaced with respect to those measured, it was considered a closer approximation than that obtained by the influence function method. It should be noted, however, that the vertical displacements calculated by the influence function method were also scaled by a factor of 1.05, in order to match the maximum subsidence values.

When the numerical model was used to calculate deformations over room-and-pillar mines, the original symmetry assumption, as stipulated for modeling longwall panels, may not be applicable. More specifically, longwall panels are assumed symmetrical around their longitudinal axes, and strata behavior along transverse cross-sections is assumed to be unaffected by "edge-effects". In room-and-pillar mining, however, the excavation is often irregular due to partially extracted pillars, remnant pillars, etc. Half-panel modeling along transverse cross-sections for room-and-pillar panels can still yield satisfactory results provided that the empirical methods can accurately predict the location of the point of maximum subsidence as well as the value of S_{max}. In such cases,

Table 7.1 Empirical Parameters and Zone Definition for Case Studies S1, S4 and S5

Case Study	S_{max} Predicted (Measured)	Inflection Point Predicted	Surface Extends of Zone Boundaries[1]			
			Zone 3		Zone 2	
	[feet]	[feet]	from [feet]	to [feet]	from [feet]	to [feet]
S1	3.11 (3.20)	-90	-250	-50	-50	+ 100
S4	1.17 (1.45)	-100	-250	-50	-50	+ 25
S5	3.62 (3.81)	-100	-200	0	0	+ 100

[1]: Zone boundary distances are given from the rib of excavation. Negative distances indicate displacement towards the center line of the panel.

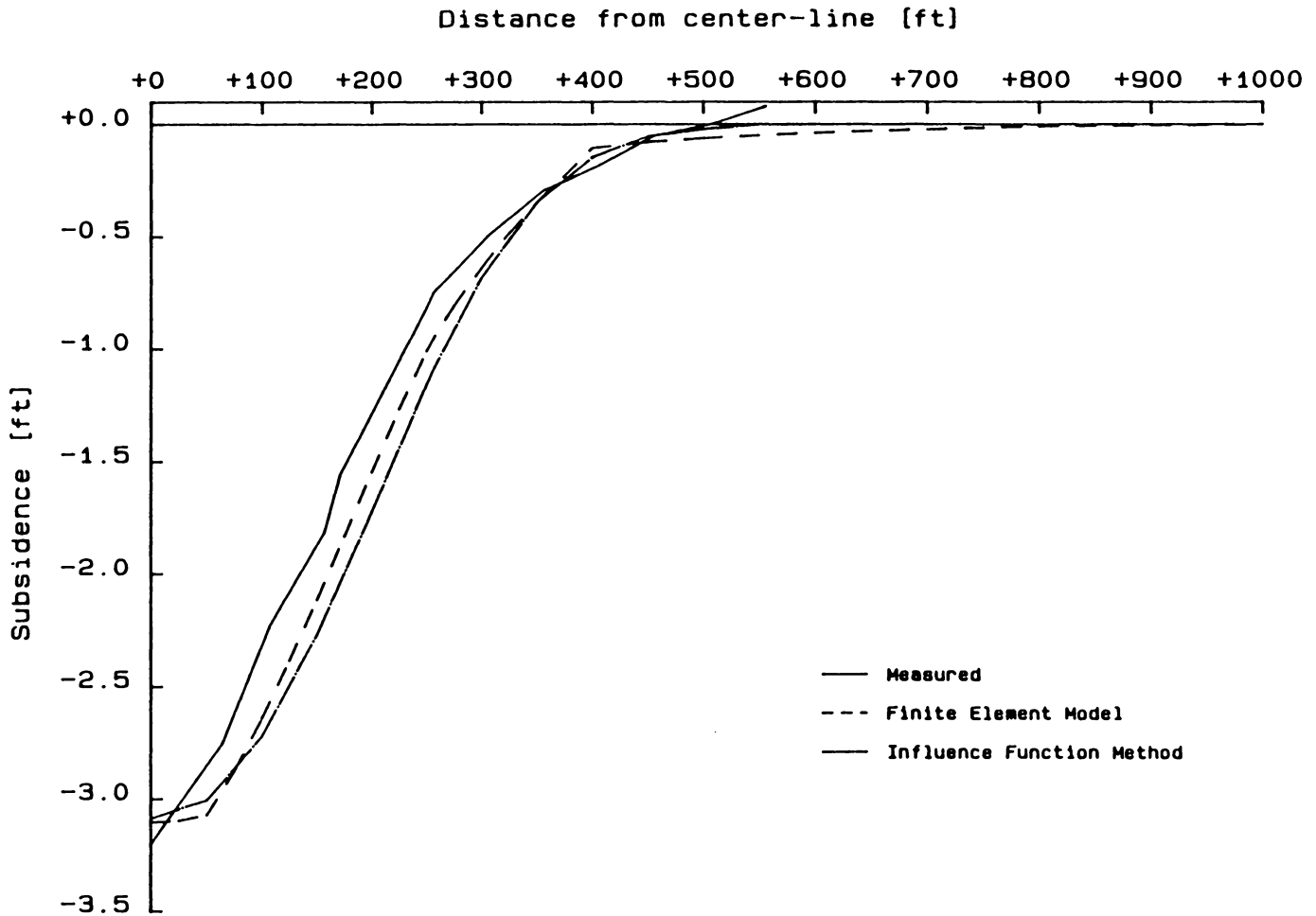

Figure 7.1 Comparison of Measured and Calculated Subsidence Profiles for Case Study S1 Using: (a) the Finite Element Model; and (b) the Influence Function Method

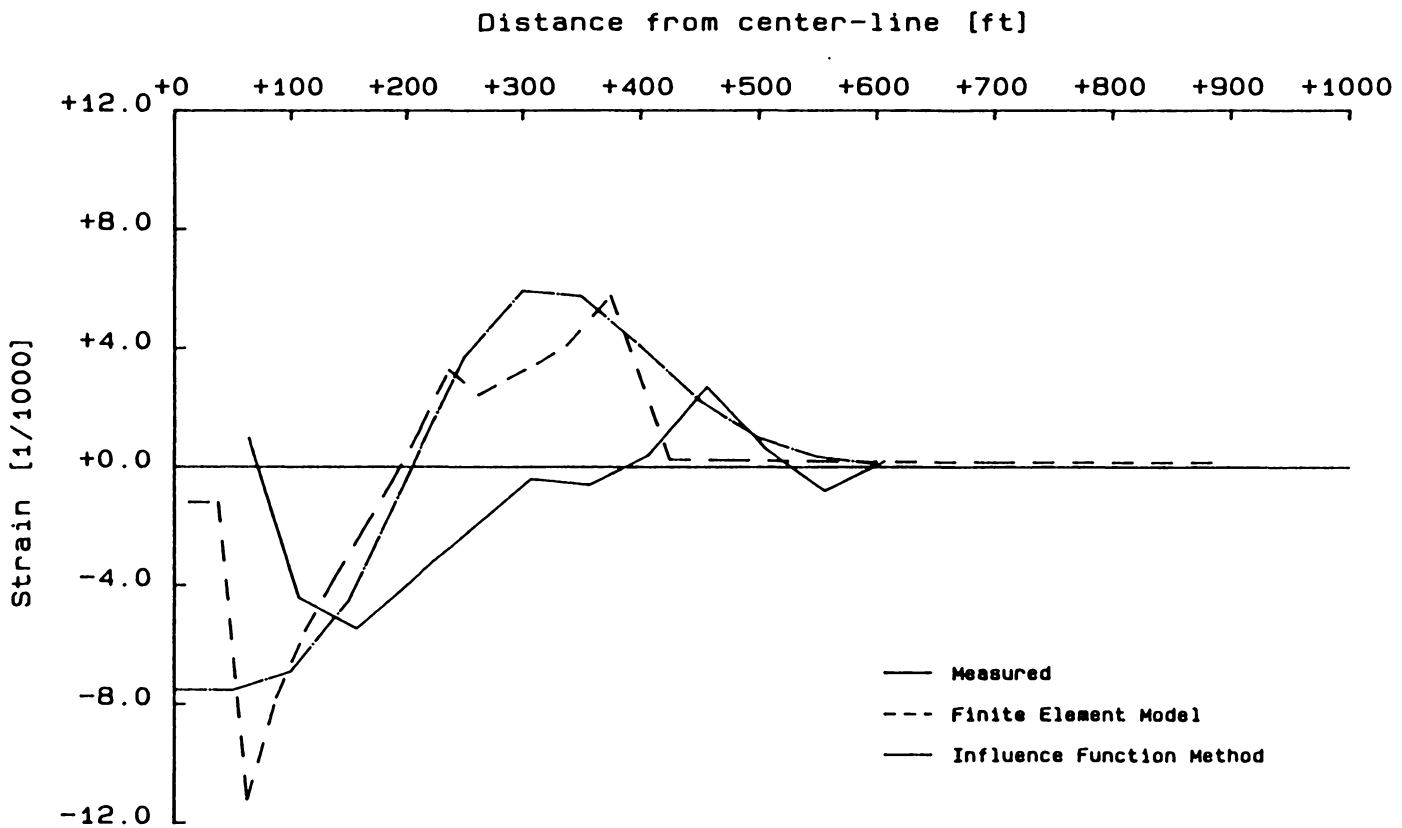

Figure 7.2 Comparison of Measured and Calculated Strain Profiles for Case Study S1 Using: (a) the Finite Element Model; and (b) the Influence Function Method

the mesh is constructed based on an average cross-sectional geometry, and the proposed procedure for setting up the model should be modified in order to represent cross-sections in proximity to complex panel geometry. For example, the roof convergence curve that reflects the failure inducing mechanism may have to be modified to account for the presence of stable (remnant) pillars or other characteristics of the excavation geometry (Figure 7.3).

Modeling the cross-section pertaining to Case Study S4 (Figure 7.4) followed the proposed procedure, since the excavation geometry around the cross-section was assumed uniform. Panel dimensions (Table 5.2) indicated that the panel was supercritical. The roof convergence curve, therefore, had to be adjusted accordingly, in order to reflect these conditions. The shape of the calculated profiles show that the finite element model was successful in simulating the supercritical conditions. Additionally, the horizontal dimension of the elements above the opening was increased from 25 feet (used in the previous models) to 50 feet, in order to reduce the number of elements and nodes in the mesh. This case study was also represented by a different panel geometry, where the opening half-width was set equal to the critical width calculated for the specific geometry (i.e 300 feet). Results obtained by the latter model were similar to those shown, which correspond to the first model. Figure 7.5 presents the transverse measured subsidence profile for Case Study S4, and the profile calculated using the finite element method. The surface displacements predicted by the influence function method are also given for comparison. The scaling factor used to reduce both the vertical and horizontal displacements was 0.71.

A different finite element model was also solved, based on the same mesh geometry, but using a different property distribution. The left boundary of Zone 3 was extended to

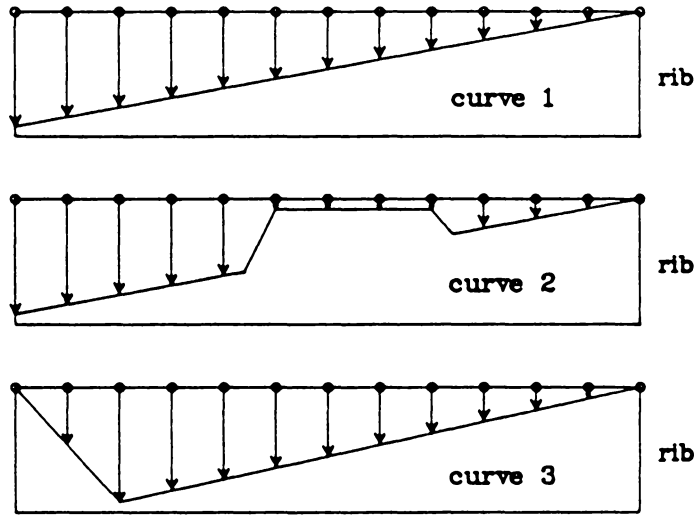

Figure 7.3 Modified Roof Convergence Curves representing various Characteristics of the Excavation Geometry

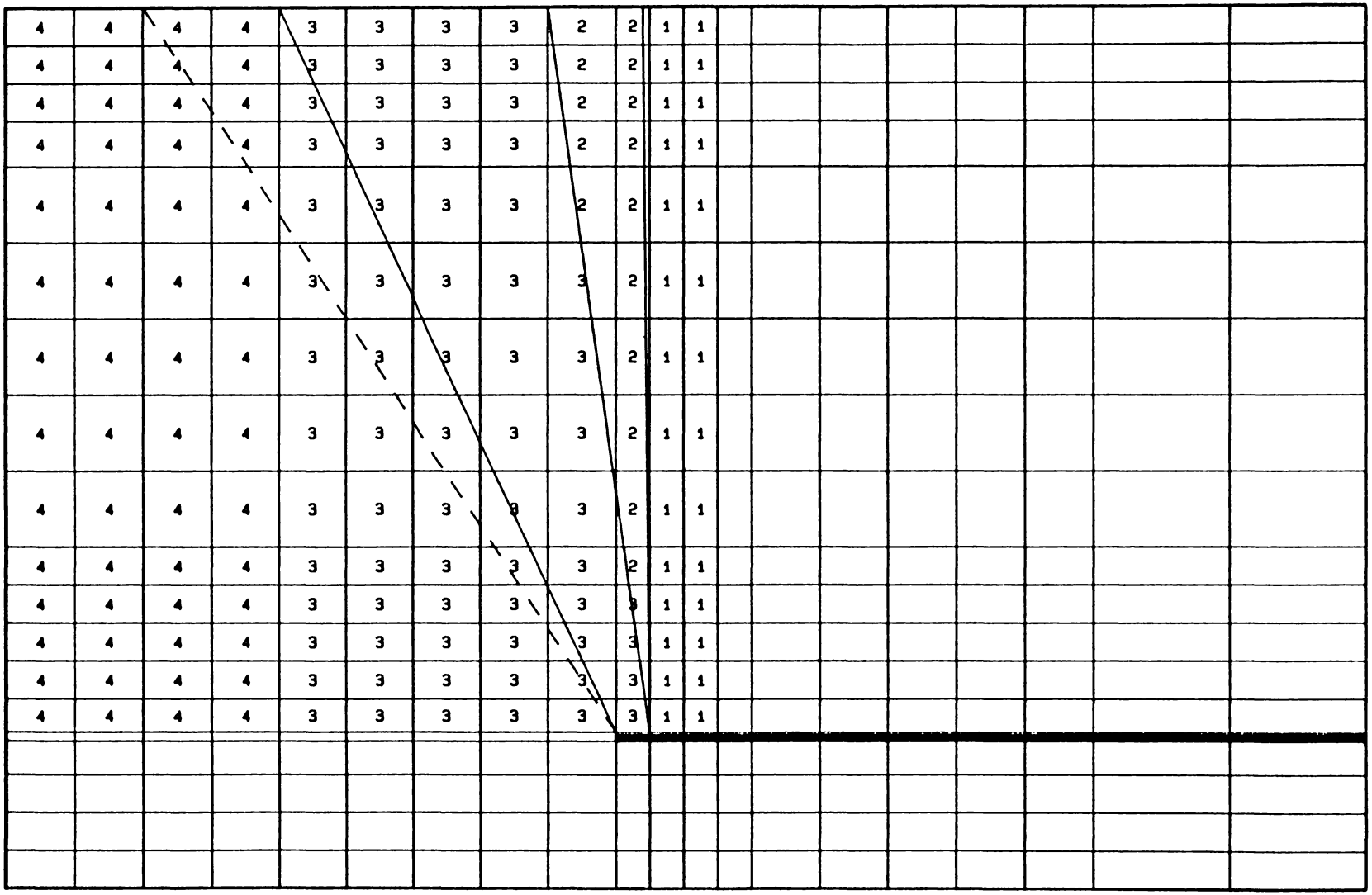

Figure 7.4 **Mesh and Zone Definitions for Case Study S4**

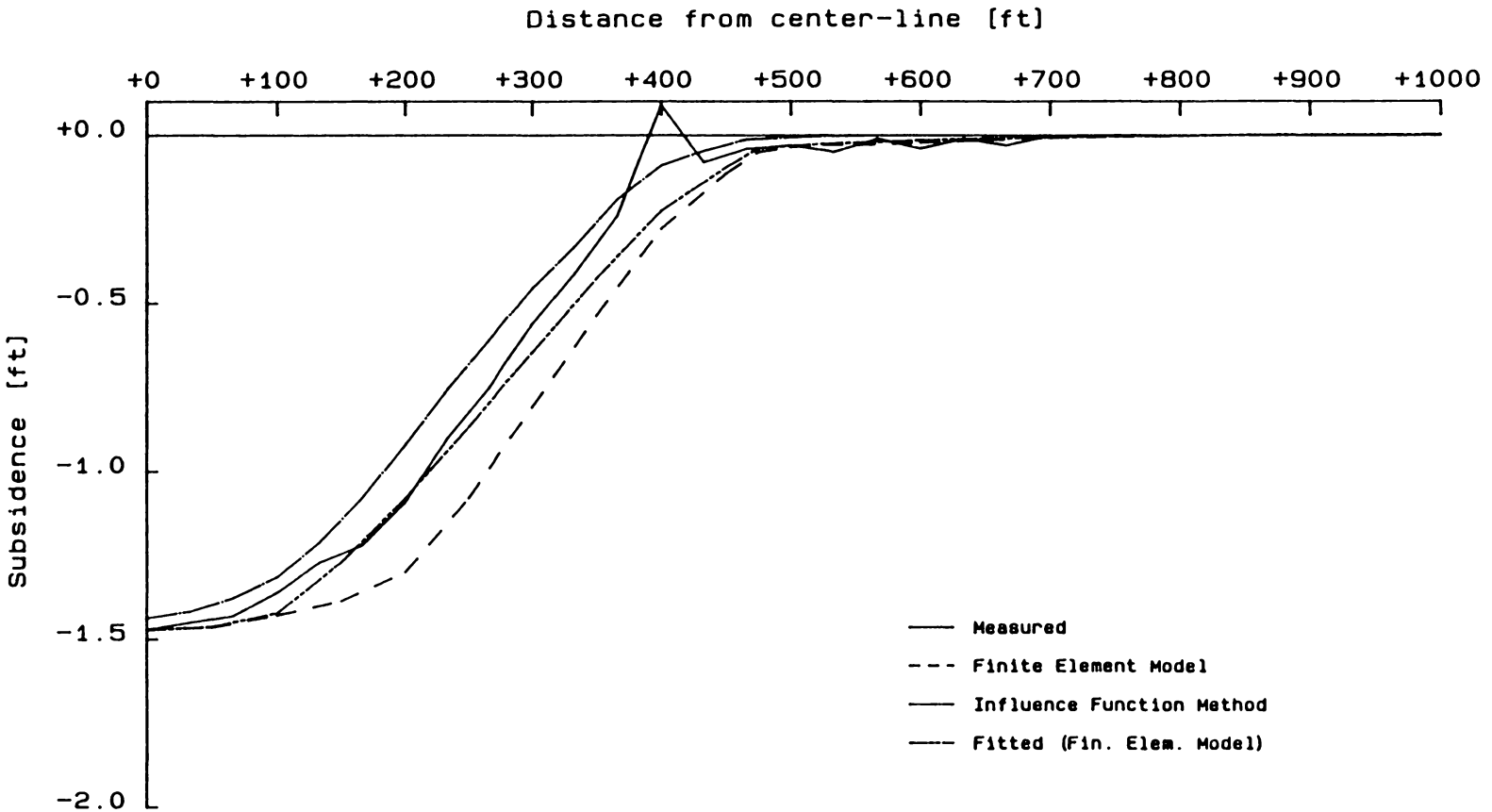

Figure 7.5 Comparison of Measured and Calculated Subsidence Profiles for Case Study S4 Using: (a) the Finite Element Model; (b) the Influence Function Method; and (c) a Modified Finite Element Model (Fitted Curve)

within 100 feet of the panel center-line, thus reducing the width of Zone 4. The magnitudes of the properties used remained the same. This resulted in a very close representation (Figure 7.5) of the measured profile, thus verifying the ability of the model to fit a known curve, and illustrating the difference between the **fitted** and **predicted** surface deformation profiles for the same case study. The differences were mainly attributable to the fact that the procedure followed for obtaining predicted profiles applies to a collection of case studies more than it does to any one mine layout. The scaling factor used for the fitted curve was 0.67. Figure 7.6 presents the corresponding strain half-profiles.

Finally, Figure 7.7 compares the measured and predicted subsidence half-profiles for Case Study S5, while Figure 7.8 presents the corresponding strain half-profiles. The surface displacements predicted by the influence function method are also given for comparison. The scaling factor used to reduce both the vertical and horizontal displacements was 0.79. Panel dimensions indicate again that this longwall excavation has reached supercritical conditions, which were accounted for during mesh definition.

Fitted surface deformation profiles were also calculated for this case study, as shown in Figures 7.7 and 7.8. The width of Zone 2 was reduced by translating the right boundary line by 50 feet towards the excavation rib. Also, the properties corresponding to Zone 4 were reduced by 50% in order to decrease the maximum tensile strain. The scaling factor used to reduce both the vertical and horizontal displacements in this case was 0.82.

7.1.1 Conclusions

The calculated subsidence profiles closely match those measured in the field, as well as the profiles calculated by the influence function method. Additionally, the calculated

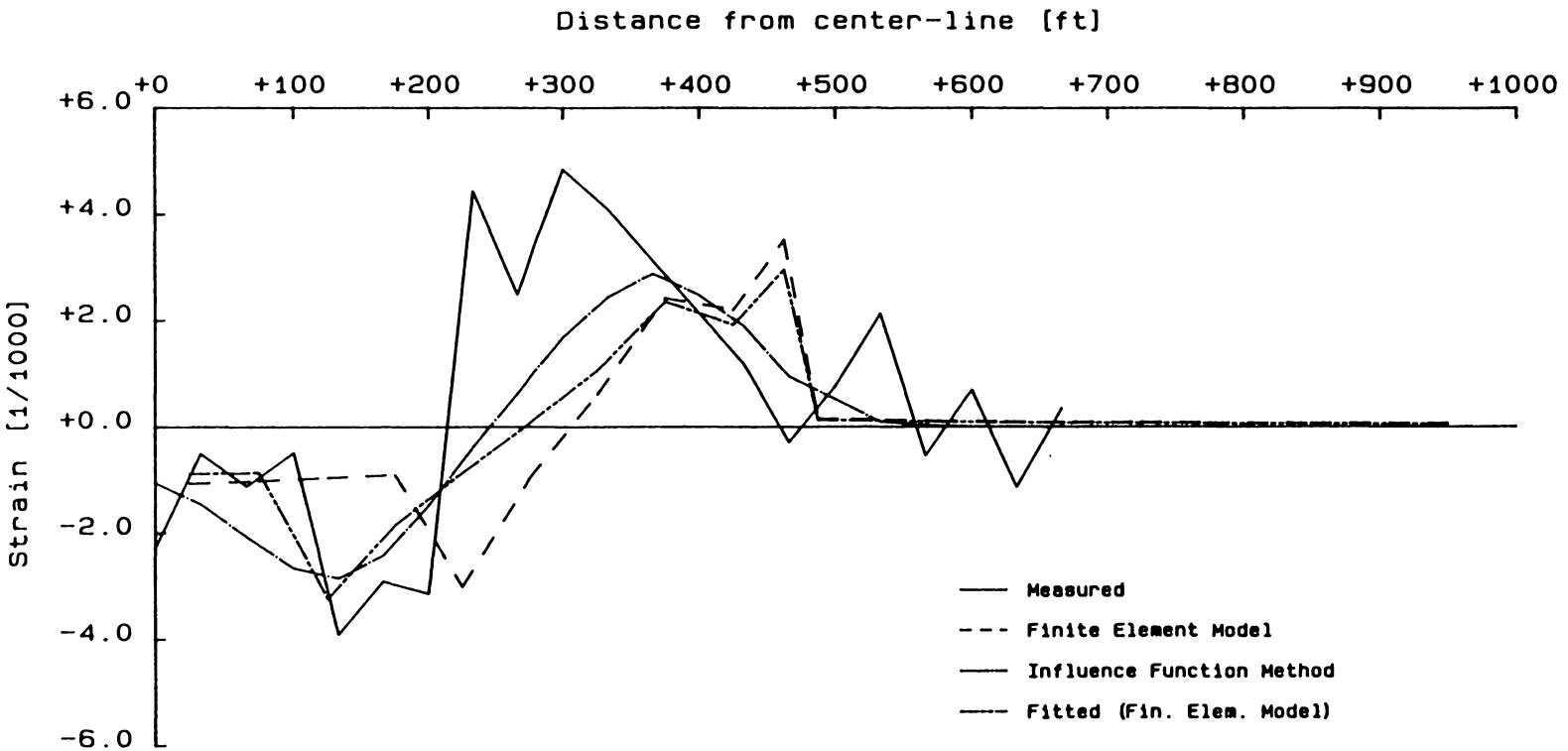

Figure 7.6 **Comparison of Measured and Calculated Strain Profiles for Case Study S4 Using: (a) the Finite Element Model; (b) the Influence Function Method; and (c) a Modified Finite Element Model (Fitted Curve)**

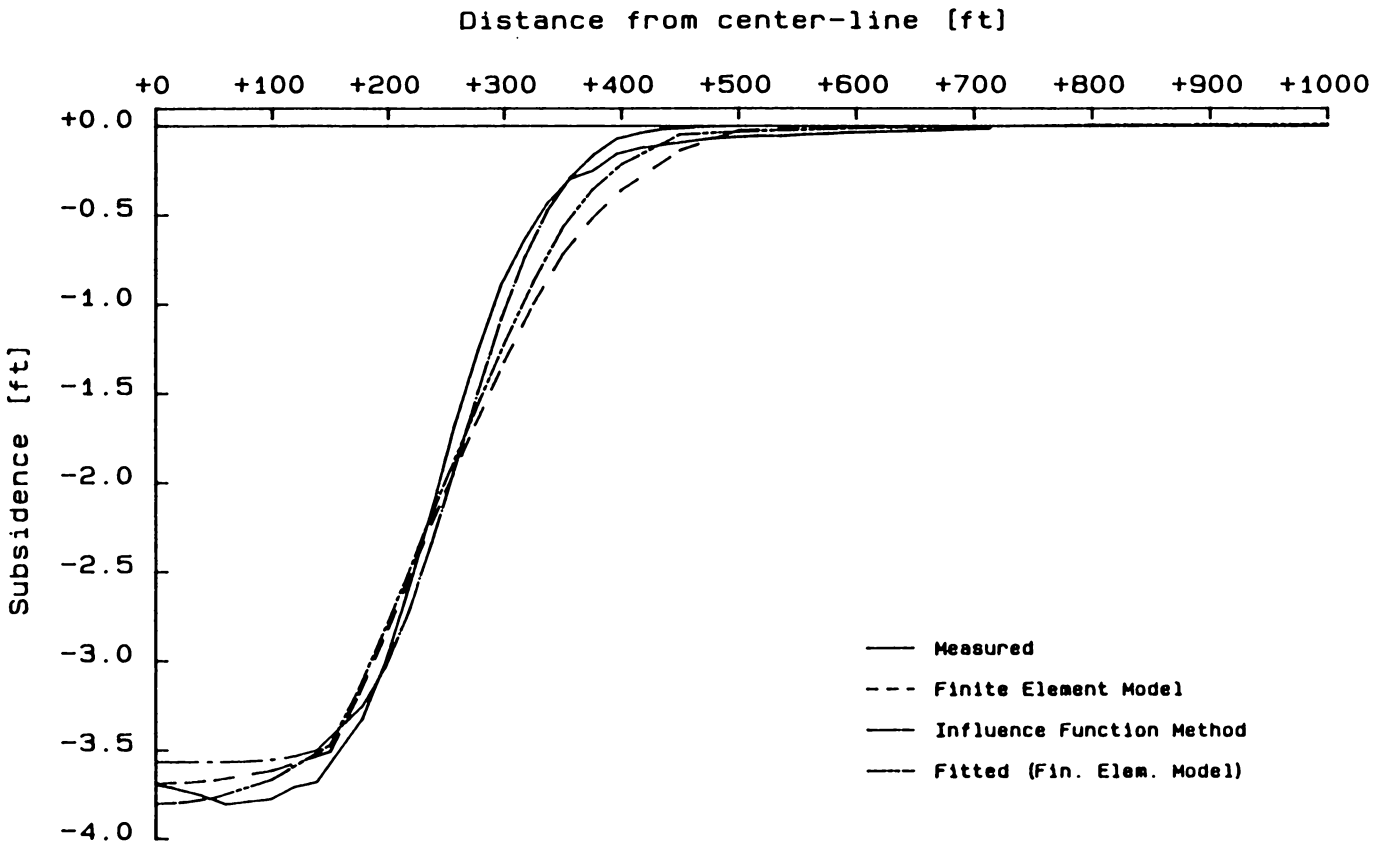

Figure 7.7 Comparison of Measured and Calculated Subsidence Profiles for Case Study S5 Using: (a) the Finite Element Model; (b) the Influence Function Method; and (c) a Modified Finite Element Model (Fitted Curve)

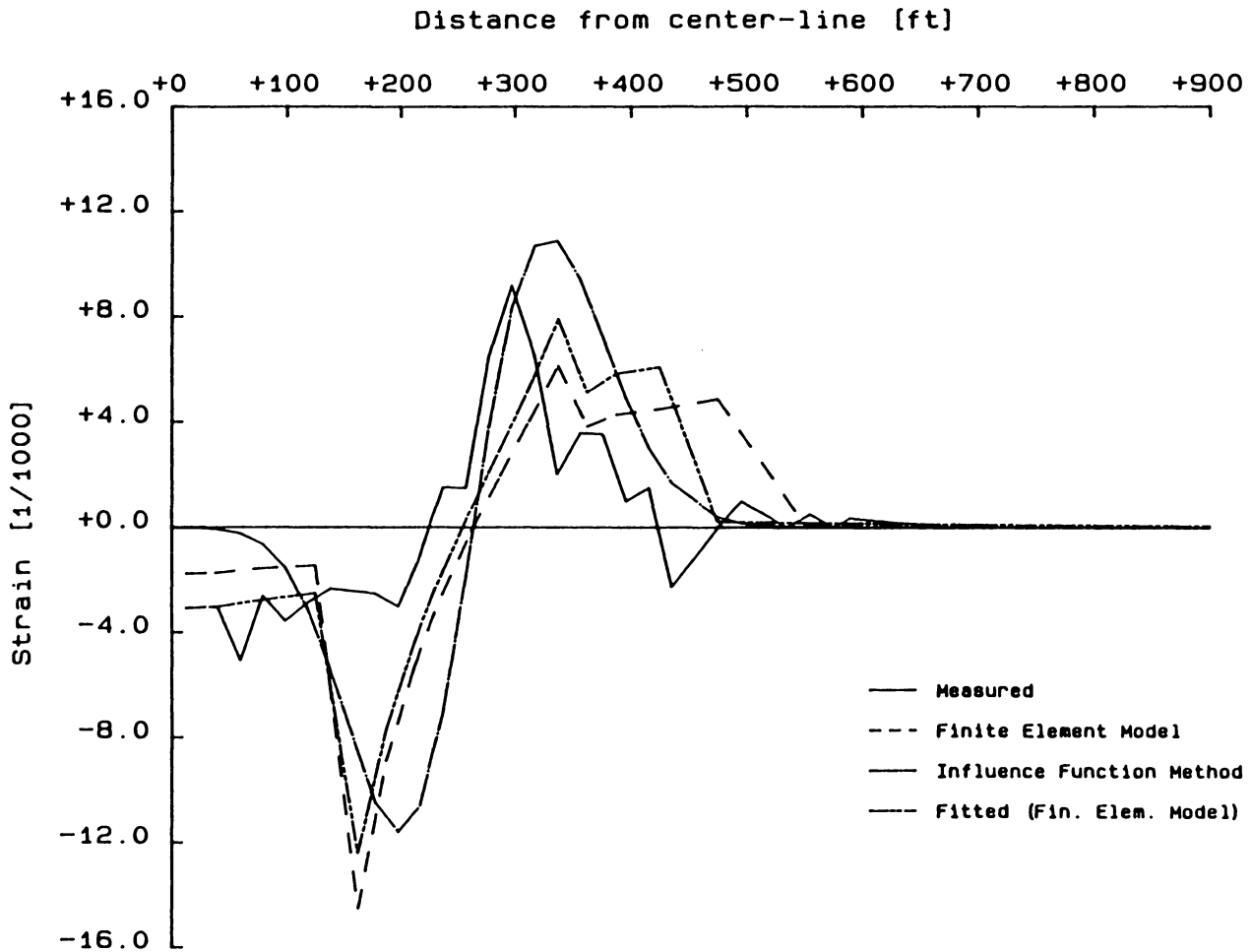

Figure 7.8 Comparison of Measured and Calculated Strain Profiles for Case Study S5 Using: (a) the Finite Element Model; (b) the Influence Function Method; and (c) a Modified Finite Element Model (Fitted Curve)

strain profiles obtained provide a good estimate of the maximum tensile and compressive strains ($\pm E_{max}$), and at the same time approximate the location of the maximum strains. Comparing the strain profiles obtained for Case Study S4 for the alternate mesh definitions, it can be observed (Figure 7.9) that their characteristics are directly related to the zone boundaries established in each mesh, as well as to the differences in magnitude of the elastic properties in the adjoining areas. By defining **transition zones** (i.e. zones with intermediate properties) between the proposed main zones, smoother strain profiles can be obtained. The profiles currently obtained, however, better describe those measured, when compared to the smooth profiles produced by the influence function method, which present a gradual change in horizontal strain. It should be noted that the introduction of more zones would complicate the proposed procedure, without significantly enhancing the calculated surface deformation characteristics.

Since the proposed procedure for predicting surface deformation characteristics is based on an empirical definition of certain parameters, model performance depends on the accuracy of such data. Therefore, the model is restricted to case studies with parameters within the data range, from which the aforementioned empirical relationships were derived. Model application, however, is not restricted if the necessary empirical data can be approximated for any given situation.

7.2 Application to Parametric Evaluation of Deformation Characteristics

One of the advantages of using a numerical formulation to model surface deformations is the ability to perform a parametric analysis by varying one or more of the case study attributes. The inherent assumption in all models analyzed up to this point was that the surface elevation remained constant over the area of excavation. Surface slopes of 30°

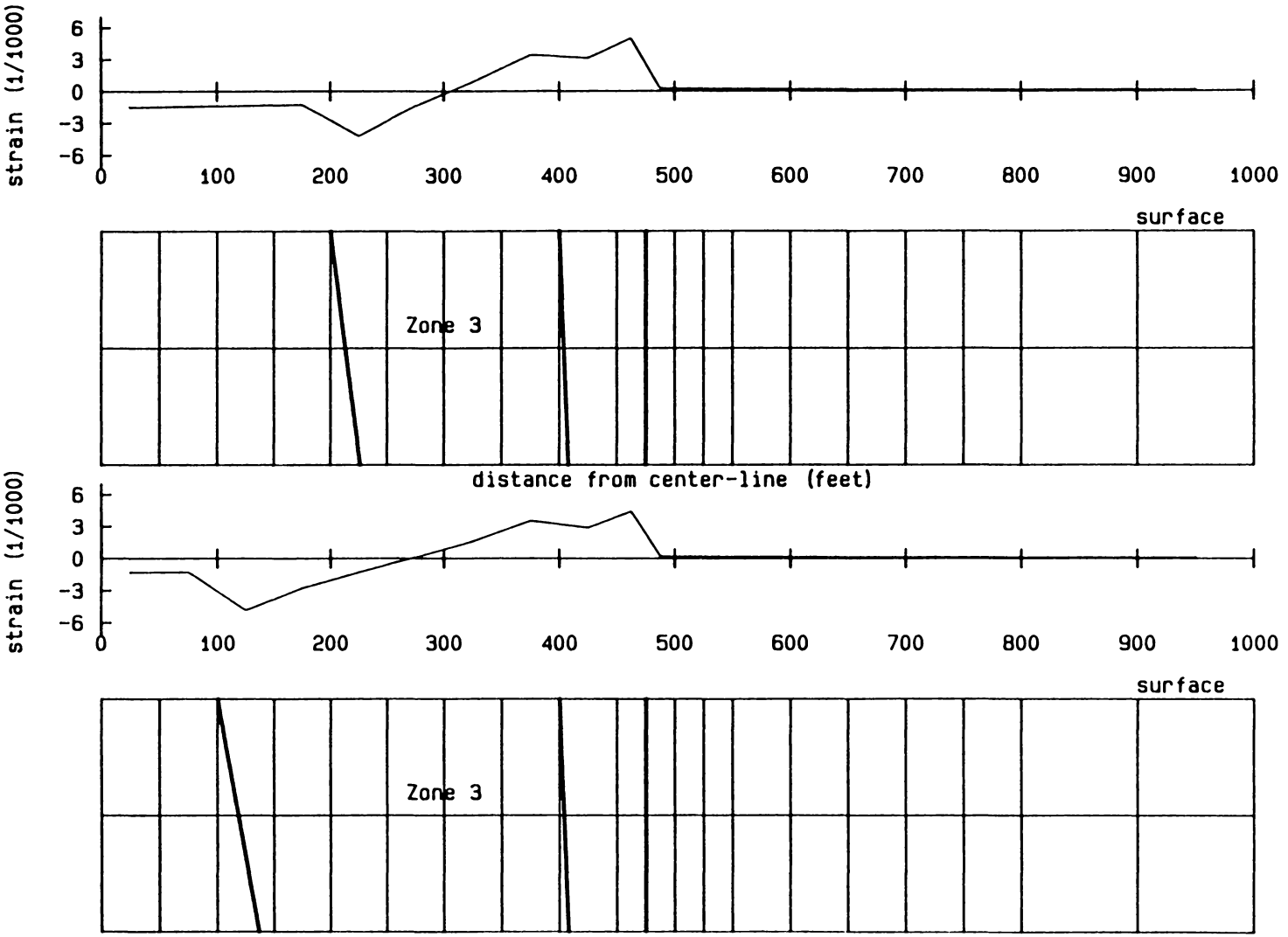

Figure 7.9 Comparison of Strain Profiles and their Corresponding Zone Definition (Case Study S-4)

however, are not unusual when mining occurs under mountainous terrain such as the Appalachian region.

The British National Coal Board (1975), has already identified the implications of a sloping surface to the prediction of surface strains as well as to the adjustment of measured strain profiles. A strain adjustment factor was proposed as a function of the initial slope angle (α_1) and the final slope angle (α_2):

$$\text{strain adjustment} = \pm \left[\frac{\sec \alpha_2}{\sec \alpha_1} - 1\right] \qquad [7.1]$$

The sign of the strain adjustment factor is positive for increasing gradients (slopes) and negative for decreasing gradients. In the former case the strain adjustment must be added to the tensile strain and substracted from the compressive strain.

A number of meshes was constructed representing panel cross-sections with varying surface slopes for a hypothetical case study. Panel half-width was 300 feet, average overburden depth was kept at 600 feet while the inflection point was located at -150 feet from the rib. Analysis was performed assuming a horizontal surface and surfaces sloping at 30°, 20° and 15°, with respect to the horizontal as shown in Figure 7.10. It should be noted that the surface slope profiles were constructed by keeping the surface projection of the inflection point constant. The sloping profiles were extended beyond the excavation rib until they intersected the draw line, whereupon they became horizontal. Figure 7.11 compares the subsidence profiles calculated for the three different slope angles and the one calculated for a horizontal surface. Figure 7.12 shows the corresponding strain profiles. The calculated inflection point for each of these profiles is the point where the horizontal strain becomes zero. Comparison of these profiles indicated that the calculated inflection point was translated along the slope direction pro-

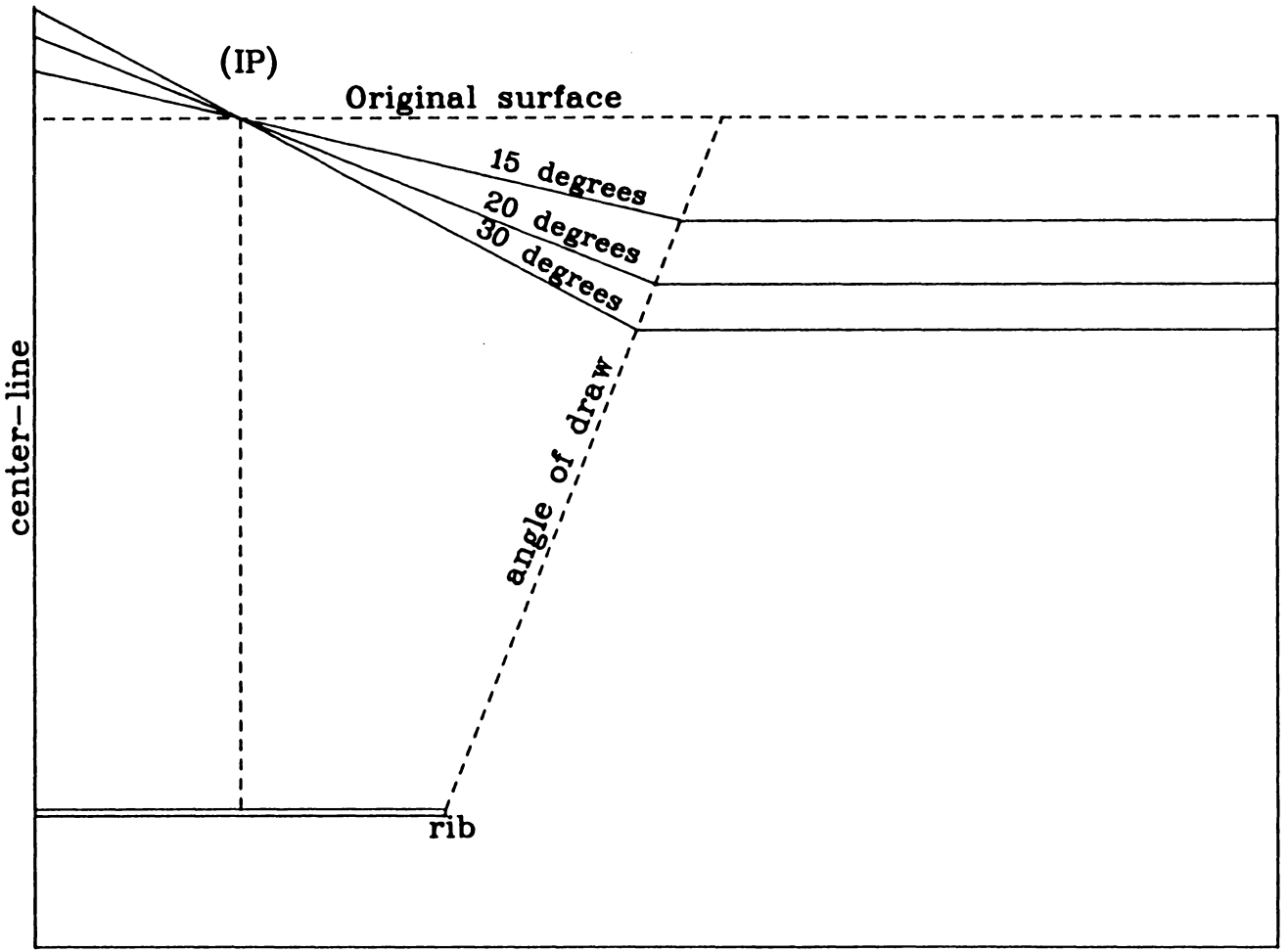

Figure 7.10 Mesh Definitions for Surface Slopes of 30°, 20° and 15°

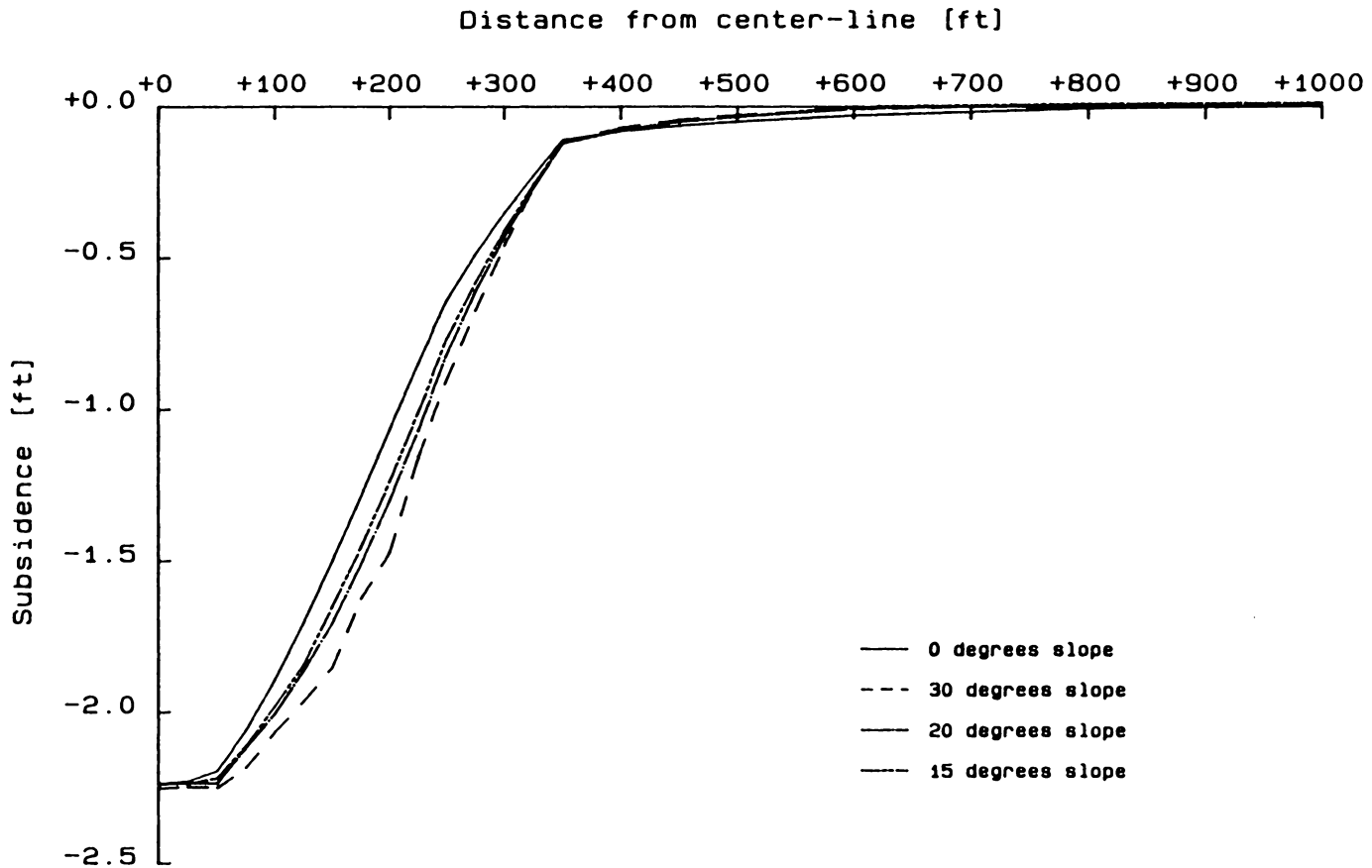

Figure 7.11 **Comparison of Subsidence Profiles for Different Surface Slopes**

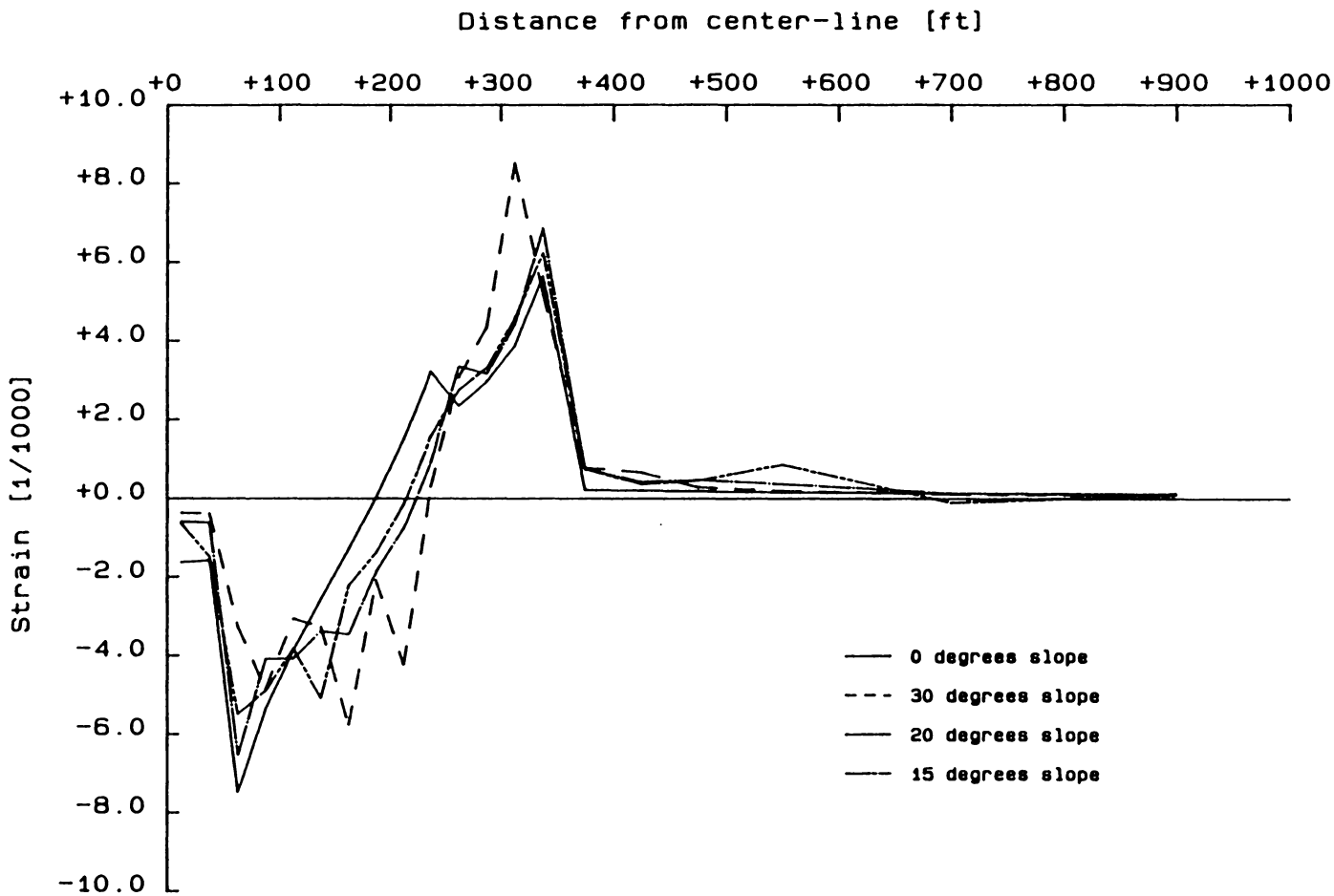

Figure 7.12 **Comparison of Strain Profiles for Different Surface Slopes**

portionally to the slope angle. At the same time, the maximum tensile strain of the sloping profiles increased, while the maximum compressive strain decreased, which is in accordance with the aforementioned adjustment of horizontal strains (NCB, 1975). Frank and Geddes (1986), also analyzed the effects of surface slope to the subsidence and horizontal strain profiles for different mining sequences. Their model, however, presented a parametric analysis of idealized case studies and has not been validated for specific case studies. Their results are similar to the ones presented, in the sense that higher sloping profiles exhibit a "sharper" subsidence curve as well as higher maximum tensile values.

Chapter 8

Conclusions and Recommendations

The analysis of immediate roof behavior using empirical and analytical methods, and the critical evaluation of overburden deformation patterns above longwall and room-and-pillar mines in the eastern U.S. coalfields, resulted in the development of a numerical model for calculating surface deformation characteristics over underground coal mines. This procedure was based on the well-known finite element method and incorporated concepts related to the mechanics of strata deformation characteristics, through empirical indices associated with subsidence engineering.

Different material behavior models, failure criteria, and failure-inducing mechanisms were employed in an attempt to determine the formulation which best approximates surface deformations. Deformation zones based on the aforementioned empirical parameters were defined in the overburden, which resulted in accurate subsidence and horizontal strain calculations.

The ability of the model to fit a known surface subsidence profile was tested on several case studies. Also, for the same case studies, calculated strain profiles approximated closely those measured. Subsequently the model was used to predict surface deforma-

tion profiles for case studies within the range of the empirical data bank. The successful implementation of the model complements the existing prediction methods, namely the profile function method, the zone area method and influence function method. Additionally, results obtained by the latter method were compared to those calculated by the numerical model, since both methods can be used for calculating vertical as well as horizontal movements.

The advantages of using this model compared to other models available in the literature are that:

- The formulation utilized empirical indices used in subsidence engineering, in order to incorporate the site-specific characteristics into the model.
- The model was sensitive to the ratios of the elastic moduli used to describe different rocks and/or rock conditions, and not to the magnitude of the elastic properties.
- The use of fixed displacement nodes around the opening to induce failure overcame the roof-floor overlap problem encountered in other formulations.
- The use of arbitrary reduction factors to convert laboratory to insitu property values was completely avoided.
- Scaling of the calculated surface displacements was based on the empirically predicted regional or local parameters.
- The model could satisfactorily predict horizontal strain profiles; lack of this capability was a disadvantage of previous formulations.
- Parametric analysis was also possible for different excavation geometries, roof convergence curves and overburden properties.

Since the results from the numerical calculations depend upon the empirical parameters used, which, in turn, were derived statistically from a regional data base, the procedure

might not yield accurate results for case study characterized with parameters outside this data range.

Furthermore, it is recommended that additional research in the following areas may establish a more comprehensive model for calculating surface deformations.

- Since the zone definition in the overburden was based on data for a specific region, which reflect the prevailing geologic conditions and geomechanical rock behavior, further studies may be needed to determine whether the model behaves in a similar fashion for other regions.
- The model could also be enhanced to accomodate a step-by-step excavation sequence in the preferred mining direction.
- The two-dimensional approach assumes uniform panel conditions, which are represented by the panel cross-section. Other factors (such as the presence of a remnant pillar) must be approximated by appropriately modifying the roof convergence curve. A three-dimensional approach would eliminate the latter approximation, therefore yielding more accurate results, at the expense, however, of higher analysis cost.

REFERENCES

1. Adler, L. and M. C. Sun (1968), "Ground Control in Bedded Formations", Virginia Polytechnic Institute and State University, ***Bulletin*** 28, December.

2. Agioutantis, Z. and Karmis M. (1986), "A Study of Roof Caving in the Eastern U.S. Coalfields", ***Proceedings***, 5th Conference on Ground Control in Mining, Morgantown, West Virginia, June, pp. 134-146.

3. Bathe, K. J. (1975), "A Finite Element Program for Automatic Dynamic Incremental Nonlinear Analysis - (ADINA)", Massachusetts Institute of Technology.

4. Barton, N., R. Lien and J. Lunde (1974), "Engineering Classification of Rock Masses for the Design of Tunnel Support", ***Rock Mechanics***, Vol. 6, No. 4, pp. 183-236.

5. Beckett, L. A. (1984), "Longwall Mining, A Finite Element Study of Strata Behavior and Expected Subsidence", ***USBM Progress Report*** 10054, Denver Research Center, Denver.

6. Bieniawski, Z. T. (1976), "Rock Mass Classifications in Rock Engineering", ***Proceedings***, Symposium on Exploration for Rock Engineering Johannesburg.

7. Bieniawski, Z. T. (1984), ***Rock Mechanics Design in Mining and Tunneling***, A. A. Balkema, Rotterdam, Netherlands.

8. Cundall, P. A. (1974), "A Computer Model for Rock Mass Behavior Using Interactive Graphics for the Input and Output of Geometrical Data", University of Minnesota, Minneapolis.

9. Denkhaus, H. G. (1964) "Critical Review of Strata Movement Theories and Their Application to Practical Problems", ***Journal of the South African Institute of Mining and Metallurgy***, March.

10. Drucker, D. C. and Prager W. (1952), "Soil Mechanics and Plastic Analysis or Limit Design", ***Quarterly of Applied Mathematics***, Vol. 10, pp. 157-175.

11. Duncan, J. M. and Chang C. Y. (1970), "Non-Linear Analysis of Stress and Strain in Soils", ***Journal***, Soil Mechanics and Foundations Division, ASCE, September, pp. 1629-1653.

12. Duncan, J. M., R. Seed, K. Wong and Y. Ozawa (1984), "FEADAM84: A Computer Program for Finite Element Analysis of Dams", ***User's Guide***, Dept. of Civil Engineering, VPI&SU, Blacksburg, Virginia.

13. Farahmand, D. and G. Y. Li (1986), "An Application of Boundary Element Method for Underground Excavations in Jointed Rock", ***Proceedings***, 27th U.S. Symposium on Rock Mechanics, Tuscaloosa, Alabama, pp. 299-303.

14. Franks, C. A. M. and J. D. Geddes (1986), "Subsidence on Steep Slopes Due to Longwall Mining," ***Inter. Journal of Mining and Geological Engineering***, Vol. 4, pp. 291-301.

15. Girrens, S. P., C. A. Anderson, J. G. Bennett and M. Kramer (1982), "Numerical Prediction of Subsidence with Coupled Geomechanical - Hydrological Modelling", ***Proceedings***, Workshop on Surface Subsidence Due to Underground Mining, Morgantown, West Virginia.

16. Goodman, R. E., Taylor R. L. and T. L. Brekke (1968), "A Model for the Mechanics of Jointed Rock", ***Journal***, Soil Mechanics and Foundations Division, ASCE, May.

17. Gren, K. and E. Popiolek (1983), "Mining Influence on the Surface and the Rock Strata", Krakow, Poland (in Polish).

18. Holt, G. E. and P. A. Mikula (1984), "Evaluation of Subsidence Prediction Methods for Coal Mining in Eastern Australia", Australian Coal Industry Research Laboratories Ltd (ACIRL), Published Report 84-15.

19. Hsiung, S. M. and S. S. Peng (1985), "Chain Pillar Design for U.S. Longwall Panels", ***Mining Science and Technology***, Vol 2, pp. 279-305.

20. Hsiung, S. M. and S. S. Peng (1986), "Control of Floor Heave with Proper Mine Design - Three Case Studies", ***Mining Science and Technology***, Vol 4, pp. 257-272.

21. Karmis, M., and Z. Agioutantis (1985), "An Investigation into the Mechanism of Roof Caving and its Prediction Using Numerical and Geomechanics Techniques", ***Proceedings***, 3rd Annual Workshop, Generic Mineral Technology Center on Mine Systems Design and Ground Control, University of Kentucky, Lexington, Kentucky, pp. 53-74.

22. Karmis, M. and A. Jarosz (1985), "Subsidence Control in the Appalachian Coalfields", ***Proceedings***, 3rd Annual Workshop, Generic Mineral Technology Center on Mine Systems Design and Ground Control, University of Kentucky, Lexington, Kentucky, pp. 91-120.

23. Kidybinski, A. (1982), "Classification of Rock for Longwall Caveability", ***Proceedings***, State of the Art of Ground Control in Longwall Mining and Mining Subsidence, Editor M. Karmis, AIME published.

24. Knothe, S. (1957), "Observations of Surface Movements Under Influence of Mining and their Theoretical Interpretation", ***Proceedings***, European Congress on Ground Movement, University of Leeds, England, April, pp. 210-215.

25. Kratzsch, H. (1983), ***Mining Subsidence Engineering***, Springer-Verlag, Berlin, West Germany.

26. Kripakov, N. P., L. A. Beckett and D. A. Donato (1986), "Loading on Underground Mine Structures Influenced by Multiple Seam Interaction", ***Proceedings***, International Symposium on the Application of Rock Characterization Techniques in Mine Design, AIME Annual Meeting, New Orleans, Louisiana, March 2-6, pp. 196-206.

27. Lorig, L. J. (1984), "A Hybrid Computational Model for Excavation and Support Design in Jointed Media", Ph.D. Dissertation, University of Minnesota.

28. Matthews, J. (1986), "Specifying and Acquiring Longwall Shield Supports", ***Proceedings***, 27th U.S. Symposium on Rock Mechanics, Tuscaloosa, Alabama, pp. 360-366.

29. Mayer, A. D., A. K. Isaac and P. Neve (1984), "Validation and Error Analysis of a Strata Modelling Technique", ***International Journal of Mining Engineering***, Vol. 2, pp. 305-321.

30. Majumder, S. (1986), "The Support Requirement at a Longwall Face - A Bending Moment Approach", ***Proceedings***, 27th U.S. Symposium on Rock Mechanics, Tuscaloosa, Alabama, pp. 325-332.

31. Mozumbar, B. K. (1974), "A Mathematical Model of Ground Movement Due to Underground Mining", Ph.D. Dissertation, The Pennsylvania State University.

32. N.C.B., (1966), "Subsidence Engineer's Handbook", London, England.

33. N.C.B., (1975), "Subsidence Engineer's Handbook", London, England.

34. Penn State (1974), "A Master Environmental Control and Mine System Design Simulator for Underground Coal Mining", Final Report, Volume V: Subsidence Subsystems, U.S.B.M. Grant No. G0111808.

35. Peng, S. S. (1978), ***Coal Mine Ground Control***, John Wiley, New York.

36. Peng, S. S. and H. S. Chiang (1984), ***Longwall Mining***, John Wiley, New York.

37. Peng, S. S. (1986), ***Coal Mine Ground Control***, John Wiley, New York, 2nd edition.

38. Puckett, G. A. and P. A. Mikula (1984), "Development of Geotechnical Mathematical Modelling Techniques for Coal Mine Design" Australian Coal Industry Research Laboratories Ltd (ACIRL), Published Report 84-5.

39. Salamon, M. D. G. (1966), "Reconsolidation of Caved Areas", ***Research Report*** No. 58/66, Collieries Research Laboratory, Transvaal and Orange Free State Chamber of Mines.

40. Schilizzi, P. P. G. (1987), "Monitoring and Prediction of Surface Movements Above Underground Mines in the Eastern U.S. Coalfields", Ph.D. Dissertation, VPI&SU.

41. Serata, S. and B. H. Gardner (1986), "Prediction and Design Control of Surface Subsidence by Global Simulation of Mine Behavior Using Finite Element Model", ***Proceedings***, 2nd Workshop on Surface Subsidence Due to Underground Mining, Morgantown, West Virginia, June.

42. Sheorey, P. R. (1984), "Use of Rock Classification to Estimate Roof Caving Span in Oblong Workings", ***International Journal of Mining Engineering***, Vol. 2, pp. 133-140.

43. Siriwardane, H. J. and J. Amanat (1984), "Prediction of Subsidence in Hilly Ground Terrain Using Finite Element Method", ***Proceedings***, Second International Conference on Stability in Underground Mining, Lexington, Kentucky.

44. Sutherland, H.J. (1986), "Program Review: Subsidence and Roof Stability Analysis for the Extraction and In Situ Processing of Fossil Fuels", ***In Situ***, 10(4), pp. 313-389.

45. Tang, D. H. Y. and S. S. Peng (1986), "Causes and Mechanisms of Surface Fractures in a Central West Virginia Coal Mine", ***Mining Science and Technology***, Vol. 4, pp. 41-48.

46. Trent, B. C. (1979), "A Computerized Subsidence Model", AIME Annual Meeting, New Orleans, Louisiana, February.

47. Unrug, K. and T. B. Szwilski (1982), "Methods of Roof Caveability Prediction", ***Proceedings***, State of the Art of Ground Control in Longwall Mining and Mining Subsidence, Editor M. Karmis, AIME published, pp. 13-29.

48. Valliappan, S. and R. S. Evans (1980), "Finite Element Analysis of a Slope at Illawarra Escarpment", ***Proceedings***, 3rd Australian - New Zealand Geomechanics Conference, Wellington, New Zealand.

49. VPI&SU (1981), "Design Optimization in Underground Coal Systems" Volume X: Underground Longwall Ground Control Simulator, Final Technical Report, Contract No. U.S.D.O.E. AC01-76ET10722, U.S.D.O.E., 235p.

50. VPI&SU (1987), "Prediction of Ground Movements Due to Underground Mining in the Eastern United States Coalfields", Final Report, Office of Surface Mining, Reclamation and Enforcement, Contract No. J5140137, Vol. I,II., March.

51. Zienkiewicz, O. C., S. Valliappan and I. P. King (1969), "Stress Analysis of Rock as a no Tension Material", ***Geotechnique*** 18, pp. 56-66.

Appendix A

Roof Stability Evaluation Program

A computer program was developed in BASIC (run under DOS on an IBM-PC or compatible computer) in order to facilitate calculations pertaining to roof stability evaluation, using both analytical methods (i.e. beam/plate theories) and roof classification methods. A schematic flowchart of the program is given in Figure A.1.

The data required for each case study included detailed information on the immediate roof layers and the panel geometry (i.e. length, width, width of entries, extraction height, face advance increment, etc.). Information for each roof layer included its thickness, and the magnitude of the corresponding geomechanical properties (i.e. compressive strength, tensile strength, elastic modulus, Poisson's ratio, etc.). Each layer was either considered as one structural entity, or could be subdivided into a number of **sub-layers** with equivalent properties. Additionally, a set of roof strength reduction coefficients was entered, to be used with the roof classification system. Figure A.2 shows typical information given for one of the case studies.

Once data entry was completed, the following options were available:

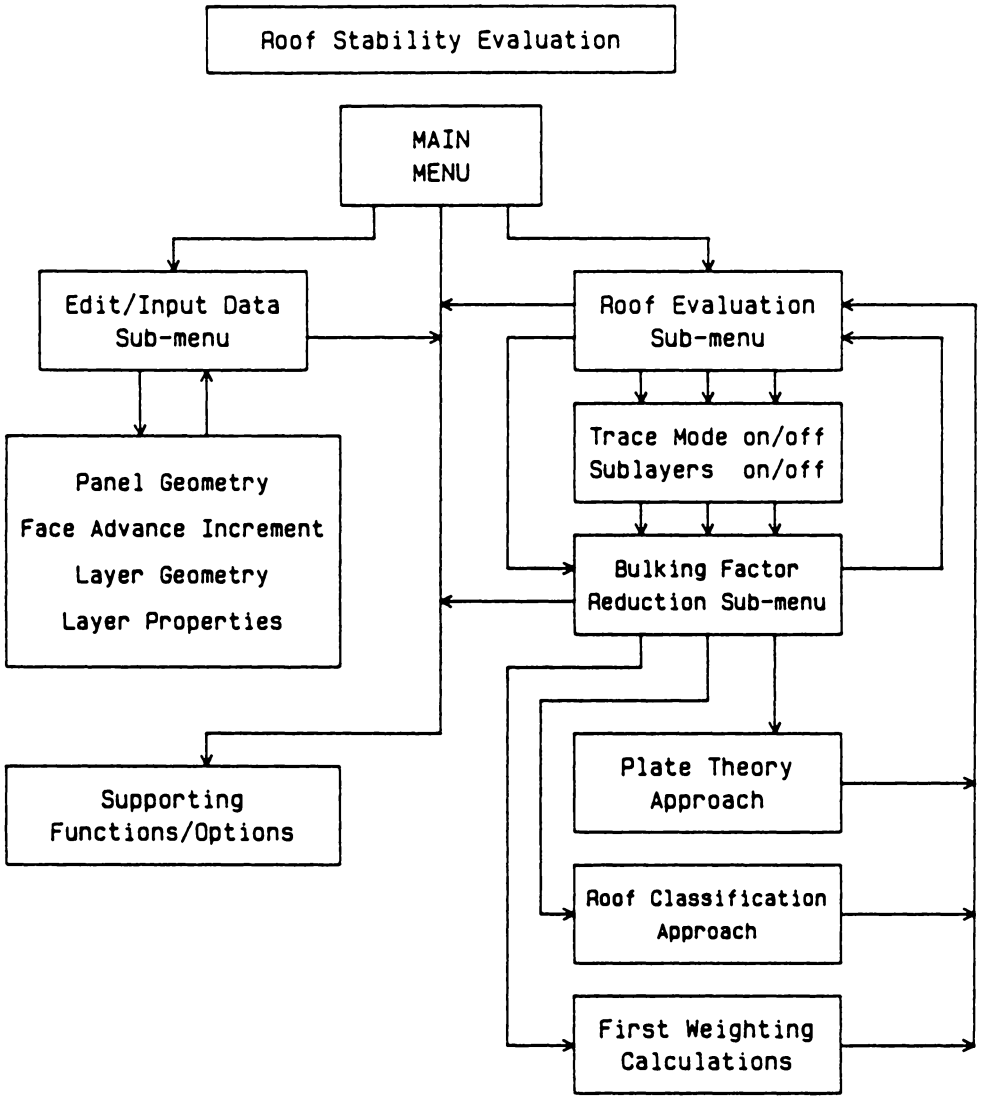

Figure A.1 Schematic Flowchart of the Roof Stability Evaluation Program

General Characteristics for: U1	
Total Overburden Layers (auto-update)	7
Coal Seam Thickness (in)	50
Coal Density (lb/cf)	95
Long-wall panel width (ft)	600
Total width of side entries (ft)	40
Total face advance (ft)	500
Face advance increment (ft)	2
Subsidence factor (0-1)	.5

	Layer 1		
	Rock type	s.shale	
	Density (lb/cf) (0= not active)	150	
	Thickness (ft)	3	
	Number of eq. spaced sub-layers	1	
	Bulking factor	1.25	
	Compressive strength (psi)	17900	
	Tensile strength (psi)	2000	
	Young's Modulus (psi)	1560000	
Classification	RQD (%)	60	
parameters:	RMR rating	-	
Default values for	(ss=.33, ms=.42, cs=.5) K1:	0.6	
reduction factors	(ss=.70, ms=.60, cs=.6) k2:	0.6	
[sandstone, mud-	(ss=.60, ms=.40, cs=.4) k3:	0.6	
stone, claystone.]	L (calculated):	398	very strong

Figure A.2 Typical Information Given in the Roof Stability Evaluation Program

- progressive roof layer failure could be calculated using the appropriate beam/plate equations. Failure was arrested when the volume of the failed (loose) material, which was calculated by applying a bulking factor, exceeded the volume of the opening. The bulking factor reduction was calculated for each failed layer (or sub-layer), and was subsequently subtracted from the initial bulking factor of the layer. The use of a variable bulking factor ensured that re-compaction of the failed material was estimated as a function of the distance from the seam. Each time the face was advanced, the dimensions of the opening, and thus the horizontal dimensions of the roof plate, changed, so the maximum normal stresses generated had to be re-calculated.

  Once a layer (or sub-layer) failed, the total volume was updated, and the **overhang** was calculated. Upon failure of a cantilever beam or plate, shearing failure does not usually occur at the point of support, thus leaving a much smaller cantilever in place of the original structure, which is termed overhang. This offers a partial support to the higher layers by effectively reducing the exposed area. Using the new dimensions of the opening, the next layer was examined for failure, and then the face was advanced, repeating the cycle. Figure A.3 shows a schematic flowchart of the progressive roof failure formulation.
- the first weighting (i.e. the face advance for which initial roof failure occurred) could be calculated using different analytical or empirical formulas.
- roof stability could be evaluated by calculating the Rock Quality Index (Section 2.4) for each layer, assuming each time that the layer was the first layer (e.g. not supported) in the roof sequence.

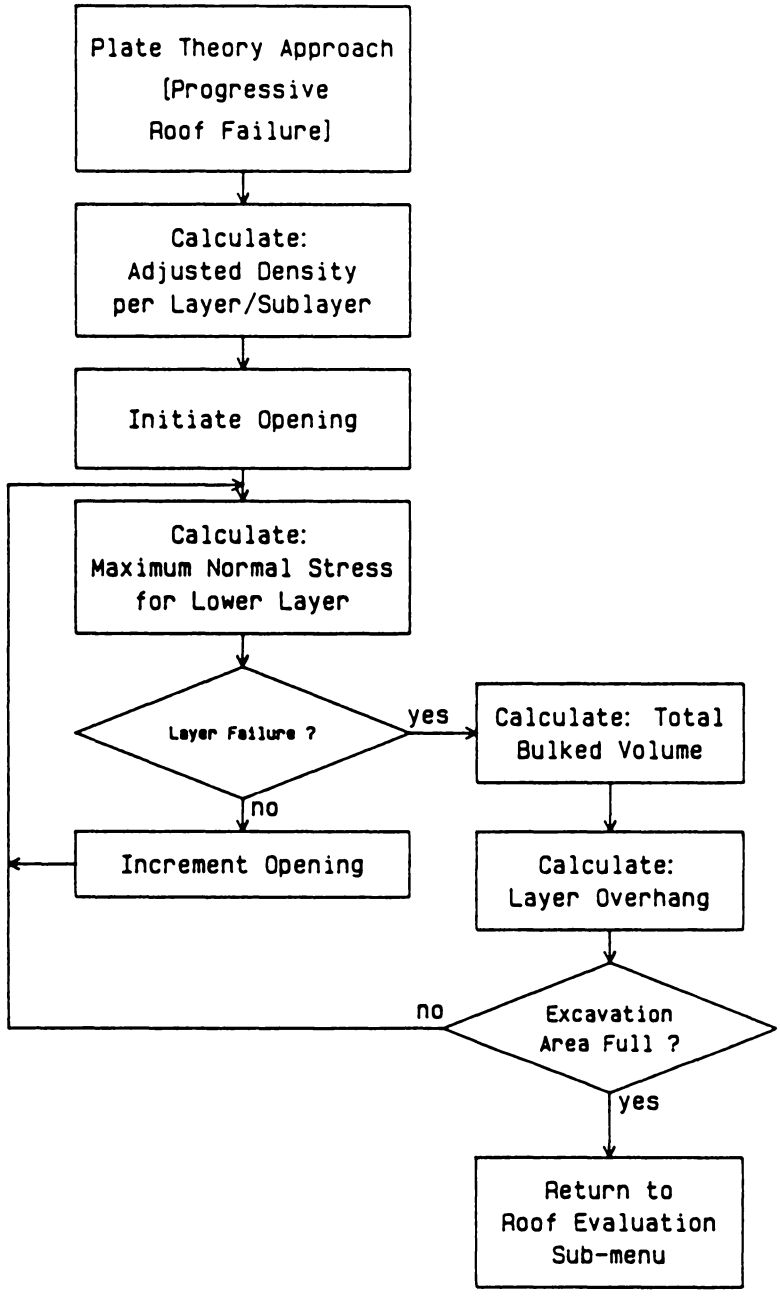

Figure A.3 Schematic Flowchart for Calculating Progressive Roof Failure, Using the Plate/Beam Theory Approach

For the first two options, calculations could also be performed under a **trace** mode, where all intermediate results were displayed on the screen. Additionally, each layer could be considered as one structural entity or as being composed of a number of sub-layers, if any were initially defined. In most cases results were similar for both cases.

Appendix B

Quadrilateral Element Mesh Generator

The finite element code developed in this study required the use of quadrilateral elements to describe the domain. Initially, the domain was subdivided into individual elements by sets of vertical and horizontal lines. The spacing between these lines varied, so that smaller elements could be defined in the areas where more accurate results were needed. A mesh generator was developed to facilitate definition of these elements based on mesh geometry, element spacing, location of opening, etc.

The iterative procedure started from the lower left corner, where the first node and the first element were defined. The horizontal extent of the mesh was then incremented according to the spacing of the vertical lines, until the maximum dimension was reached. The procedure was repeated for each horizontal layer, as described by the spacing of the horizontal lines, until the maximum vertical extent was reached. When joint elements were present in the formulation, the algorithm allowed the definition of additional nodes along the appropriate horizontal lines. In this first step, the coordinates of all nodal points were defined at the intersections of the horizontal and vertical lines.

In the second step, the nodal points describing each element were determined in a counter-clockwise direction (i.e. lower left, lower right, upper right, upper left). During this step, the opening location was identified, and appropriate action was taken (i.e. definition of chock elements, air-elements, or definition of none of these elements). Joint elements were also defined, using four nodes, where the upper and lower nodes had the same coordinates for a given element. Appropriate material-type codes were assigned to such elements, which represented the type of element and the property set to be used for that particular type. For example, joint elements were represented by material types 201-299, where material type 201 was interpreted as a joint element employing properties found in Set Number 1.

The initial stresses for each element were then calculated, based on the overburden column above a particular element. During the initial stages of the analysis, material properties corresponding to the intact rock elements were assigned "manually", by modifying the output file from the mesh generator program. When the definition of the vertical property zones became an integral part of the calculation procedure, the generator program was modified to automatically calculate the material type associated with each element. The lines defining the left and right boundaries of each zone (above seam level) were represented by two pairs of X-Y coordinates. The program then calculated, for each element, the distance of each node from a given boundary line. If all distances had the same algebraic sign, then the element was not intersected by the line, otherwise, the sum of the absolute distances on either side determined the material type assigned to the element. Figure B.1 represents an element intersected by a zone boundary line. Since $|a + d| > |b + c|$, or more area falls within the extent of Zone 2, the element is assumed to belong to Zone 2. The schematic flowchart of the mesh generator program given in Figure B.2 corresponds to the code developed for the HP-86B and

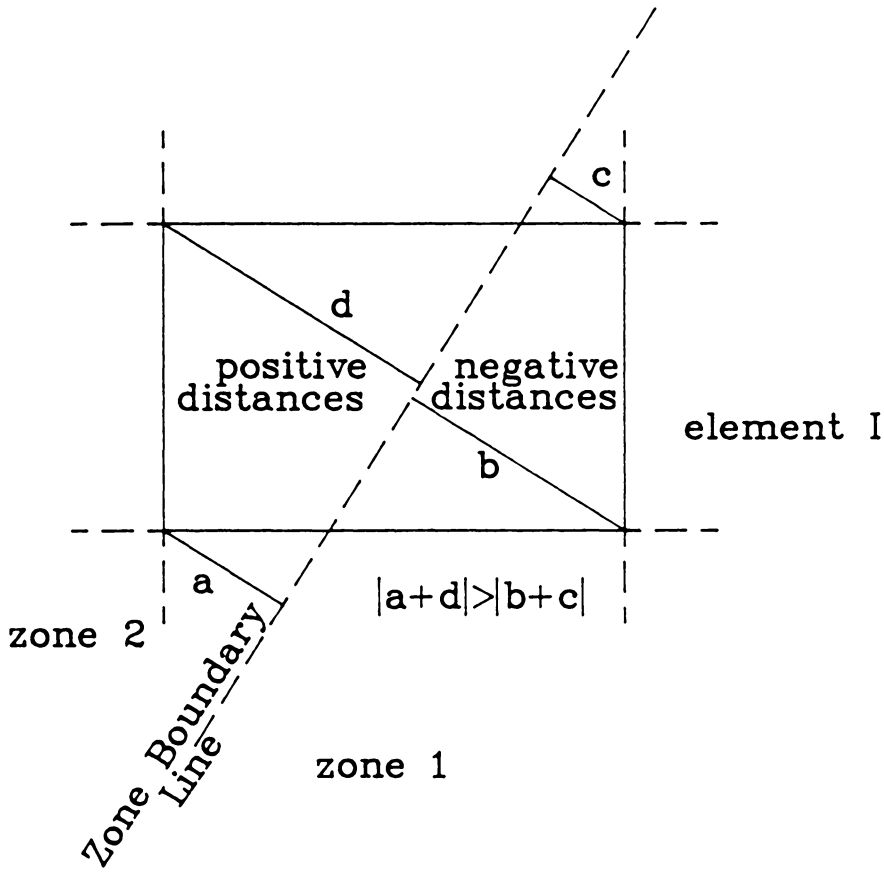

Figure B.1 **Intersection of Quadrilateral Element and Zone Definition Boundary Line**

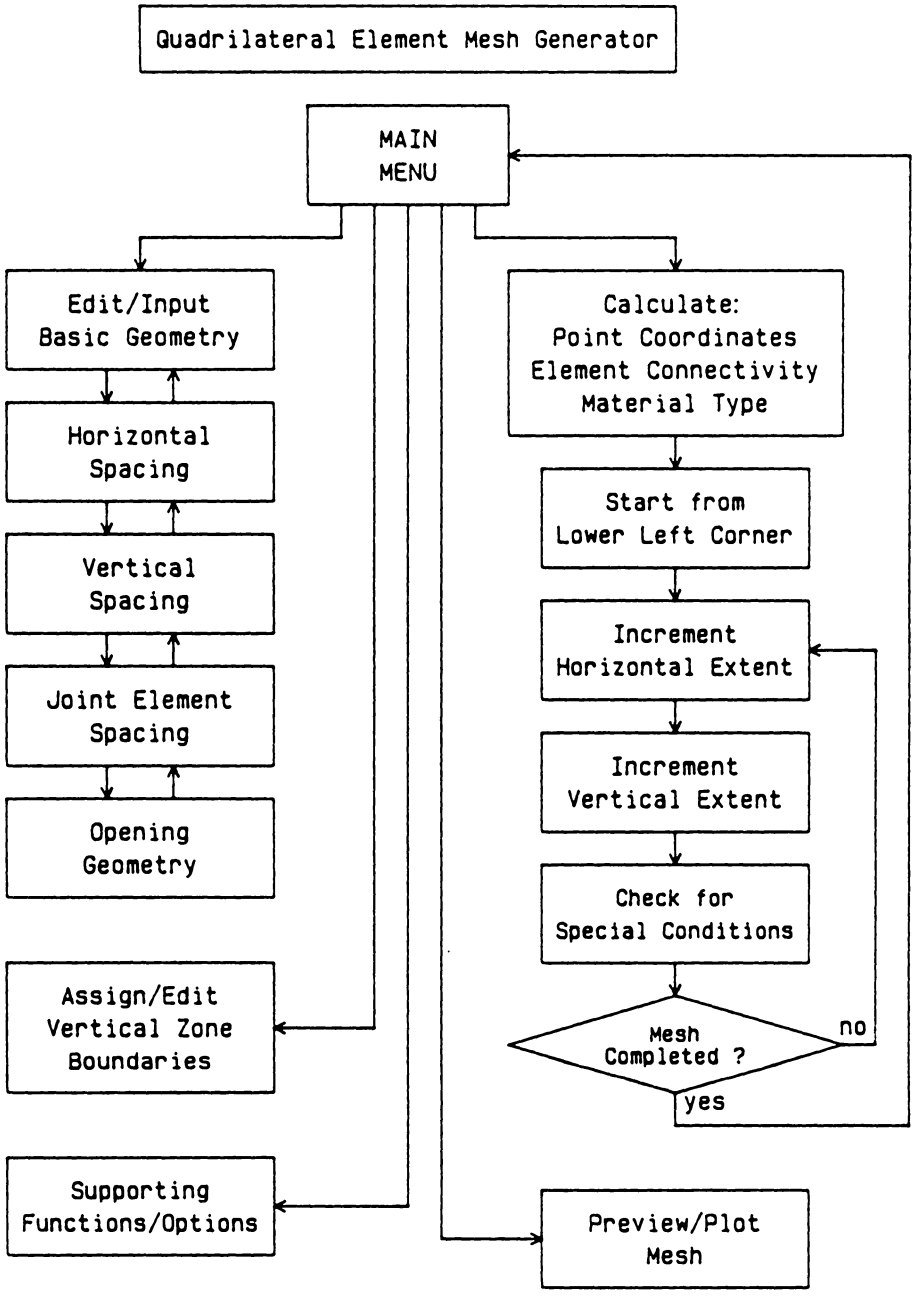

Figure B.2 **Schematic Flowchart of the Quadrilateral Element Mesh Generator Program**

IBM-PC systems, which were enhanced by graphics routines which allowed plotting of the generated mesh either on the screen or on a pen plotter. Finally, the program created, the file which was subsequently used for input to the finite element code (FEASD).

Appendix C

Finite Element Code for Analysis of Surface Deformations (FEASD)

The code was developed in FORTRAN-77 to run on an IBM mainframe system. The program structure and basic routines employed in the finite element program (i.e. derivation of strain displacement relationships for quadrilateral elements, evaluation of the element stiffness matrix, assembly of the global stiffness matrix, solution of the linear algebraic equations, etc.) were duplicated from the FEADAM84 code (Duncan *et al.*, 1984). The latter is a program which simulates soil behavior under conditions encountered in dam design. Figures C.1 and C.2 show a schematic flowchart of the FEASD program. During initial development of the code, multiple iteration schemes were employed, in order to determine the ability of different material models to successfully approximate the properties of failing material. The final model, however, employs a linear elastic, one-iteration scheme, although the capability for more iterations, and a collection of different material models, are built into the code.

The material property evaluation routine is the differentiating feature in every finite element model of overburden deformations. The model should be able to determine the

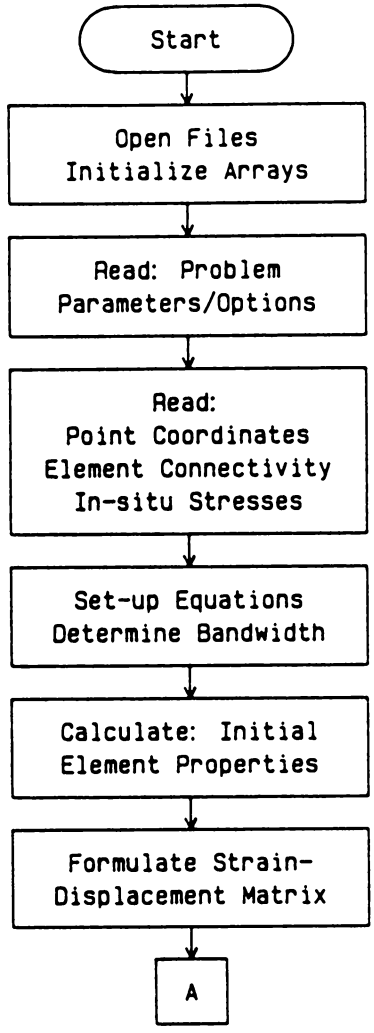

Figure C.1 Schematic Flowchart of the Finite Element Program for the Analysis of Surface Deformations [FEASD] (part 1)

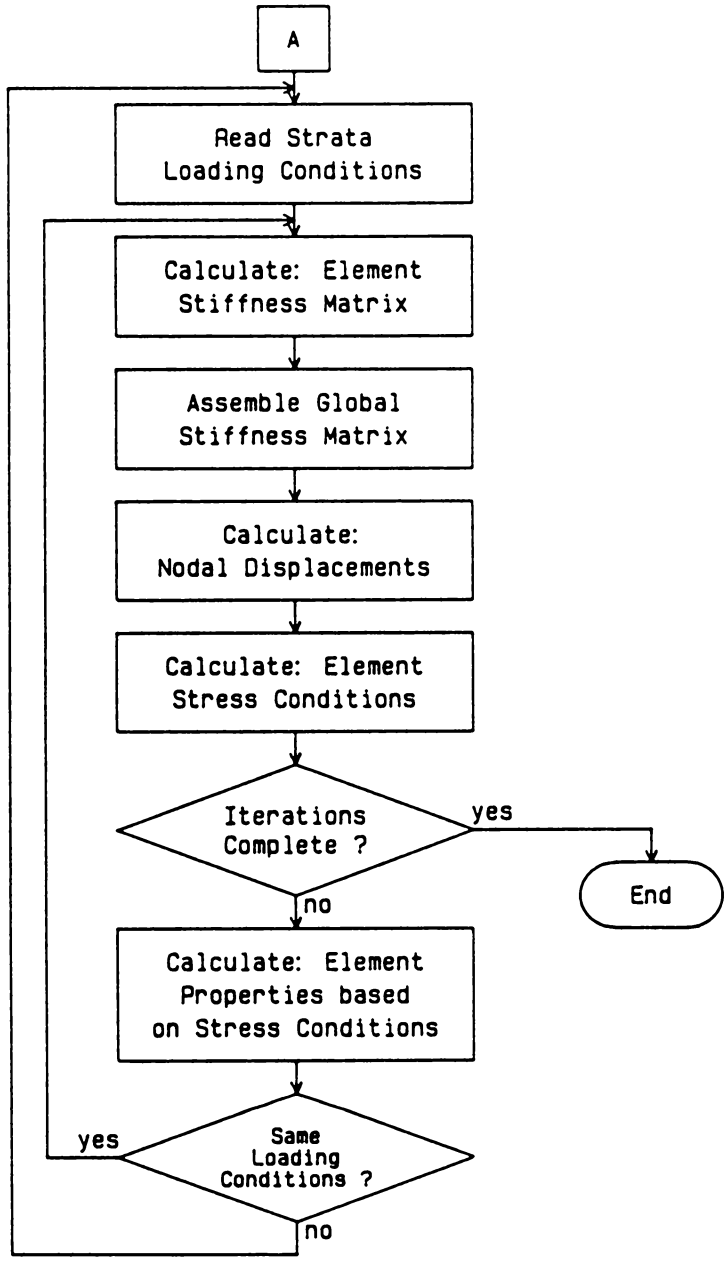

Figure C.2 Schematic Flowchart of the Finite Element Program for the Analysis of Surface Deformations [FEASD] (part 2)

properties of each element, based on the current stress-state, the previous stress-state and the **failure criterion** employed. The current stress-state reflects either the initial stress conditions, or is evaluated from the displacements calculated during the previous iteration.

To simplify data input, material properties corresponding to one element type (i.e. intact, joint, etc.), were grouped into sets. Upon program initialization, the material model and property set for each element type were selected. Figures C.3 and C.4 show a schematic flowchart of the subroutine used to evaluate the material properties for each element, based on the element type, material model and property set number.

After each iteration was completed, the stresses corresponding to each element were evaluated, and the corresponding material properties were selected for that element. Once an intact rock or a joint element failed, it could only assume properties corresponding to failure conditions. Joint elements were considered to be in failure when either the relative horizontal or vertical nodal displacements exceeded a preset value. Detection of failure for the intact rock element was more complicated depending on the criterion employed. Post-failure properties were either fixed or variable, depending upon the material model selected. In most cases, both the elastic modulus and Poisson's ratio were reduced with respect to the original values. The axial stiffness of the chock elements was increased, depending on the relative closure of the corresponding nodes in the opening. The advantages and disadvantages of using the different material models have been discussed, in Chapter 4.

Finally, the program printed the calculated nodal displacements and element stresses according to the requested format. The results were subsequently processed by other

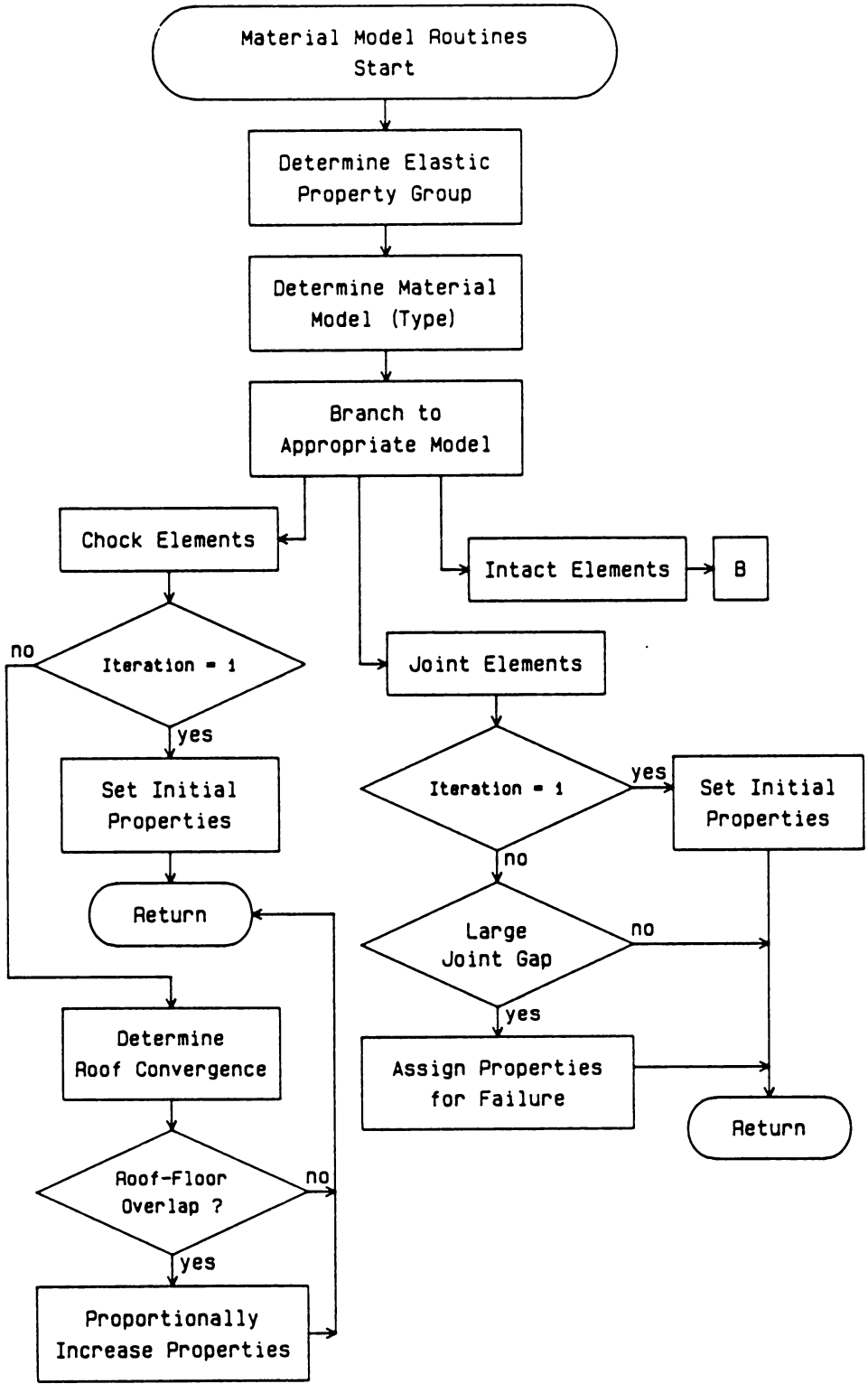

Figure C.3 Schematic Flowchart of the Material Model Subroutine in FEASD (part 1)

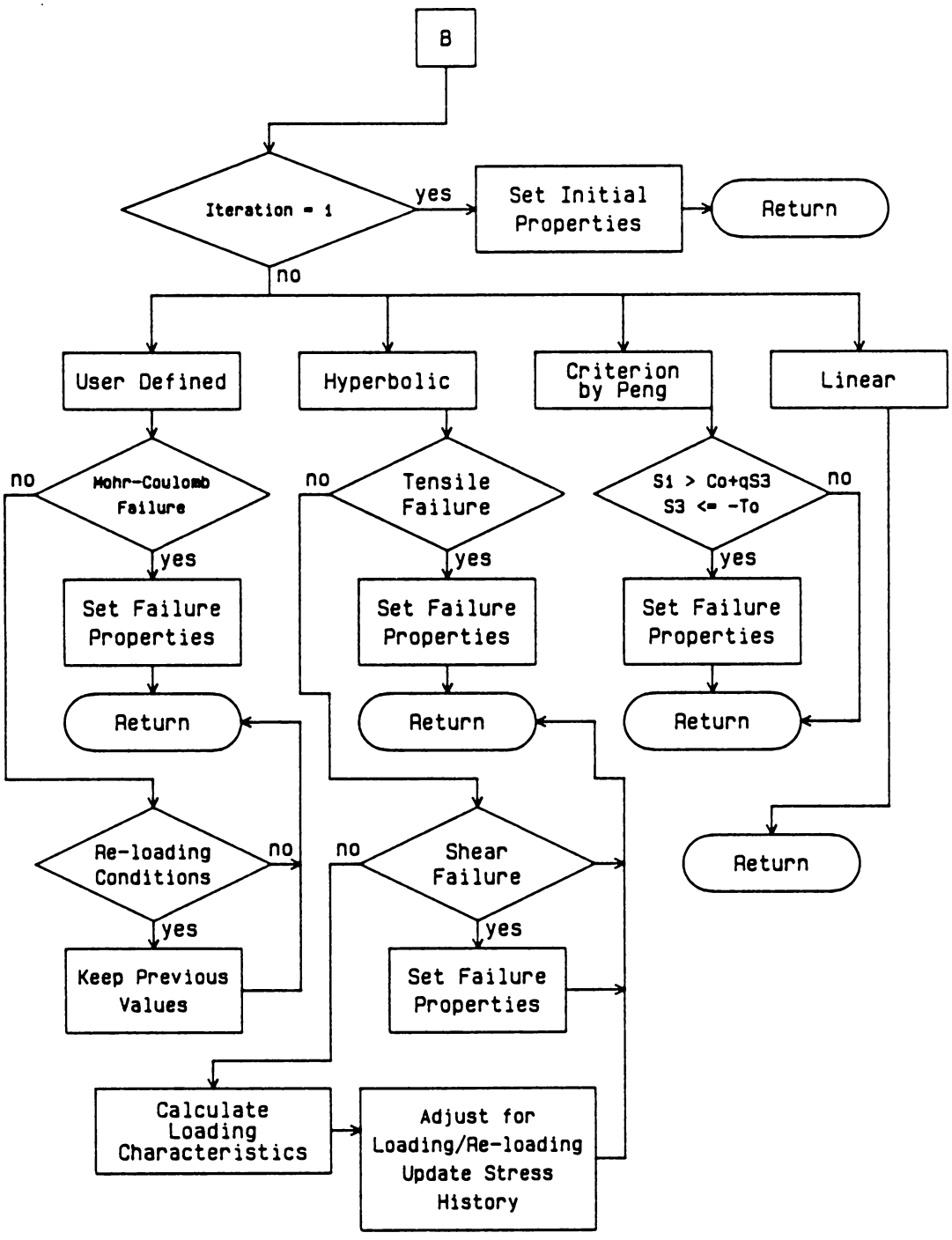

Figure C.4 Schematic Flowchart of the Material Model Subroutine in FEASD (part 2)

programs, either on the mainframe or on desktop computers, in order to create the corresponding plots and surface deformation profiles.

The vita has been removed from the scanned document